



CENTRO DE INVESTIGACIONES  
EN ÓPTICA, A.C.



# PHASE APERTURE METHODS FOR PHASE EXTRACTION AND SUPER- RESOLUTION MICROSCOPY



Thesis submitted for the award of the degree of Doctor of Philosophy

*Advisor: Abundio Dávila      Co-advisor: Cyril Mauchair*

*José Alberto Aguilar Mora*

*October 2015  
León, Guanajuato, México*



If you wish to make an apple pie from scratch, you must first invent the universe.

*Carl Sagan*



## ABSTRACT

---

In this work the effects of the modification on the optical microscope pupil, and their applications are presented. Two variations of the pupil are analyzed, in the first one the consequences of placing a vortex type phase filter in the pupil plane of the microscope is studied. The phase filter is a quantized version of an optical vortex; this modifies an optical microscope into a phase contrast microscope which can be used in the quantification of the measured phase by the rotation of the discrete vortex. This first modification in the pupil plane leads the extension of the phase vortex filter into two areas in optical metrology; speckle metrology and the creation of a new interferometer.

For the second study case, the pupil of the microscope was expanded creating a super resolution optical microscope. The developed microscope was based on the projection of structured light onto the sample, generating a synthetic pupil microscope twice the size as the original, which lets the passage of high frequency information that previously was restricted by the optical transfer function microscope. The built microscope was implemented for the measurement and characterization of nano-structures formed on metal surfaces with ultra-short laser pulses.

---



## RESUMEN

---

En este trabajo se presentan los efectos que tiene la alteración de la pupila en un microscopio óptico, así como sus aplicaciones y algunas variantes. Se analizan dos casos, en el primero se estudian las consecuencias de colocar un filtro de fase en el plano de la pupila del microscopio que consta de un filtro tipo vórtice. El filtro de vórtice se encuentra discretizado permitiendo modificar un microscopio óptico en un microscopio de contraste de fase que permite la cuantificación de la fase medida por medio de la rotación del vórtice discreto. Esta primera modificación en el plano de la pupila permite la extensión del estudio que tiene la inserción de un filtro de vórtice discreto en dos áreas de metrología óptica; la metrología de speckle y la creación de un nuevo interferómetro.

Para el segundo caso de estudio, se extendió la pupila del microscopio generando un microscopio óptico súper resolutor. El microscopio desarrollado está basado en la proyección de luz estructurada sobre la muestra, generando así una pupila sintética en el microscopio del doble del tamaño que la original, la cual permite el paso de información de alta frecuencia que antes estaba restringida por la función de transferencia del microscopio. El microscopio construido se implementó para la medición y caracterización de nano-estructuras formadas en superficies metálicas por un láser de pulsos ultra-cortos.

---





## DEDICATION

---

This work is dedicated to my family. Specially to my parents and brother who have been there all the time. Thank you for all your guidance.

---



## ACKNOWLEDGEMENTS

---

First of all, I would like to acknowledge the Consejo Nacional de Ciencia y Tecnología, CONACyT, for financial support through grants that did possible the PhD degree. Also, to the CIO, which was responsible of my education so this work could be presented. Additionally, I would like to acknowledge the Laboratoire Hubert Curien for being an important part on my career formation and to the LABEX pour l' Université de Saint-Etienne, for the financial support over the time I was there.

I wish to thank Dr. Abundio Dávila for giving me the opportunity of making part of this thesis work under his guidance. His scientific rigor and expertise in the field of optics have been a source of understanding and learning in the last years. Also Dr. Cyril Mauclair was a key player in the orientation that took this work. I owe him many thanks for his warm welcome and receptiveness, as well as for all the knowledge he shared. I also want to thank Dr. Jorge García Marquez , Dr. Enrique Landgrave, Dr. Arturo Gónzales and Dr. Eduardo López who have been over the last years looking at my progress.

I greatly appreciated the good cooperation with colleagues I had the chance to work with in both universities. Mc. Enrique Noe of the CIO who helped on software issues; also, to M. David Pietroy and M. Nicolas Faure, thank you for the academic support but specially for the deserts.

---



# CONTENTS

<b>0</b>	<b>Introduction</b>	<b>1</b>
0.1	Thesis scheme . . . . .	1
0.2	Contributions . . . . .	2
<b>1</b>	<b>Optical microscopy</b>	<b>3</b>
1.1	Introduction . . . . .	4
1.2	Microscope basics . . . . .	5
1.2.1	Microscope objective . . . . .	5
1.2.2	Illumination . . . . .	10
1.3	Microscope resolution . . . . .	12
1.4	Microscope techniques . . . . .	15
1.4.1	Phase contrast microscopy . . . . .	15
1.4.2	Confocal microscopy . . . . .	20
1.4.3	Microscopy based on nonlinear optics . . . . .	21
1.4.4	Super resolution microscopy . . . . .	23
1.4.5	Stimulated emission depletion microscopy . . . . .	24
1.4.6	Stochastic super-resolution microscopy . . . . .	26
1.4.7	Optical coherent tomography . . . . .	27
<b>2</b>	<b>Phase contrast quantitative microscopy based on optical vortex filtering</b>	<b>29</b>
2.1	Introduction . . . . .	31
2.2	Vortex phase filter . . . . .	32
2.2.1	Continuous vortex filter . . . . .	32
2.2.2	Multi-step vortex filter . . . . .	36
2.3	Vortex phase filter interference . . . . .	45
2.3.1	Weak phase objects . . . . .	46
2.3.2	Strong phase objects . . . . .	50
2.4	Phase extraction using vortex rotation . . . . .	56
2.5	Numerical simulation . . . . .	57
2.5.1	Spiral fringe patterns . . . . .	58
2.5.2	Phase contrast patterns . . . . .	59

2.5.3	Effect of incrementing the number of steps in the extracted phase . . . . .	60
2.6	Experimental results . . . . .	61
2.7	Point diffraction interferometer with spiral carrier . . . . .	64
2.7.1	Phase extraction . . . . .	68
2.8	Conclusions . . . . .	69
<b>3</b>	<b>Scattered light filtering using optical vortices</b>	<b>71</b>
3.1	Introduction . . . . .	72
3.1.1	Speckle pattern properties . . . . .	73
3.1.2	Out-of-plane measurement . . . . .	76
3.1.3	In-plane measurement . . . . .	79
3.1.4	Speckle shearing interferometer . . . . .	81
3.2	Displacement measurement with multi-level spiral phase plate in out-of-plane speckle interferometry . . . . .	82
3.2.1	Introduction . . . . .	83
3.2.2	Phase extraction . . . . .	85
3.2.3	Numerical simulation . . . . .	90
3.2.4	Experimental results . . . . .	94
3.3	Conclusions . . . . .	97
<b>4</b>	<b>Structured illumination microscopy</b>	<b>99</b>
4.1	Introduction . . . . .	100
4.2	Image formation . . . . .	102
4.3	Reconstruction algorithm . . . . .	107
4.3.1	Isolation of high frequency information . . . . .	109
4.3.2	Carrier removal . . . . .	112
4.3.3	Optical transfer function compensation . . . . .	116
4.3.4	Algorithm summary . . . . .	118
4.4	Experimental setup . . . . .	120
4.4.1	Performance of the microscope . . . . .	122
4.5	Application . . . . .	126
4.5.1	Inspection of nanostructures generated by ultrafast laser pulses . . . . .	127
4.5.2	Real time inspection of nanostructures generated by ultrafast laser pulses . . . . .	130
4.6	Conclusions . . . . .	138
<b>5</b>	<b>Discussions and conclusions</b>	<b>139</b>
5.1	Concluding remarks . . . . .	139

5.2 Further work . . . . . 141

**Bibliography** . . . . . **143**





# LIST OF FIGURES

1.1	Compound microscope setup . . . . .	4
1.2	Types of objective. a)Finite tube length microscope objective, b)infinity corrected microscope objective. . . . .	6
1.3	Typical microscope objective nomenclature. . . . .	7
1.4	Numerical aperture of a microscope objective. . . . .	8
1.5	Khöler Illumination. Top diagram shows the illumination path in yellow, while the sample path shown in green can be seen on the bottom diagram. . . . .	11
1.6	Epi Illumination. . . . .	12
1.7	Diffraction effect in an arbitrary pupil. . . . .	13
1.8	Fraunhofer diffraction for a circular aperture. a) Circular aperture, b) diffraction pattern of the circular aperture, c)diffraction pattern of two circular apertures separated over Rayleigh cri- teria, d) diffraction pattern of two circular apertures just in the Rayleigh criteria. . . . .	14
1.9	Effect of the light through no transparent and transparent samples. . . . .	16
1.10	Propagation of a plane wavefront through a transparent sample.	17
1.11	Phase contrast microscope with coherent illumination. . . . .	18
1.12	Phase contrast microscope with annular illumination. . . . .	18
1.13	Phase spiral contrast microscopy. . . . .	20
1.14	Typical confocal microscopy configuration. . . . .	20
1.15	Representation of different nonlinear optics process. a)SHG, b)THG, c)TPA. . . . .	22
1.16	Point spread function of circular aperture and a super reso- lution filter. . . . .	23
1.17	Energy levels of a typical Fluorophore. . . . .	25
1.18	Optical setup for STED microscopy. . . . .	25
1.19	Comparison of resolution and imaging depth for ultrasound, OCT and confocal microscopy. . . . .	27
2.1	4- <i>f</i> correlator. . . . .	31

2.2	Phase vortex. a) Mesh plot of a phase vortex, b) 2D image of a phase vortex with phase coded only in gray levels, c) 2D image of a phase vortex with carrier phase coded only in gray levels. . . . .	33
2.3	Point spread function of the optical vortex $ h(x_i, y_i) ^2$ . a) Surface of the PSF, b) upper view gray representation of the PSF. . .	33
2.4	Vortex phase filter with different topological charges $m$ . . . .	35
2.5	Vortex phase rotation. . . . .	35
2.6	Gray level representation of the vortex phase filter with spatial carrier, where the maximum phase (white) corresponds to $2\pi$ and zero phase is represented on black. . . . .	36
2.7	Vortex phase filter with spatial carrier PSF. . . . .	37
2.8	Phase of the MSSPF with variation of the $n$ and $p$ parameters. . .	39
2.9	Point spread functions of the multi-step spiral phase filter. a) $ h_2(x_i, y_i) ^2$ , b) $ h_3(x_i, y_i) ^2$ , c) $ h_4(x_i, y_i) ^2$ , d) $ h_5(x_i, y_i) ^2$ , e) $ h(x_i, y_i) ^2$ . . . . .	40
2.10	4-Step vortex filter. . . . .	41
2.11	Spatial light modulator typical shape. . . . .	43
2.12	4-Step vortex phase filter PSF $ h_4^{(1)}(x_i, y_i) ^2$ . . . . .	44
2.13	Vortex phase filter interference typical setup. . . . .	45
2.14	Intensity distribution $I^{(n)}(x_i, y_i)$ for a weak phase object. a) $I^{(1)}(x_i, y_i)$ , $\alpha_1 = 0$ , b) $I^{(2)}(x_i, y_i)$ , $\alpha_2 = \pi/2$ , c) $I^{(3)}(x_i, y_i)$ , $\alpha_3 = \pi$ , d) $I^{(4)}(x_i, y_i)$ , $\alpha_4 = 3\pi/2$ . . . . .	48
2.15	Extracted phase and amplitude from the interference patterns displayed on Fig.2.14. a) Amplitude $\mathcal{A}(x_i, y_i)$ , b) phase $\Theta(x_i, y_i)$ . . . . .	49
2.16	Deconvoluted phase and amplitude extraction from the interference patterns displayed on Fig.2.16. a) Amplitude $a_o(x_e, y_e)$ , b) phase $\varphi_o(x_e, y_e)$ . . . . .	50
2.17	Intensity distribution $I(x_i, y_i)$ with spiral carrier, for a continuous vortex phase filter. . . . .	51
2.18	Intensity distribution $I_4(x_i, y_i)$ with spiral carriers, caused by multi-step spiral phase filter. . . . .	53
2.19	Local fringe orientation definition $\beta(x_i, y_i)$ . . . . .	54
2.20	Local fringe orientation extracted map $\beta(x_i, y_i)$ from the interference pattern $I(x_i, y_i)$ from Fig. 2.17. . . . .	55
2.21	Extracted phase of the spiral interference pattern using one interferogram. a) Extracted convolved phase $\Theta_w(x_e, y_e)$ from Fig.2.17, b) extracted convolved phase $\Theta_4(x_e, y_e)$ from Fig.2.18	55

2.22	a) Deconvoluted phase $\varphi(x_e, y_e)$ using phase map from Fig. 2.21a, b) deconvoluted phase $\varphi(x_e, y_e)$ using phase map of 2.21b. . . . .	56
2.23	Computed interference pattern for $p = 4$ . a) $I_4^{(1)}(x_i, y_i)$ , b) $I_4^{(2)}(x_i, y_i)$ , c) $I_4^{(3)}(x_i, y_i)$ , d) $I_4^{(4)}(x_i, y_i)$ of a double element phase object. . . . .	58
2.24	Extracted wrapped phase using the interferograms of Fig. 2.23. a) Convolved phase $\Theta_4(x_i, y_i)$ , b) deconvoluted phase $\varphi_o^e(x_o, y_o)$ . . . . .	59
2.25	Computed interference pattern for $p = 4$ , a) $I_4^{(1)}(x_i, y_i)$ , b) $I_4^{(2)}(x_i, y_i)$ , c) $I_4^{(3)}(x_i, y_i)$ , d) $I_4^{(4)}(x_i, y_i)$ of an only phase USAF optical test pattern. . . . .	59
2.26	Extracted phase using the interferograms of Fig. 2.25. . . . .	60
2.27	a) Unwrapped extracted phase, b) absolute error map, between the unwrapped extracted phase and the simulated phase	61
2.28	Schematic diagram of the experimental setup. A detailed description of the elements and their function is given in the text. . . . .	62
2.29	Experimental interference pattern $I_p^{(n)}(x_i, y_i)$ with the MSSPF gray representation in the right corner. a) $I_3^{(1)}(x_i, y_i)$ , b) $I_4^{(1)}(x_i, y_i)$ , c) $I_5^{(1)}(x_i, y_i)$ . . . . .	63
2.30	Experimental extracted wrapped phase. a) Convolved phase $\Theta_4(x_i, y_i)$ , b) deconvoluted phase $\varphi_o^e(x_o, y_o)$ . . . . .	63
2.31	Schematic diagram of a point diffraction interferometer. The entrance pupil emits light transmitted or reflected by an object. Lens $L_1$ collects the light shown in green color that is focused on a pinhole and its neighborhood. The transmitted and diffracted light, shown in green and red, after the Smartt filter are collected by lens $L_2$ to form an interference pattern on plane $(x_i, y_i)$ where a camera detector is usually positioned.	65
2.32	Combined filter: Smartt and discrete phase vortex of four steps are placed in a stack. Each gray level in the phase vortex represent a constant phase of $0, \pi/2, \pi$ and $3\pi/2$ . . .	66
2.33	Optical setup of a point diffraction interferometer with the proposed combined filter. . . . .	67
3.1	Speckle formation over a detector $P$ . a) Objective Speckle formation on a rough surface, b) random phasor on $P$ . . . . .	72

3.2	Speckle pattern. a) Probability function, b) pattern recorded by a CCD camera. . . . .	73
3.3	Influence of the integration of speckles on the probability density function of the intensity. . . . .	74
3.4	Average speckle dimension for an illuminated area shown in red. a) Objective speckle size, b) subjective speckle size. . . .	75
3.5	Example of out-of-plane correlation fringes. a) Object with no deformation, b) object with deformation, c) intensity pattern on the CCD with no deformation, d) intensity pattern on the CCD with deformation, e) correlation fringe pattern. . . . .	77
3.6	Example of out-of-plane interferometer. . . . .	78
3.7	Example of in-plane ESPI. . . . .	79
3.8	Displacement by a load measured by an in-plane optical setup. a) Induced force over a bar causing a displacement $v$ , b) experimental in-plane displacement fringes over the observed area. . . . .	80
3.9	Schematic diagram of an optical setup of a speckle shearing interferometer. . . . .	81
3.10	Example of an object seen in the camera detector on a shearing interferometer configuration. a) Reference object, b) object displaced by the mirror a distance $\Delta x$ , c) superposition of the reference object and the shifted version of the object recorded by the camera detector. . . . .	82
3.11	Schematic diagram of a $4f$ optical correlator with a phase vortex filter represented in gray levels. . . . .	84
3.12	Influence of the four-step vortex on the speckle. . . . .	85
3.13	Phase map extracted with an algorithm based on Eq. (3.35). . . . .	90
3.14	Correlation fringe patterns obtained with the numerical simulation: (a) $I^{(1)}(x_i, y_i)$ ; (b) $I^{(2)}(x_i, y_i)$ ; (c) $I^{(3)}(x_i, y_i)$ ; (d) $I^{(4)}(x_i, y_i)$ . . . . .	91
3.15	Extracted phase obtained from the correlation fringe patterns of Fig. 3.14 and an algorithm based on Eq. (3.37). . . . .	91
3.16	Interferograms of the LCoS obtained with a Fizeau interferometer (a), and generated after a least squares fit of a low order polynomial to the OPD values provided by the interferometer (b). The bright areas show the actual size that was given to the phase vortex filter with a diaphragm. . . . .	93
3.17	Progressive degradation of correlation fringes due to phase vortex aberrations. The circles on the lower right corner of each pattern show the filter orientation that was used to generate the pattern. . . . .	93

3.18	Extracted phase in the case of a moderately aberrated phase vortex filter. It was obtained from the correlation fringe patterns of Fig. 3.17 and an algorithm based on Eq. (3.37). . . .	94
3.19	Experimental setup for out-of-plane displacement measurement using vortex filtering. . . . .	95
3.20	Experimental correlation pattern. . . . .	96
3.21	Displacement measurement. . . . .	96
4.1	Moiré Fringes. a) High frequency information with carrier, b)high frequency structured illumination pattern, c)low frequency Moiré fringes. . . . .	101
4.2	SIM analysis in the frequency domain. . . . .	102
4.3	Structured illumination. . . . .	103
4.4	Structured illumination projected over a 3D object. . . . .	103
4.5	Structured illumination projected over the object through the microscope objective. . . . .	104
4.6	Frequency spectrum of a 3D object illuminated with structured light. . . . .	105
4.7	Object propagation through the microscope. a)Original object, b)object seen with the microscope, c) frequency spectrum of the original object, d)frequency spectrum of the object seen through the microscope. . . . .	107
4.8	Structured illumination projected over an object and propagated through the microscope. a) Intensity distribution $I_1(x_i, y_i)$ , b)frequency spectrum of the intensity distribution $I_n(x_i, y_i)$ . . . . .	108
4.9	Spectrum of the isolated high frequency information a) Right information lobe $ \mathcal{F}\{\mathcal{I}_+(x, y)\} $ , b) left information lobe $ \mathcal{F}\{\mathcal{I}_-(x, y)\} $ . . . . .	109
4.10	Frequency response of $ G^3(\omega) ^2$ , orders 0,+1 and -1 are sketched in red. . . . .	111
4.11	Sketch of the spectrum of the isolated high frequency information without carrier. a)Right information lobe $ \mathcal{F}\{\mathcal{I}_+(x, y)\} $ , b) left information lobe $ \mathcal{F}\{\mathcal{I}_-(x, y)\} $ , c) translation of the high frequency information. . . . .	113
4.12	Simulation of the spectrum of the isolated high frequency information without carrier. a)Right information lobe $ \mathcal{J}_+(u, v) $ , b)left information lobe $ \mathcal{J}_-(u, v) $ , c)translation of the high frequency information $ \tilde{\mathcal{J}}_+(u, v) $ , d)translation of the high frequency information $ \tilde{\mathcal{J}}_-(u, v) $ . . . . .	116

4.13	Simulated super resolution image. a)Super resolution image $I_s(x, y)$ , b)reconstructed frequency spectrum, c)transversal cut section comparison between original object, object under the microscope and SIM reconstruction. . . . .	118
4.14	Diagram block of the algorithm for SIM. a)Capture algorithm, b)reconstruction algorithm. . . . .	119
4.15	Experimental setup for SIM microscopy. . . . .	120
4.16	Experimental illumination patterns projected over a stainless steel sample. a) $\theta_1 = 90^\circ$ , b) $\theta_2 = 54^\circ$ , c) $\theta_3 = 18^\circ$ , d) $\theta_4 = 342^\circ$ , and e) $\theta_5 = 306^\circ$ . . . . .	122
4.17	Evaluation of the point spread function of the microscope. a)Image of a flat surface for the PSF analysis , b) zoom of the image seen by the normal microscope, c) zoom of the image seen by the super resolution microscope. . . . .	123
4.18	Experimental measurement of the point spread function of the microscope. . . . .	124
4.19	Analysis of a test grid. a) Normal microscope, b)super resolution microscope, c)comparison of the profile of the images a) and b). . . . .	125
4.20	Inspected nanostructures generated by the ultrafast pulse laser. a)Impact analyzed using an optical microscope, b)nanostructures analyzed using an SEM. . . . .	126
4.21	Inspected nanostructures generated by the ultrafast pulse laser over stainless steel. a)Impact analyzed using an optical microscope, b) nanostructures analyzed using SIM. . . . .	127
4.22	Zoom over the selected area in Figure 4.22. a)Impact analyzed using an optical microscope, b)nanostructures analyzed using SIM. . . . .	128
4.23	Analyzed impact of a femtosecond laser using SIM. . . . .	129
4.24	Inspected nanostructures generated by the ultrafast pulse laser over stainless steel before ablation. a)Impact analyzed using an optical microscope, b) nanostructures analyzed using an SIM. . . . .	129
4.25	Comparison of the microscopy techniques by a transversal cut of the sample images shown in Fig. 4.24. . . . .	130
4.26	Inspection of nanostrucutres using white light. a)Impact analyzed using an optical microscope, b) nanostructures analyzed using an SIM, c)comparison of the microscopy techniques by a transversal cut of the sample. . . . .	131

4.27	Experimental Setup for inspection of nanostructures in real time. . . . .	132
4.28	Schematic of the ultrafast laser beam focused on the sample for real time inspection of the nanostructures. a)Size of the minimum spot focus on the sample, b) experimental setup. . . . .	133
4.29	LIPSS over stainless steel sample after 72 pulses. a)Sample seen through a traditional microscope, b)sample seen through SIM, c)sample seen through a SEM. . . . .	133
4.30	Evolution in time of LIPSS on a stainless steel sample with low fluence. . . . .	134
4.31	Transversal cut for analyze the time evolution of LIPSS on a stainless steel sample with low fluence. a) Comparison graph of the 21 profile of LIPSS over stainless steel low fluence regime, b)time evolution of the structures on stainless steel at low fluence. . . . .	135
4.32	Evolution in time of LIPSS on a stainless steel sample with high fluence, white mark on the first image to indicate a segment for analysis, presented on Fig. 4.33. . . . .	136
4.33	Transversal cut for analyze the time evolution of LIPSS on a stainless steel sample with high fluence. a) Comparison graph of the 8 profile of LIPSS over stainless steel low fluence regime, b) time evolution of the structures on stainless steel at high fluence, c) time evolution of the structures on stainless steel at high fluence on a color scale. . . . .	137





# LIST OF TABLES

1.1	Color ring color codes. . . . .	9
1.2	Commonly used LED for microscopy. . . . .	10
1.3	Microscopy techniques. . . . .	15
2.1	Dependance of the quality index and the number of steps of the MSSPF . . . . .	61
3.1	Coefficients of the low order polynomial that we used to rep- resent the wavefront aberration function of our LCoS. . . . .	92
4.1	Samples analyzed. . . . .	132



## SYMBOLS

Symbol	Description	Units
$\alpha_n$	phase rotation for vortex phase filtering	rad
$\beta$	orientation/direction	-
$\beta_\pi$	orientation	-
$\epsilon$	attenuation parameter	-
$f$	focal length	m
$\lambda$	wavelength	m
$m$	topological charge of the vortex phase filter	-
$\mathbf{R}$	Rotation matrix	-
$p$	number of steps of the Multi-step vortex phase filter	-
$\rho$	radial spatial frequency coordinate	rad/m
$\rho_o$	radius of the filter in spatial frequency units	m
$(u, v)$	spatial frequency coordinates	rad/m
$(x_o, y_o)$	cartesian coordinates at the object plane	m
$(x_i, y_i)$	cartesian coordinates at the image plane	m
$(x_f, y_f)$	cartesian coordinates at the frequency plane	m
$a_o(x_o, y_o)$	amplitude of the object wave field	-
$\varphi_o(x_o, y_o)$	phase of the object wave field	rad
$\Psi(u, v)$	vortex phase	rad
$\Psi_p(u, v)$	discrete or quantified multi-step phase filter with $p$ steps	rad

$P(x_o, y_o)$	generalized pupil function	-
$\mathbf{q}(x_o, y_o)$	quadrant vector (a vector with functions as components)	-
$U_o(x_o, y_o)$	complex object field field	-
$U_i(x_i, y_i)$	complex image field	-
$U_r(x_i, y_i)$	complex reference field	-
$G_f(u, v)$	spectrum of the object field bounded with the pupil function	-
$H(u, v)$	transfer function of the continuous vortex phase filter	-
$H_p(u, v)$	transfer function of the multi-step vortex phase filter	-
$H^c(u, v)$	transfer function of the continuous vortex phase filter with spatial carrier	-
$h(\mu, \nu)$	kernel of the continuous vortex phase filter	-
$h_p(\mu, \nu)$	kernel of the multi-step vortex phase filter	-
$I(x_i, y_i)$	intensity distribution	-

## MATHEMATICAL OPERATIONS

$\otimes$	convolution
$ ()$	absolute value
$[()$	floor function
$a \bmod b$	modulus operation $a$ modulus $b$
$\text{T}$	Transposition
$\mathcal{F}\{()\}$	Fourier Transform
$\mathcal{F}^{-1}\{()\}$	Inverse Fourier Transform
$\mathcal{H}_{\mathcal{R}}\{()\}$	Radial Hilbert Transform
$\mathcal{R}_{\mathbb{C}}\{()\}$	Riesz Transform with Complex Kernel



## ABBREVIATIONS

---

2D	Two Dimensional
3D	Three Dimensional
AFM	Atomic Force Microscopy
CCD	Charged-Couple Device
DIC	Differential Interference Contrast
DOE	Diffraction Optic Element
DM	Deformable Mirror
ESPI	Electronic Speckle Pattern Interferometry
FPALM	Fluorescence Photo-Activation Localization Microscopy
FWHM	Full Width at High Maximum
HDI	Hole Diffraction Interferometer
HT	Hilbert Transform
LCoS	Liquid Crystal in Silicon
MP	Magnification Power
MSSPF	Multi-step Spiral Phase Filter
NA	Numerical Aperture
OCT	Optical Coherence Tomography
OPD	Optical Path Difference
OTF	Optical Transfer Function
OTL	Optical Tube Length
PALM	Photo Activated Localization Microscopy
PCM	Phase Contrast Microscopy
PDI	Point Diffraction Interferometer
PSF	Point Spread Function

RESOLFT	REversible Saturable Optical Fluorescence Transitions
RHT	Radial Hilbert Transform
RT	Riesz Transform
SEM	Scanning Electron Microscopy
SHG	Second Harmonic Generation
SIM	Structured Illumination Microscopy
SLM	Spatial Light Modulator
SMLM	Single-Molecule Localization Microscopy
SPD	Spectral Precision Distance
SPF	Spiral Phase Filter
SPM	Spiral Phase Microscopy
STED	Stimulation Emission Depletion
STORM	Stochastic Optical Reconstruction Microscopy
THG	Third Harmonic Generation
TPA	Two Photon Absorption

---



## CHAPTER 0

# INTRODUCTION

### Contents

---

<b>0.1 Thesis scheme</b> . . . . .	<b>1</b>
<b>0.2 Contributions</b> . . . . .	<b>2</b>

---

## 0.1 Thesis scheme

The present work relates the effects of the modification on the optical microscope pupil for two particular cases

- Vortex phase filter**  $\left\{ \begin{array}{l} \text{Phase contrast microscopy} \\ \text{Speckle interferometry} \\ \text{Point diffraction interferometer} \end{array} \right.$
- Super resolution microscopy**

The first chapter gives an overview of the different optical microscopy techniques as well as some definitions that are useful for the construction of the microscopes. Chapters 2 focus on the use of the vortex phase filter; the analysis and construction of the quantitative phase contrast microscopy is described and the incorporation of the vortex into a point diffraction interferometer where a vortex phase filter is combined with an amplitude filter. The expansion of the use of the vortex filter on speckle interferometry can be found on chapter 3.

The second part of this work studies the effect of an extended pupil on the microscope. This extension generates a super resolution effect on the microscope (chapter 4). An optical setup is presented as well as the implementation of the microscope for the characterization of nano-structures generated over metallic sample caused by ultra-short laser pulses.

## 0.2 Contributions

With this work, the examination and development of a quantitative phase contrast microscope using multi-step vortex phase filters, and the construction and study of a super-resolution optical microscope is intended.

It is sought the construction of a quantitative phase contrast microscope based on phase filter. The phase filter consists in a quantized vortex type filter, called multi-step vortex filter. With this device the measurement of the object phase can be done by rotating vortex filter. Moreover, due to the capabilities of the vortex phase filter for phase measurement, the aim of this work is to expand its use over speckle interferometry and explore the applications of an hybrid amplitude-phase filter into a point diffraction interferometer.

The particular objective of building a super resolution optical microscope, is to observe the in-situ behavior of nano-structures generated by ultrafast laser pulses. Common techniques of optical super resolution microscopy normally use fluorescence effect by adding fluorophores to the sample. This work seeks to develop a super-resolve microscope able to work with specular samples.

## CHAPTER 1

# OPTICAL MICROSCOPY

### Contents

---

<b>1.1</b>	<b>Introduction</b>	<b>4</b>
<b>1.2</b>	<b>Microscope basics</b>	<b>5</b>
1.2.1	Microscope objective	5
1.2.2	Illumination	10
<b>1.3</b>	<b>Microscope resolution</b>	<b>12</b>
<b>1.4</b>	<b>Microscope techniques</b>	<b>15</b>
1.4.1	Phase contrast microscopy	15
1.4.2	Confocal microscopy	20
1.4.3	Microscopy based on nonlinear optics	21
1.4.4	Super resolution microscopy	23
1.4.5	Stimulated emission depletion microscopy	24
1.4.6	Stochastic super-resolution microscopy	26
1.4.7	Optical coherent tomography	27

---

Optical microscopy consists in a group of techniques based on optical elements, which are used to get a magnified image version of the objects that usually is not able to be identified by the human eye, because of its size. The objective of this chapter is to get an overview of basic optical microscopy concepts that will be applied in the further chapters.

The main concepts introduced in this chapter, are intended to review the microscope fundamental components and their operation. First the microscope objectives are discussed highlighting the most common types that can be found off-the shelf. Also guidelines are given to choose a particular objective that is suitable for objects of a given dimension and properties. Furthermore, a brief section on illumination is included in order to understand the basis of a microscope.

Additionally, the resolution of the microscope (Section 1.3) is described. Next, the most common microscopy techniques such as phase contrast microscopy (PCM), confocal microscopy, second harmonic generation microscopy (SHGM), super resolution microscopy and novel image techniques such as optical coherence tomography (OCT).

## 1.1 Introduction

It is part of the human nature to try to find out the composition of the things, meaning to see the smallest thing we can. But by using just the eye this can't be done. Thus, some optical elements were used to solve this problem. The simplest optical microscope that can be used to observe the microscopic samples is called "simple microscope" or "augment lens". This simple microscope has only a positive lens and its maximum amplification is  $\frac{25}{f} + 1$ . [1]. The main disadvantage of this simple microscope is that it requires a lens with a small focal length  $f$  to obtain a big amplification. Hence, if the required amplification can not be satisfied, a more complex setup has to be designed.

The first attempts to overcome this problem are attributed to Zacharias Hanssen in the year 1590. But the version of the microscope as we know it, was conceived by Galileo [2]. In Fig. 1.1 the schematic diagram of a compound microscope is shown. The compound microscope has mainly two blocks, the objective and the ocular. The objective creates an image placed among the objective and ocular, which is finally magnified by the ocular and the eye optics.

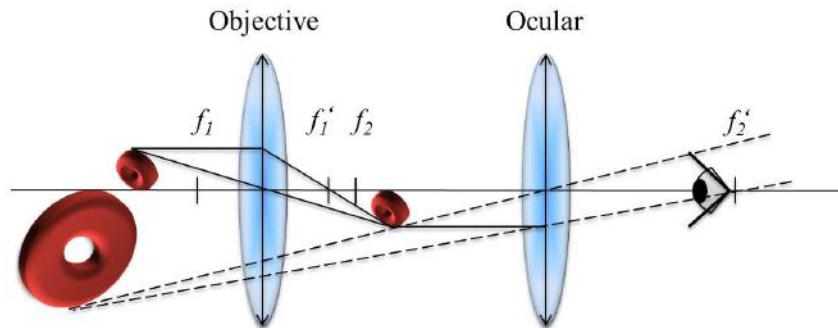


Figure 1.1. Compound microscope setup

Literature on microscopy techniques [3, 4, 5] is extensive, and covers a range of diverse applications. But recent developments tend to find procedures to extend the diffraction limit [6, 7, 8] to deal with biological tissues that are transparent [9, 10] or present scattering properties [11].

## 1.2 Microscope basics

Two main critical aspects that determine the microscope performance are: the objective lens, and the illumination that is to be applied on the microscope. In this subsection the principal parts of the microscope are analyzed in order to have a better understanding on the construction of an optical microscope.

### 1.2.1 Microscope objective

The core of the microscope is the objective, because is the responsible of creating a real image of object of interest so it can be projected by the ocular. The microscope objective gives the initial magnification of the microscope, and depending on the structure dimension of the sample that is under test an appropriate objective should be chosen so it could perform the magnification task. Not only the magnification of the microscope depends on the objective, but also the quality and resolution of the image. Objectives can be designed so optical aberrations are corrected or compensated, so the image of the object under suffers no distortion by optical aberrations. The construction of the microscope depends directly on the type of microscope objective that is chosen. Even though there are standards in the microscope objective manufacturers, there are certain differences among the main commercial brands, the following subsections show some of the most important differences.

#### 1.2.1.1 Types of objectives

There are two basic types of microscope objective: the first one is denominated finite tube microscope objective as it is shown in Fig 1.2a. The reason is that the tube length distance is finite. The objective forms the image of the object into the field stop. Then this intermediate image is used by the eyepiece to form the final image. For this configuration the parafocal

distance allows the interchange of objectives to zoom image without defocussing.

On the other hand, the infinity corrected microscope objective, creates the image of the object into the infinity, as shown in Fig 1.2b. For this configuration it is necessary to add a tube lens in order to focus the beam into the eyepiece and form the image. This type of microscope objective is used when there are some additional elements such as beam splitters or prisms in the microscope, also it can be used for coherent sources such as laser illumination as it is collimated.

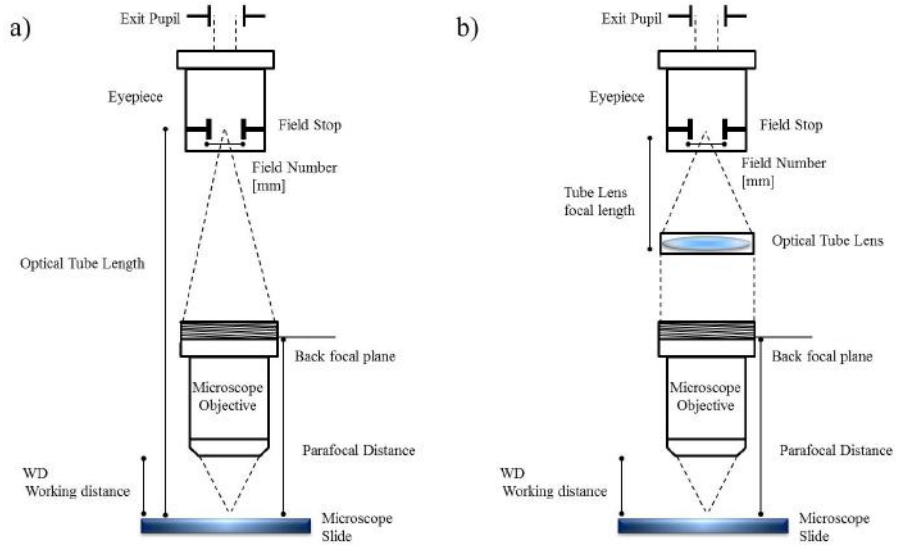


Figure 1.2. Types of objective. a)Finite tube length microscope objective, b)infinity corrected microscope objective.

It can be seen from Fig. 1.2a that finite tube length objective requires a specific optical tube length (OTL) in order to project the image on the eye-piece. This length is related with the absolute magnification of the objective  $M$  [12]

$$(1 + M) \approx \frac{OTL}{f_{\text{objective}}}, \quad (1.1)$$

where  $f_{\text{objective}}$  is the focal length of the microscope objective.

The focal tube lens is a parameter that is defined by the manufacturer in case of the infinity corrected system. For instance, the typical tube lens

focal length manufactured by Zeiss is 164.5 mm but for Olympus is 180 mm.[13, 14]. The magnification power (MP) of the microscope for this type of objective depends on the optical tube lens (OTL), which is the distance between the focal length of the objective and the eyepiece [15]. The magnifying power of the microscope can be calculated using,

$$MP_{\text{microscope}} = M_{\text{objective}} MP_{\text{eyepiece}} = -\frac{OTL}{f_{\text{objective}}} \frac{250 \text{ mm}}{f_{\text{eyepiece}}}. \quad (1.2)$$

The constant of 250 mm corresponds to the standard near position of the human vision which relates to a four diopters magnification.

### 1.2.1.2 Objective parameters

Beside the previous classification, microscope objective have some other important parameters that have to be taken into account for the application, usually a nomenclature printed on the objective is done in order to know this parameters as described in Fig. 1.3.



Figure 1.3. Typical microscope objective nomenclature.

The objective **maker** corresponds to the manufacturer of the microscope, such as Olympus or Zeiss. The label marked as **objective type** is the type of correction that is done to the objective such as Achromatic, Plan Achromatic, Fluor, Plan Fluor, Apochromat and Plan Apochromat. Depending on the type of aberration correction desired on the system the selection has to be made, being the Apochromat the most advanced objective, because they are usually chromatically corrected for the three colors, with spherical aberration corrected for at least two colors.

There are different objectives for each **application**, it is not the same to use an objective for bright field (H), than an objective for dark field (D). So there are also special objectives for differential interference contrast (DIC),

reflected light (R), phase contrast (PH) and polarization (P). The thickness of the **cover slip** is given in mm, when there is no cover slip a zero appears in the nomenclature, meanwhile a " - " is shown when the coverslip is optional. Also the **working distance** is given in millimeters, which is the distance between the surface of the front objective lens and the sample that is inspected.

One of the most important parameters of the microscope objective is the **numerical aperture** (NA), which is defined as

$$NA = n \sin(\theta) \quad (1.3)$$

where  $n$  is the refraction index of the medium, for microscopy the most common media are air (no marking), oil (Oil), water (W), or Glycerine. The value  $\theta$  corresponds to the half-angle of the maximum cone of light that can enter or exit the lens [2].

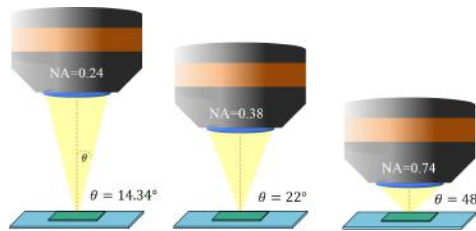


Figure 1.4. Numerical aperture of a microscope objective.

The numerical aperture can be translated as the amount of light that can be accepted to the system by the cone light that is formed by the angle. This number has no dimension and is straightforward related to the resolution of the optical system, it is desirable that the numerical aperture of the objective is almost one or bigger, it is related with the magnification and the working distance, for example if the magnification and the NA increases the working distance of the microscope will be reduced; this will be explained with further detail in the next section. From Fig. 1.4 it can be seen that the higher the value of the NA is, the angle is bigger and the distance between the objective and the sample is smaller. Meaning that for non-immersion objectives is quiet difficult to get values of  $NA$  bigger than 0.95

The **magnification** color ring, helps the manufacturer to identify the magnification. Table 1.1 shows the typical colors for Zeiss and Olympus manufacturers.



Table 1.1. Color ring color codes.

<b>Magnification</b>	<b>Zeiss</b>	<b>Olympus</b>
1x, 1.2x , 1.5x	Black	Black
2.5x	Brown	Brown or Orange
4x, 5x	Red	Red
1x, 1.2x , 1.5x	Black	Black
6.3x	Orange	-
10x	Yellow	Yellow
16x, 20x	Green	Green
25x, 32x	Green	Turquoise
40x, 50x	Light Blue	Light Blue
63x	Dark Blue	Dark Blue
>100x	White	White

## 1.2.2 Illumination

One of the most important aspects on microscopy is the illumination of the sample. One of the requirements to have a good inspection of the sample, is that the illumination should be uniform in all the field of view. Usually for the illumination it is used different kinds of lamps, such as the tungsten-argon and tungsten lamps. Nevertheless, LED (Light-Emitting Diode) illumination has been replacing the arc lamps due the long lifetime, reduced costs, and its compact design, moreover the LED illumination provides a narrow spectral band with different wavelengths as seen in Table 1.2.

Table 1.2. Commonly used LED for microscopy.

Wavelength (nm)	Color	Medium
380	UV	Diamond, boron nitride
455	Royal Blue	Indium gallium nitride (InGaN)
505	Cyan	Zinc selenide (ZnSe), indium gallium nitride (InGaN)
530	Green	Gallium(III) phosphide (GaP), aluminium gallium indium phosphide (AlGaInP)
590	Amber	Gallium arsenide phosphide (GaAsP), aluminium gallium indium phosphide (AlGaInP)
633	Red	Aluminium gallium arsenide (AlGaAs), gallium arsenide phosphide (GaAsP)
435 – 675	White Light	Blue/UV diode with yellow phosphor

### 1.2.2.1 Köhler Illumination

One of the biggest problem in microscopy is to achieve an even illumination in the sample. To achieve this August Köhler in the late 1800 developed a technique in order to have an even illumination in the sample [16]. Before Köhler illumination, the used illumination for microscopy was denominated *critical illumination* [17], the problem with this technique is that the lamp filament was imaged over the sample, producing unwanted patterns and an uneven illumination over the sample. The Köhler illumination setup is

shown in Fig. 1.5.

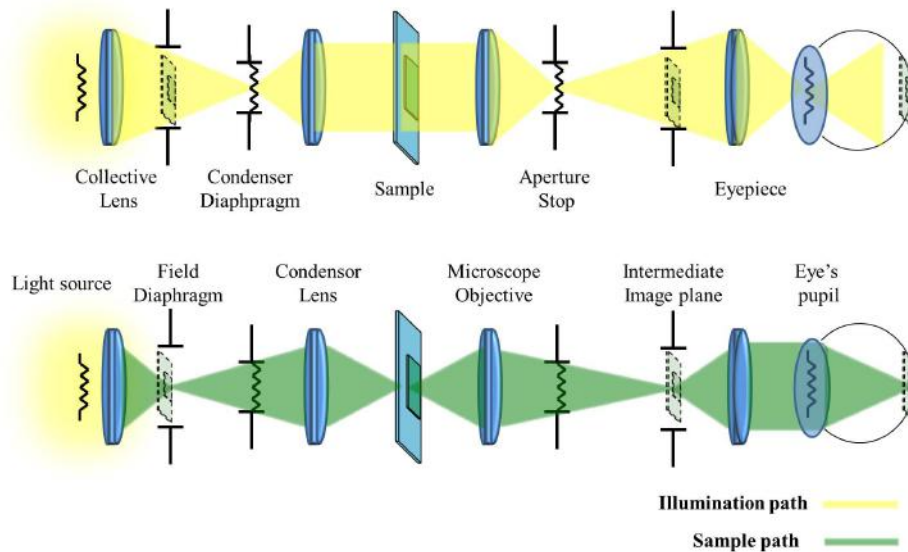


Figure 1.5. Köhler Illumination. Top diagram shows the illumination path in yellow, while the sample path shown in green can be seen on the bottom diagram.

The idea of this illumination is based on creating the image from the filament in the eye's pupil, in this way the filament won't be seen by the eye or in the camera detector. To achieve this even illumination, the source has to be focused by using a collective lens on a condenser diaphragm, which typically is open up to  $3/4$  parts of the lamp size. This acts like a source for the condenser lens, which collimate the light and project it to the sample; this can be shown in the illumination path from Fig. 1.5.

Once the specimen is well illuminated, the light transmitted is collected by the microscope objective, where the eyepiece creates the image of the sample over the eye. It can be seen that the alignment of this setup is critical, so microscopes that use this illumination technique require to be realigned with some regularity.

### 1.2.2.2 EPI Illumination

Typical Köhler illumination works only for transmission specimens, so in order to resolve this problem a variant of Köhler illumination has been proposed and called EPI illumination. This kind of illumination is used frequently for metallurgic samples or for thick opaque samples.

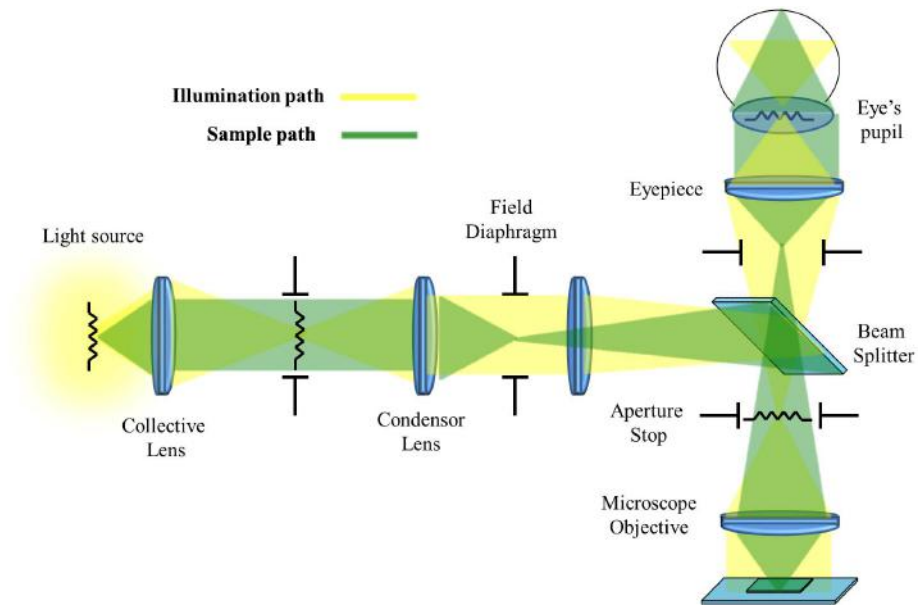


Figure 1.6. Epi Illumination.

This configuration can be seen on the schematic diagram shown in Fig. 1.6, it can be seen that an additional lens is used to focus the light over the back focal plane of the microscope objective, using this element also as part of the illumination. One disadvantage of this illumination is its alignment, every element should be precisely centered with the optical axis.

## 1.3 Microscope resolution

The resolution of an optical system can be defined in general terms as the minimum detail that can be analyzed by the system without aberrations and distortions. The light has its wave-particle duality, thus interference and diffraction phenomena are presented within. The diffraction can be de-

scribed as the deviation of the light from its path when there is no reflection or refraction involved [18].

Figure 1.7, shows the general diffraction diagram where the illumination source is perpendicular to the pupil. The electric field, which is shown in this figure, produced in the point  $P_o$ , with coordinates  $x_o, y_o$ . Which is generated by the pupil located in the plane  $u, v$  at a perpendicular distance  $z_o$ . The pupil has its transmittance function  $T(u, v)$ .

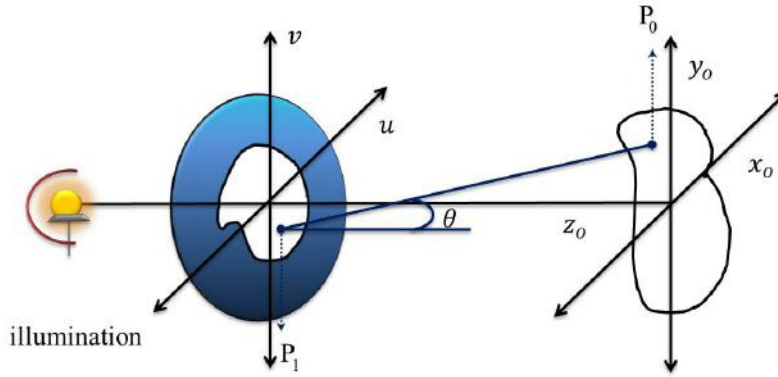


Figure 1.7. Diffraction effect in an arbitrary pupil.

Far field diffraction can be expressed using Eq. (1.4) known also as the Fraunhofer diffraction. It can be seen that the produced field is almost the Fourier transform of the pupil transmittance function multiplied by a square factor.

$$U_o(x_o, y_o) = \frac{\exp ikz \exp \frac{ik}{2z}(x_o^2 + y_o^2)}{i\lambda z} \int \int_{\text{Aperture}} T(u, v) \exp \left[ -i \frac{2\pi}{\lambda z} (x_o u + y_o v) \right] dudv, \quad (1.4)$$

where  $k$  is the wave number and  $\lambda$  is the wavelength of the incident light.

For instance, if the transmittance of the pupil is a circular aperture as shown in Fig 1.8a. The intensity of the produced electric field caused by diffraction can be seen in Fig 1.8b. This pattern corresponds to the normalized zero order Bessel function. This diffraction pattern is a function of the radius of the aperture and the propagation distance  $z$ .

The intensity distribution shown in Fig 1.8b is known as the Airy pattern.

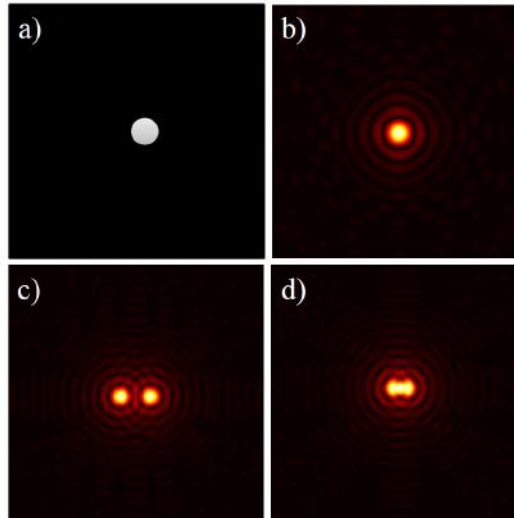


Figure 1.8. Fraunhofer diffraction for a circular aperture. a) Circular aperture, b) diffraction pattern of the circular aperture, c) diffraction pattern of two circular apertures separated over Rayleigh criteria, d) diffraction pattern of two circular apertures just in the Rayleigh criteria.

A very well-known characteristic of this distribution is the relation between the first lobe maximum and the first minimum of the function. This relation is important for the concept of resolution limit.

$$r_{\text{Airy}} = 0.61 \frac{\lambda}{NA}. \quad (1.5)$$

$NA$  corresponds to the numerical aperture of the system, which is related with the amount of light that can enter to an optical system.

The Rayleigh criterion mentions that two point sources can be resolved if they are separated by the resolution limit for a circular aperture. When the first maximum of the Airy pattern of the first point source coincides exactly with the first zero of the second source Airy distribution, this can be seen in Figs. 1.8c and d, where two circular apertures are illuminated for a distance bigger than the Rayleigh criteria and two other separated just by the criteria. This means that two objects can be resolved only if the separation between these elements is bigger than the mentioned in Eq. (1.5).

For a circular pupil, the diffraction pattern is not only present in the lateral direction  $(x, y)$  but also in the axial axis  $z$ . The concept of axial resolution is

the same as the lateral resolution, for this the relation between the distance in the axial minimum must be separate from the maximum according to Eq. (1.6) [19].

$$z_{\min} = 2 \frac{\lambda n}{NA^2}, \quad (1.6)$$

where  $n$  is the refractive index where the light propagates.

## 1.4 Microscope techniques

The selection of the microscope technique depends in the type of object that is under inspection and in the sample characteristics that are studied. For instance the technique is different if the analyzed object is an amplitude specimen, such as stained tissue, or a phase object like a bacteria or cells. Specimens can be also specular as metallurgic samples or mirrors like light diffusers such as fibers. Moreover, the sample can present some optical properties such as birefringence or fluorescence. In Table 1.3 a brief relation of the analyzed sample and the microscopy technique is presented [17] with the most common microscopy techniques.

Table 1.3. Microscopy techniques.

<b>Technique</b>	<b>Type of specimen</b>
Bright field	Amplitude, reflecting, diffuser
Dark field	Light scattering
Phase Contrast	Phase objects, scattering, light-refracting
Polarization Microscopy	Birefringence samples
Fluorescence Microscopy	Fluorescence samples
Confocal Microscopy	3D samples requiring optical sectioning
No linear Microscopy	Molecular dynamic of the sample
Super-resolution microscopy	Imaging beyond diffraction limit

### 1.4.1 Phase contrast microscopy

The simplified effect of light propagation through a transparent and opaque samples is shown in Fig 1.9. For an opaque sample the wave field is absorbed by the sample. Hence this light does not reach to the detector and the

image of the sample will be recorded as in bright field microscopy. But, for the transparent sample the detector will not notice any change on intensity. Because, the effect of the sample over the incident wave field is the alteration of the emerging wave field. This inconvenience can be overcome using phase contrast microscopy. The phase contrast microscope is a technique that allows the conversion of phase shift, caused by light through a transparent sample, to a brightness change in the receptor.

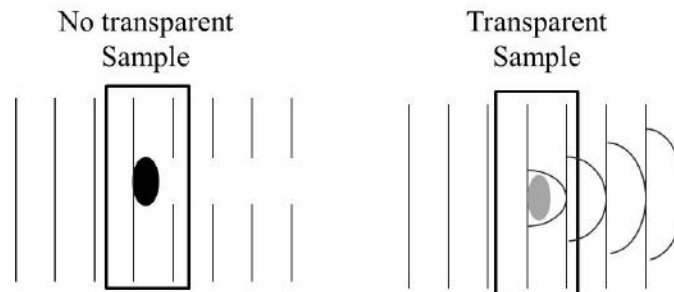


Figure 1.9. Effect of the light through no transparent and transparent samples.

Phase contrast microscopy has been popularised specially in the field of biology. With this technique, some cell structures can be seen and analyzed. Before this technique the biological samples were necessarily stained, this caused the alteration of the sample. Several techniques of phase contrast microscopy have been developed [3, 20]. In this section the conventional phase contrast microscopy and the spiral phase contrast microscopy are described.

#### 1.4.1.1 Fundamentals of phase contrast microscopy

Phase contrast microscopy (PCM) was invented by Frits Zernike in 1953. With this invention Zernike was awarded with the Nobel prize. To understand the principle of the PCM technique the effect of the light propagating of wavelength  $\lambda$  through a sample with refractive index  $n$  has to be analyzed. Fig. 1.10 shows the simplified version of a plane wavefront of wavelength  $\lambda$  propagating in the  $z$  direction, through a sample of phase difference  $\delta\varphi = k_z n z - \omega t$ , where  $z$  is the propagation distance,  $\omega$  is the angular frequency and  $t$  the time.



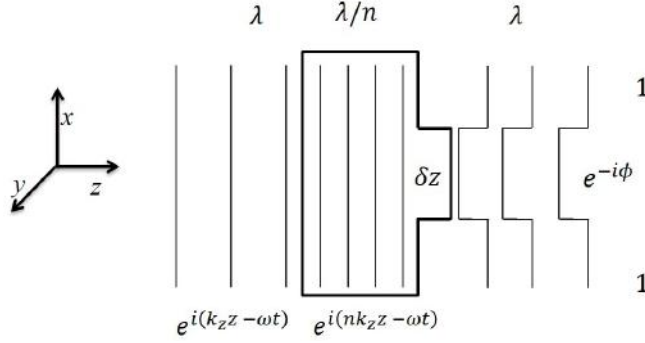


Figure 1.10. Propagation of a plane wavefront through a transparent sample.

The electric field  $E$ , resulting of the propagation for a transparent sample on free space can be expressed using Eq. (1.7). Where  $\delta\varphi$  corresponds to the optical path difference caused by the transparent sample.

$$E(z, t) = A(z, t)e^{-i\delta\varphi}, \quad (1.7)$$

and  $A(z, t)$  is the absorption of the object. Using Eq.(1.7) the intensity  $I$  recorded on the receptor can be observed in Eq. (1.8)

$$I = |E(t, z)|^2 \approx 1 + (\delta\varphi)^2 \quad (1.8)$$

From Eq.(1.8), can be observed that the term  $(\delta\varphi)^2$  corresponds to the diffracted light, and the "1" belongs to the direct light. The term  $(\delta\varphi)^2$  is too small, thus the receptor only sees the direct light. To solve this Zernike purposed the setup shown in Fig.1.11. A retarder phase plate of  $\pi/2$  with an amplitude value of  $\epsilon$  is placed in the Fourier plane, as shown in Fig. 1.11; this opaque phase plate decreases the amplitude of the wavefront between 10 and 30 percent of its original intensity [17]. This plate changes the phase of the diffracted light, this can be described using Eq. (1.9) [21]. Where it can be noticed that the term corresponding to the diffracted light is not as small as in Eq.(1.8). Thus, the implementation of a phase plate with an specific amplitude density  $\epsilon$ , raises the effect of the diffracted light rather than the direct. Allowing the inspection of the transparent specimen in the receptor.

$$I \approx \epsilon^2 - 2\epsilon\delta\varphi. \quad (1.9)$$

An inconvenience of the setup shown in Fig.1.11 is that the illumination required must be coherent. If a Köhler illumination (incoherent) is used,

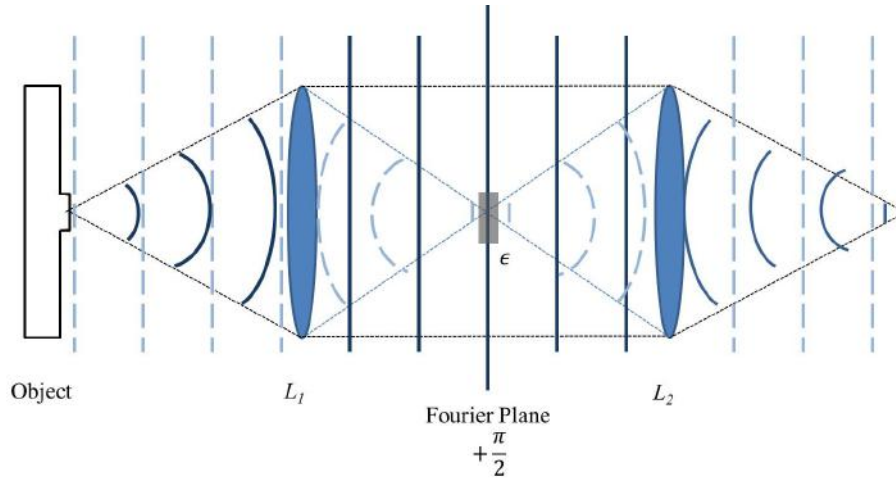


Figure 1.11. Phase contrast microscope with coherent illumination.

this technique is not useful. A pinhole can be implemented in the Köhler illumination but this dissipates a lot of light. To solve this problem an annular illumination has to be implemented. The setup is shown in Fig. 1.12 where an annulus is placed in the illumination before the the Köhler illumination, creating a partially coherent illumination. But in order to do this, the phase plate has to be modified as well. A phase shift ring plate has to be added as shown in Fig. 1.12.

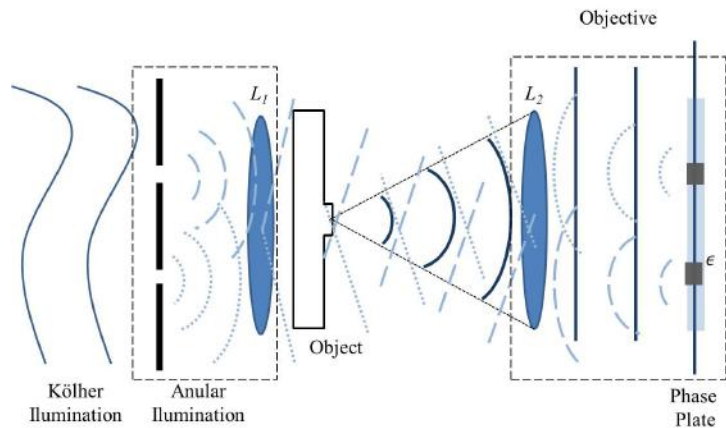


Figure 1.12. Phase contrast microscope with annular illumination.

The illumination of the phase contrast microscope consist of the annular disk and the condenser. Meanwhile the objective is formed of a second lens  $L_2$  and the phase shift ring plate. Hence, the illumination and the objective are not interchangeable with a bright field conventional microscope. Also, the selection of the ring plate phase shift depends on the desired contrast for the tissue image that is analyzed through the phase contrast microscope.

Using Zernike's setup is not the only way to achieve the phase contrast. There are different techniques that have advantages and disadvantages. For example the phase contrast technique can be done, using an special prism named "Nomarski Prism". This prism separates a polarized wave into two components, an S polarized and a circular one. This technique is called Nomarski Differential Interference Contrast (DIC) [20]. It is specially used for neuroscience application due the high contrast achieved [22].

The main limitation of these techniques is that they are only qualitative. This means that the phase can not be measured. Thus, other phase contrast techniques are required if a quantitative measurement is sought.

#### 1.4.1.2 **Spiral phase contrast microscopy**

The spiral phase contrast microscopy setup is shown in Fig. 1.13. This setup has the main advantage that it can quantify the phase of the sample [23] by rotating the spiral phase plate. (Spiral phase plate and vortex filtering are detailed in Chap. 2). It is observed that the configuration is similar to the Zernike configuration but instead of inserting a phase shift plate, a vortex spiral phase with carrier is used.

The Spiral Phase Microscopy (SPM) is an interferometric microscopy technique, which uses a spiral phase vortex with carrier projected over a spatial light modulator to change the phase of the object wavefront instead of the Zernike phase plate [24]. If the vortex phase filter is not implemented with a spatial carrier, a reference beam has to be added in order to create the interference. It is worth to emphasize that this technique is based on the Fourier filtering of the object. So, the implementation of spatial light modulator (SLM) for the filtering is quiet common [25].

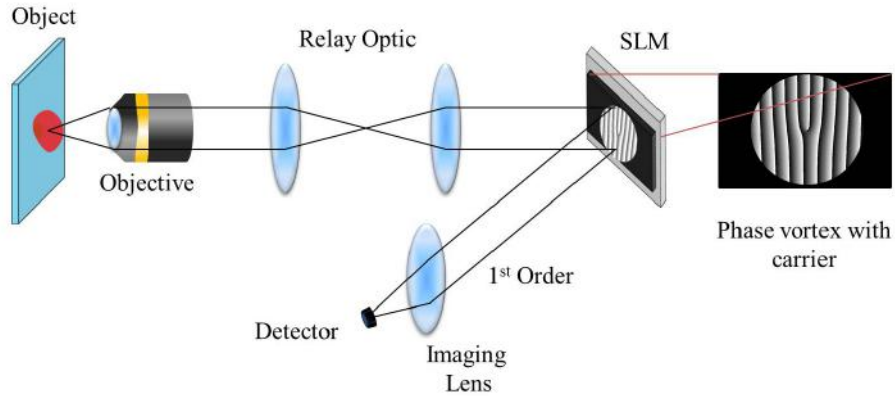


Figure 1.13. Phase spiral contrast microscopy.

#### 1.4.2 Confocal microscopy

This kind of microscopy was developed in 1957 by Marvin Minsk at the Harvard University [26]. This type of microscopy is a scanning type microscopy method, in which the sample, or the scanning area, are moved in a  $x - y$  plane to form a 2D image. The illumination of the microscope is limited by a pinhole which is frequently found in the microscope axis. The pinhole image is projected over the sample using a condenser lens. This punctual image is collected by the microscope objective which focuses the recollected photons to the detector, which can be a photomultiplier or a CCD.

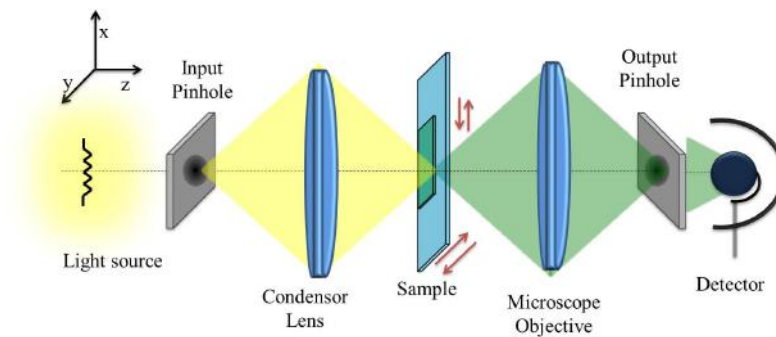


Figure 1.14. Typical confocal microscopy configuration.

Fig. 1.14 sketches the typical confocal microscopy configuration used for

samples which are analyzed by translating the sample in a  $x - y$  plane in order to scan a whole image. The main advantage of this microscopy technique is the enhancement of the specimen visibility; this effect happens due the scattering over the sample is lower than in traditional microscopy [27]. Another advantage of this technique is that a  $z$  scan can be performed over the sample allowing the reconstruction of the sample in 3D. Nevertheless, in order to reconstruct one sample, several images are needed as well as the application of post processing algorithms to the captured data. So, several modifications have been developed to this technique such as including scanning disc instead of pinholes, therefore the scanning of more points of the sample is simultaneously achieved [19].

### 1.4.3 Microscopy based on nonlinear optics

Nonlinear optic phenomena can be used to alter the optical properties of the inspected sample. However, the non-linear effects manifest themselves, only when high laser intensities are used to illuminate the sample. For microscopy, the non-linear response of the materials has been used to develop new imaging techniques.

The non-linear effect can be appreciated if the dipole polarization  $\tilde{P}(t)$  of any material is expressed as

$$\begin{aligned}\tilde{P}(t) &= \epsilon_0[\chi^{(1)}E(t) + \chi^{(2)}E^2(t) + \chi^{(3)}E^3(t) + \dots] \\ &= P^{(1)}(t) + P^{(2)}(t) + P^{(3)}(t) + \dots\end{aligned}\quad (1.10)$$

Where  $\epsilon_o$  is the permittivity in the vacuum and  $E(t)$  is the electric field which depends on time, and  $\chi$  is the electric susceptibility. Nonlinear microscopy uses the high order powers of the electric field ( $E^2, E^3, \dots$ ) in order to modify the optical properties of the sample by exciting the value of the high order electrical susceptibility terms ( $\chi^2, \chi^3, \dots$ ), and to analyse its structure.

Usually the most common nonlinear effects that are used in microscopy are second and third harmonic generation (SHG, THG) and two photon absorption (TPA). Fig. 1.15 shows the Jablonsky diagram for the different nonlinear optics process. For the second harmonic generation, two photons of frequency  $\omega$  incides to the sample generating a  $2\omega$  frequency photon. As well as for the third harmonic generation where three photons of frequency

$\omega$  incide to the sample generating a  $3\omega$  frequency photon. For the two photon absorption process two photons of  $\omega$  frequency imping to the sample generating a frequency less than  $2\omega$ . For instance on Fig. 1.15 if red light is used, SHG would generate blue light as is corresponds to  $2\omega$ , for the THG seen on Fig. 1.15b an ultraviolet emission can be seen as it is  $3\omega$ , finally a green light emission is seen on Fig. 1.15c where the light has a frequency  $> 2\omega$ .

The nonlinear optical microscopy generates better contrast than traditional microscopy in the images as it relies on the structure of the material and not in the reflected light, also it can give useful information on the behavior in some types of cells [28], because no extra pigmentation is used such as fluorophores [29]. The second harmonic generation gives information in the localization and orientation of the molecules which are under test, meanwhile the two photon absorption technique provides information about the molecule functionality which is also useful for deep tissue imaging [30].

The main disadvantages of this method is the high energy required in order to produce the non-linear effects, and that some samples do not present this effects. Center-symmetric materials do not generate second harmonics inside the material, just in the surface [31]. For example materials such as bones or dentine are capable of second harmonic generation [32].

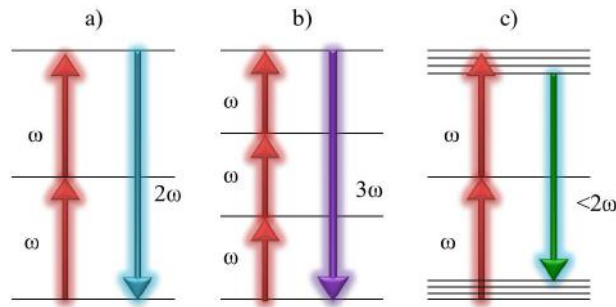


Figure 1.15. Representation of different nonlinear optics process. a)SHG, b)THG, c)TPA.

### 1.4.4 Super resolution microscopy

The super-resolution techniques are in charge of defining the characteristics of a system (the system can be optical, electric, mechanic) that hasn't been resolved [33]. For instance, for an optical system in which the diffraction effect is present. So the resolution of the system is a consequence of this effect, as seen in Eq. (1.5), known as the Rayleigh criteria. However, when the signal is captured by a CCD this device also has its own resolution; as the CCD has a size of the pixels that depends on the control electronics, the concept of super resolution can be extended as well for the electronic components of the system.

Nevertheless in this work, super-resolution will be defined as all the ensemble of the techniques that lead to surpass the Rayleigh criteria. Meaning that super resolution will be achieved when the diffraction caused by the optic pupil generates a PSF in which the ratio among the secondary maximum lobe and the center lobe of the PSF is lower than the PSF of the Airy distribution, this can be seen in Fig. 1.16.

Fig 1.16 shows the normalized PSF of a circular aperture represented by a blue line, and the PSF obtained after the introduction of a super resolution filter. Here we can observe that the PSF of the super-resolving filter shows secondary lobes with more energy than in the Airy distribution. In the other hand, the FWHM of the central lobe is reduced.

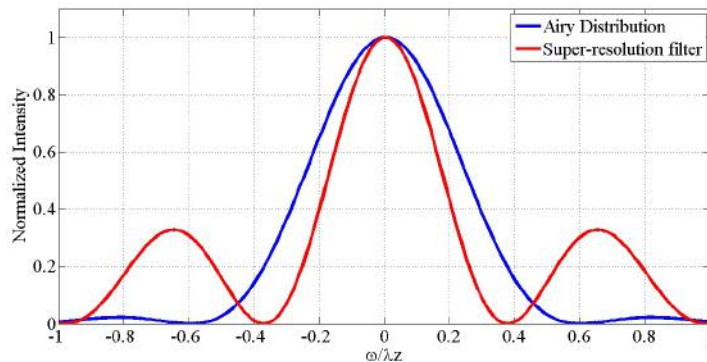


Figure 1.16. Point spread function of circular aperture and a super resolution filter.

As the Rayleigh criteria depends of the ratio between the central lobe and the secondary lobe of the PSF, and this ratio decreased when a super-resolved

filter is applied, the diffraction limit can be overcome. However the pupil of the system has to be different from a circular one, which generates the Airy pattern, this is called pupil engineering. The synthetic pupils can be designed as only phase pupils [34, 35], as is the case of binary phase filters [36] which can be easily displayed on spatial light modulators or a combination between amplitude and phase filters which offers advantages against only phase filters such as a better Strehel relation [37]. Using these techniques for different pupils, the resolution of the bright field microscope can be improved, this type of microscopy is also called spatially modulated illumination [38], surpassing the diffraction limit up to 50 nm [38].

Besides pupil engineering there are different super resolution techniques which use different optical principles. For instance Near-field scanning optical microscope (NSOM), which uses the evanescent waves in order to get super resolution information. By using this technique nanostructures up to 20 nm can be measured [39]. A disadvantage of this technique is that fluorescence has to be present on the sample and feedback with an atomic force microscope probe has to be done, so a lot of time is spent during the scanning process.

There are other techniques such as Structured illumination microscopy (SIM), which projects a sinusoidal pattern over the sample and by measuring the Moiré the super resolution is achieved [40] (further explanation in chapter 4 will be provided).

### 1.4.5 Stimulated emission depletion microscopy

Even if confocal microscopy has advantages over the traditional microscopy; it presents some disadvantages such as losses of the light caused by the pupil aperture. Stimulated Emission Depletion (STED) microscopy is a super resolution technique based on functional groups of molecules that show fluorescence called fluorophores. STED microscopy uses the principle from the super resolution microscopy technique called reversible saturable optical fluorescent transition (RESOLFT) microscopy [41] but using this special molecules. The conventional energy diagram of the fluorophore is presented in Fig 1.17. where the ground level corresponds to  $S_0$ , and the first electronic state  $S_1$ . Level  $L_0$  corresponds to a low vibrational state of  $S_0$ ; while  $L_1$  corresponds to the directly excited level of  $S_1$ . Also we can find the level  $S_2$  which corresponds to the relaxed vibrational stage of  $S_1$ , and  $L_3$  is the high level of  $S_0$  [42].



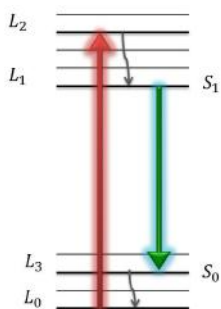


Figure 1.17. Energy levels of a typical Fluorophore.

Figure 1.18 an schematic diagram of the optical setup used for STED microscopy. The objective of this microscopy technique is to have an excitation pulse, which makes that the fluorophores generates an energy transition from level  $L_0$  to  $L_1$  (fluorescence emission); however, before the fluorophore starts the fluorescence process, a reduction in the energy level it's applied over the fluorophores using a depletion pulse called STED pulse. For the technique circular pupils are used so the point spread function of the circular pupil is projected over the fluorophores. As the reduction of the fluorescence is achieved over a non-depleted zone, a smaller fluorescent area beyond the diffraction limit can be analyzed. The region with more intensity is projected over the analyzed molecule or specimen; thus a better resolution is obtained. By itself the STED microscopy technique can achieve a lateral resolution of 20 nm [43], being acknowledge with the chemistry 2014 Nobel prize.

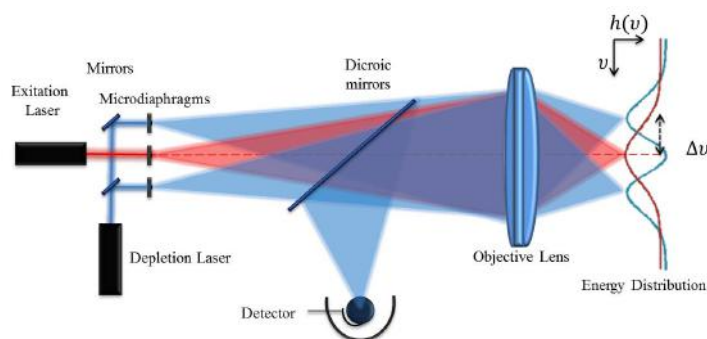


Figure 1.18. Optical setup for STED microscopy.

The STED technique shown in Fig. 1.18 can be combined with other techniques, such as the confocal microscopy, to obtain axial resolution improvement [44].

#### 1.4.6 Stochastic super-resolution microscopy

There are alternative super-resolution microscopy techniques that use the structure of the molecule with fluorophores and stochastic approaches to reconstruct a super-resolved element. This techniques illuminates single spots. Only a single isolated elements can be register at one time because they are separated within a region determined by diffraction limit (around 200-250nm diameter). The molecules or fluorophores are excited at separate times thereby this techniques are resolved in time. The first technique is called single-molecule localization microscopy (SMLM) [45], where other variations have been studied

- **SPD:** Spectral precision distance microscopy, is a fluorescence microscopy technique that is used form measure the distance, position and angle of optical isolated elements [46], using different colors and markers analyzed by its spectral domain, resolution achieved using this technique can be over 50 nm [47, 48].
- **STORM:** Stochastic optical reconstruction microscopy is based on time-resolved and sequential effect of fluorescent which is result of attaching Cy5 and Cy3 dyes to nucleic acids or proteins of the sample that is under analysis. The sample is illuminated so the position of the single spot centroids are determined and then deactivated, and so on until the whole image is scanned to create high resolution images for this technique. The type of dyes are the principal difference with other stochastic microscopy techniques, achieving up to 40 nm. for spatial resolution [49].
- **PALM and FPALM:** Photo activated localization microscopy and fluorescence photo-activation localization microscopy are based on the sequential activation and time-resolved localization of photoswitchable fluorophores instead of the dyes as in STORM. The principle is the same of activation localization and deactivation of a single spot, but these techniques are based on the use of fluorophores and fluorescent proteins [50, 51], being able to measure structures up to 10 nm for spatial resolution [6].

### 1.4.7 Optical coherent tomography

Optical coherent tomography (OCT) is an optical imaging technique frequently used in biomedical optics and medicine. It has been used due to its capabilities of obtaining cross sectional imaging of the internal microstructure of the analyzed sample, with almost one or two orders of magnitude resolution improvement than conventional ultrasound imaging techniques. This can be seen in Fig 1.19, where a comparison of the resolution and imaging depth of microscopy and ultrasound is shown. The axial image-resolution in OCT ranges from 1 – 5  $\mu\text{m}$ , and is determined by the coherence length of the light source [52, 53]. Meanwhile the imaging depth is usually limited to 2-3 mm, by the attenuation generated by optical scattering, in contrast with confocal microscopy where the light penetration limits the depth imaging. [54].

This technique provides information by measuring the magnitude and echo time delay of the backscattered light; producing a two dimensional data set which represent the optical backscattering in a cross sectional plane through the analyzed sample. OCT can be applied in-situ visualization of tissue microstructures without the need of removal and processing of specimens, gaining an important market in biological applications [55, 56, 57].

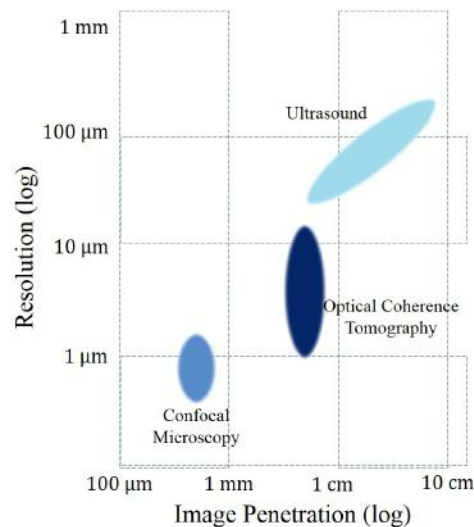


Figure 1.19. Comparison of resolution and imaging depth for ultrasound, OCT and confocal microscopy.



## CHAPTER 2

# PHASE CONTRAST QUANTITATIVE MICROSCOPY BASED ON OPTICAL VORTEX FILTERING

### Contents

---

<b>2.1</b>	<b>Introduction</b>	<b>31</b>
<b>2.2</b>	<b>Vortex phase filter</b>	<b>32</b>
2.2.1	Continuous vortex filter	32
2.2.2	Multi-step vortex filter	36
<b>2.3</b>	<b>Vortex phase filter interference</b>	<b>45</b>
2.3.1	Weak phase objects	46
2.3.2	Strong phase objects	50
<b>2.4</b>	<b>Phase extraction using vortex rotation</b>	<b>56</b>
<b>2.5</b>	<b>Numerical simulation</b>	<b>57</b>
2.5.1	Spiral fringe patterns	58
2.5.2	Phase contrast patterns	59
2.5.3	Effect of incrementing the number of steps in the extracted phase	60
<b>2.6</b>	<b>Experimental results</b>	<b>61</b>
<b>2.7</b>	<b>Point diffraction interferometer with spiral carrier</b>	<b>64</b>
2.7.1	Phase extraction	68
<b>2.8</b>	<b>Conclusions</b>	<b>69</b>

---

A vortex is an optical singularity that presents a phase dislocation in the wavefront [58]. The optical vortex is also known as phase rotor or spiral phase. Vortex wavefronts have been used for trapping particles [59]. By

taking advantage of this dislocation, the optical vortex induces an orbital angular momentum, thus it can be used as optical tweezers [60, 61]. Nevertheless, the aim of this work, was to use the optical vortex as a Fourier filter. The effects introduced by the vortex filtering depend on the input wavefront that is filtered. The kind of input wavefronts that are analyzed in this chapter for phase samples are produced by:

- Weak phase objects: with wavefront changes of less than  $2\pi$ .
- Strong phase objects and scattered objects: with phase changes greater than  $2\pi$ .
- Scattering phase objects: with random phase changes greater than  $2\pi$ .

The Fourier filter can also be made with a variety of vortices, in our work the multi-step vortex has been introduced as a practical filter to reduce manufacturing errors. Additionally, the interferometric effects of the filtered wavefront and a reference beam and the phase extraction techniques are discussed as well in this chapter.

## 2.1 Introduction

The spatial filtering process can be done using a  $4-f$  optical system as shown in Fig. 2.1. The wavefront field in the image plane  $U_i(x_i, y_i)$  can be described by Eq. (2.1).

$$U_i(x_i, y_i) = \mathcal{F}^{-1}\{\mathbf{H}(u, v)\mathcal{F}\{P(x_o, y_o)U_o(x_o, y_o)\}\}. \quad (2.1)$$

Where  $\mathcal{F}$  and  $\mathcal{F}^{-1}$  are, respectively, the forward and inverse Fourier transform operators,

$$U_o(x_o, y_o) = a_o(x_o, y_o) \exp[i\varphi_o(x_o, y_o)], \quad (2.2)$$

is the object complex amplitude distribution,  $P(x_o, y_o)$  is the generalized pupil function, and  $\mathbf{H}(u, v)$  is the transfer function of the filter where

$$\mathbf{H}(u, v) = \mathbf{H}\left(\frac{x_f}{\lambda f}, \frac{y_f}{\lambda f}\right), \quad (2.3)$$

and  $(x_f, y_f)$  are Cartesian coordinates at the spatial frequency plane,  $f$  is the focal length of the Fourier transforming lens, and  $\lambda$  the illumination wavelength. The amplitude  $a_o(x_o, y_o)$  and the phase  $\varphi_o(x_o, y_o)$  in Eq. (2.2) depend of the object analyzed.

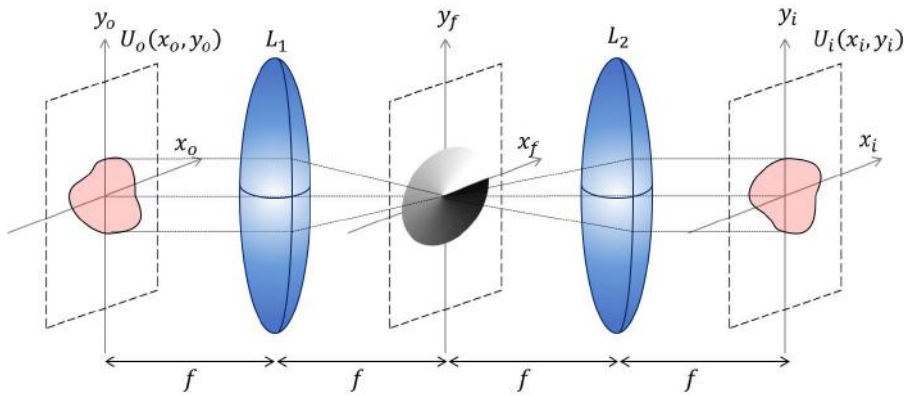


Figure 2.1.  $4-f$  correlator.

The filtering operation can be easily implemented in a  $4f$  optical system, in which a filter  $\mathbf{H}(u, v)$  is inserted as shown in Fig. 2.1. In this system the Fourier transform of the complex distribution  $P(x_o, y_o)U_o(x_o, y_o)$ , generated

by coherent light scattered from a surface at the object plane  $(x_o, y_o)$ , and bounded by pupil function  $P(x_o, y_o)$ , is obtained at the back focal plane  $(x_f, y_f)$  of the lens  $L_1$ . The filter, adds its phase to the phase of the spectrum  $\mathbf{G}_f = \mathcal{F}\{P(x_o, y_o)U_o(x_o, y_o)\}$ , and the resulting complex field is a Fourier transformed by lens  $L_2$  to generate a filtered wavefront in the image plane  $(x_i, y_i)$ . In the following section (Sec. 2.2) the filter  $\mathbf{H}(u, v)$  is described as a vortex phase filter. In the description it is assumed that the object is placed at the front focal plane of the Fourier transforming lens, and that vignetting is neglected. Additionally in Sec. 2.3 the interference of the field  $U_i(x_i, y_i)$  with a reference wave field is analyzed.

## 2.2 Vortex phase filter

The vortex phase filter can be described as

$$\mathbf{H}(u, v) = \text{circ}\left(\frac{\rho}{\rho_0}\right) \exp[i\Psi(u, v)], \quad (2.4)$$

where  $\Psi(u, v)$  is the vortex phase as a function of spatial frequencies  $(u, v)$ . Furthermore,  $\rho = \sqrt{u^2 + v^2}$  and  $\rho_0$  is the radius of the filter in spatial frequency units. The term  $\text{circ}\left(\frac{\rho}{\rho_0}\right)$  is the amplitude of the filter, this is used in case the filter has a circular pupil otherwise the amplitude is unitary. The function  $\text{circ}\left(\frac{\rho}{\rho_0}\right) = 1$  if  $\rho \leq \rho_0$ , if not; it is zero. The vortex phase can be divided in two:

- Continuous Phase Vortex
- Multi-Step Phase Vortex.

In subsections 2.2.1 and 2.2.2 each case will be discussed in detail.

### 2.2.1 Continuous vortex filter

The continuous spiral phase vortex is shown in Fig. 2.2. This vortex can be treated as an operator of the radial Hilbert transform [62]. It has the property that is a direct 2-D quadrature operator, because if a transversal cut is done to the vortex phase, each cut behaves as signum function. The vortex function is defined by [63]



$$H(u, v) = \frac{u + iv}{\sqrt{u^2 + v^2}}. \quad (2.5)$$

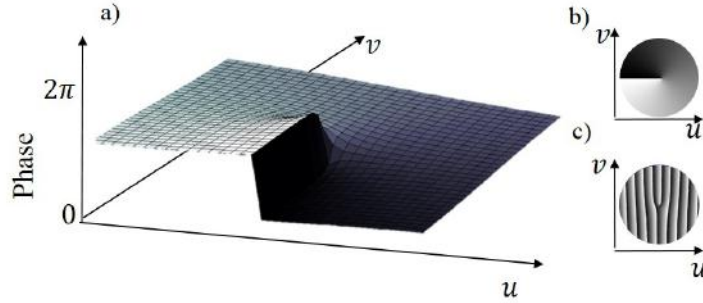


Figure 2.2. Phase vortex. a) Mesh plot of a phase vortex, b) 2D image of a phase vortex with phase coded only in gray levels, c) 2D image of a phase vortex with carrier phase coded only in gray levels.

Even though the vortex operator can be treated as a 2-D radial Hilbert operator, also called radial Hilbert transform [62], the correct approach is to consider the vortex as an operator of the Riesz transform [64] whose kernel  $h(x_i, y_i)$  is complex [63] as shown in Eq. (2.6)

$$h(x_i, y_i) = \frac{i(x_i + iy_i)}{2\pi(x_i^2 + y_i^2)^{3/2}}. \quad (2.6)$$

The point spread function (PSF) of the vortex filter can be seen in Fig. 2.3.

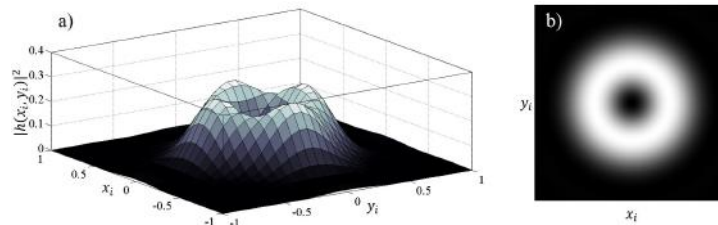


Figure 2.3. Point spread function of the optical vortex  $|h(x_i, y_i)|^2$ . a) Surface of the PSF, b) upper view gray representation of the PSF.

Due to the radial nature of the vortex filter, it is common to rewrite Eq. (2.5) and (2.6) in polar coordinates.

$$H(u, v) = \exp[i\phi(u, v)] \quad (2.7)$$

$$h(x_i, y_i) = \frac{i \exp(i\theta(x_i, y_i))}{2\pi r^2}, \quad (2.8)$$

Where  $\phi(u, v)$  is the polar angle in frequency space. The spatial polar coordinates are defined as usual:

$$x_i = r \cos \theta, y_i = r \sin \theta. \quad (2.9)$$

If Eq. (2.4) and (2.7) are compared. It can be noticed that for the continuous vortex with no carrier

$$\phi(u, v) = \Psi(u, v), \quad (2.10)$$

Thus, the phase of the filter changes as shown in Fig. 2.2a).

Commonly a topological charge  $m$  can be introduced to the vortex phase, this topological charge introduces a momentum to the propagated wave [65], it has some interesting applications in communications and quantum applications[66]. Eq. (2.11) shows the equation of the vortex filter when a topological charge  $m$  is added, where  $m \in \mathbb{R}$ . Furthermore, the effect of this topological charge is reflected in Fig.2.4.

$$H(u, v) = \exp[im\phi(u, v)]. \quad (2.11)$$

The topological charge can be modified to produce the fractional Hilbert transform [62, 67]. This can be used to implement a selective edge in the resultant image of the filter. If  $m < 1$ , the right hand edge is emphasized, if  $m = 1$  (radial Hilbert transform or Riesz transform with complex kernel) both edges are emphasized, and when  $m > 1$  the left-handed edges are emphasized.

The vortex filtering process of a function  $g_o(x_o, y_o)$  can be expressed as

$$\begin{aligned} \mathcal{H}_{\mathcal{R}}\{g(x_o, y_o)\} &= \mathcal{F}^{-1}\{\mathcal{F}\{g_o(x_o, y_o)\}H(u, v)\} \\ &= g_o(x_i, y_i) \otimes h(x_i, y_i) \\ &= \mathcal{R}_{\mathbb{C}}\{g(x_o, y_o)\}. \end{aligned} \quad (2.12)$$

Where  $\mathcal{H}_{\mathcal{R}}$  is the Radial Hilbert (RHT) transform operation,  $\otimes$  stands for the convolution operation and  $\mathcal{R}_{\mathbb{C}}$  is the Riesz Transform with complex kernel operation when  $m = 1$ .

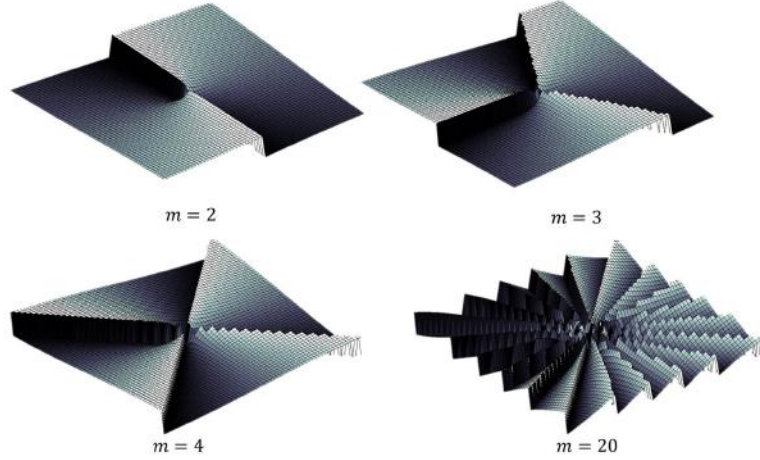


Figure 2.4. Vortex phase filter with different topological charges  $m$ .

### 2.2.1.1 Vortex phase rotation

When a constant phase  $\alpha_n$  is added to the filter as shown in Eq. (2.13), the wrapped phase can be seen as a rotation of the original phase vortex filter. This effect is displayed in Fig.2.5. This phase rotation can be implemented as well for vortices with different topological charge.

$$\begin{aligned} H^{(n)}(u, v) &= \exp[im\phi(u, v)] \exp[i\alpha_n] \\ &= H(u, v) \exp[i\alpha_n]. \end{aligned} \quad (2.13)$$

Where  $\alpha_n \in \mathbb{R}$ , this means that the phase rotation can be done depending on the rotation sensibility of the device in which the filter is implemented.

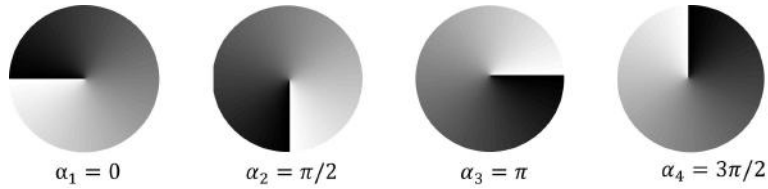


Figure 2.5. Vortex phase rotation.

### 2.2.1.2 Vortex phase filter with carrier

The vortex phase filter can be modulated with a spatial linear carrier, as shown in Fig.2.6. A "fork" shape figure usually appears in the modulated vortex phase.

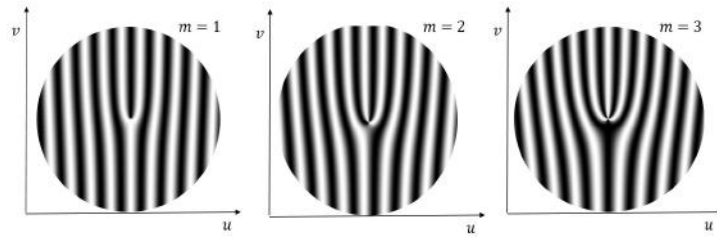


Figure 2.6. Gray level representation of the vortex phase filter with spatial carrier, where the maximum phase (white) corresponds to  $2\pi$  and zero phase is represented on black.

When the carrier is added to the filter, it can be expressed as:

$$H^c(u, v) = \exp [i \cos (m\phi(u, v) + Tu)], \quad (2.14)$$

in this equation,  $T$  is the period of the carrier expressed on  $m$ , this period modifies the number of fringes that the filter has. The carrier can be orientated in any direction using a linear combination of  $u$  and  $v$ . It can be noticed that the carrier filter is not limited to a topological charge of one. However, when the topological charge is increased, an addition of the "fork" branches is anticipated.

The purpose of introducing this modulation, is to obtain the vortex PSF in the diffraction orders  $+1$  or  $-1$  as shown un Fig. 2.7. The main disadvantage of using this kind of filter is that most of the energy is distributed on the zero order.

### 2.2.2 Multi-step vortex filter

In practice, small angular phase increments, like those to produce acceptable continuous vortices, are difficult to make with digital devices. They have been made with deformable mirrors [68], and also with digital SLMs, mainly

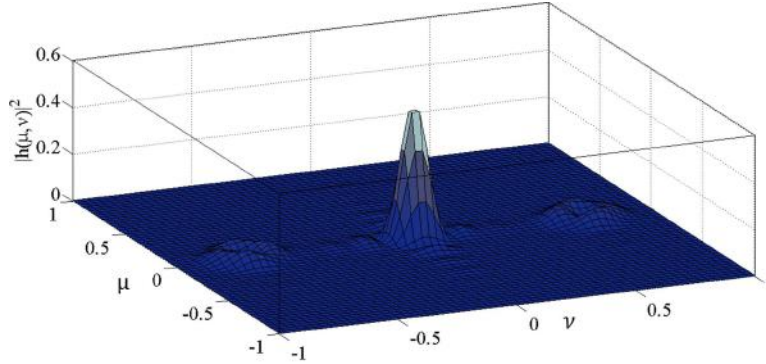


Figure 2.7. Vortex phase filter with spatial carrier PSF.

LCoS [24], and more recently with digital micro-mirror devices (DMD) [69]. To work out this inconvenience, a discrete vortex phase filter was proposed [70]. This discrete vortex has  $p$ -steps that resembles a "snail stair".

We named it as multi-step spiral phase filter (MSSPF) that can be seen as a quantized version of a continuous spiral phase filter of unitary topological charge (SPF). The continuous spiral phase of the filter is usually discretized into a  $p$ -steps of the vortex phase. The transfer function of the generalized MSSPF can be expressed as:

$$\mathbb{H}_p^{(n)}(u, v) = \text{circ}\left(\frac{\rho}{\rho_o}\right) \exp[i\Psi_p^{(n)}(u, v)], \quad (2.15)$$

where  $(u, v)$  are the spatial frequency coordinates,  $\rho = \sqrt{u^2 + v^2}$ ,  $\rho_o$  is the radius of the filter in spatial frequency units, and  $p$  represents the number of the filter steps (or quadrants for  $p = 4$ ), with the restriction that  $p \in \mathbb{N}$ , where  $\mathbb{N}$  is the set of all natural numbers. As usual  $\text{circ}(\rho/\rho_o) = 1$  if  $\rho \leq \rho_o$ . The MSSPF depends on  $n$ , which represents the multiple combinations that the orientation of the major vortex discontinuity can represent, where  $n \leq p$ . Each discretized filter can have  $n$  orientations; the possible phase configuration for each MSSPF can be represented as:

$$\begin{aligned}\Psi_p(u, v) &= \left[ \Psi_p^{(1)}(u, v), \Psi_p^{(2)}(u, v), \dots, \Psi_p^{(n)}(u, v) \right]^T \\ &= \frac{2\pi}{p} \mathbf{R} \mathbf{q}_p(u, v),\end{aligned}\quad (2.16)$$

where the symbol  $T$  denotes transposition,

$$\begin{aligned}\mathbf{R} &= [r_{i,j}] \\ &= [\mathbf{r}_1, \mathbf{r}_2, \dots, \mathbf{r}_p]^T \\ &= \begin{pmatrix} 0 & 1 & 2 & \dots & p-1 \\ p-1 & 0 & 1 & \dots & p-2 \\ \vdots & & \ddots & & \vdots \\ 2 & \dots & p-1 & 0 & 1 \\ 1 & 2 & \dots & p-1 & 0 \end{pmatrix},\end{aligned}\quad (2.17)$$

and

$$\mathbf{q}_p(u, v) = [q_1(u, v), q_2(u, v), \dots, q_j(u, v)]^T, \quad (2.18)$$

here we refer to  $\mathbf{q}_p(u, v)$  as the step level vector (a vector whose elements are functions), with  $j \leq p$ , and to  $\mathbf{R}$  as the vortex rotation matrix. Notice, from Eq. (2.16) that the maximum phase of the MSSPF is not  $2\pi$ , as for the SPF, but  $\frac{2\pi(p-1)}{p}$ . This implies that, the MSSPF requires less phase modulation than the continuous spiral phase plate.

The step level function  $q_j(u, v)$  is defined as:

$$q_j(u, v) = \begin{cases} 1 & \frac{2\pi(j-1)}{p} < \theta \leq \frac{2\pi j}{p}, \\ 0 & \text{otherwise} \end{cases}, \quad (2.19)$$

where  $\theta = \tan^{-1}(v/u)$  is the angular polar coordinate. The step level function is a radial variation of the Heaviside function  $H(u) = 1$  if  $u > 0$  otherwise is 0. A special characteristic of the step level vector is that the sum of its components is one for all the function domain,  $\sum_{j=1}^p q_j(u, v) = 1$ .

Using Eqs. (2.16) and (2.19), Eq.(2.15) can be expressed as:

$$\mathbb{H}_p^{(n)}(u, v) = \text{circ} \left( \frac{\rho}{\rho_o} \right) \exp \left[ i \frac{2\pi}{p} \sum_{j=1}^p r_{n,j} q_j(u, v) \right], \quad (2.20)$$

taking into count that

$$r_{n,j} = r_{1,j} + n - 1 \quad \text{mod } p, \quad (2.21)$$

The  $n^{\text{th}}$  filter can be rewritten as:

$$\begin{aligned} \mathbb{H}_p^{(n)}(u, v) &= \text{circ}\left(\frac{\rho}{\rho_o}\right) \exp[i\Psi_p^{(1)}(u, v)] \\ &\times \exp\left[i\frac{2\pi(n-1)}{p} \sum_{j=1}^p q_j(u, v)\right] \\ &= \text{circ}\left(\frac{\rho}{\rho_o}\right) \exp\left[i\frac{2\pi(n-1)}{p}\right] \mathbb{H}_p^{(1)}(u, v), \end{aligned} \quad (2.22)$$

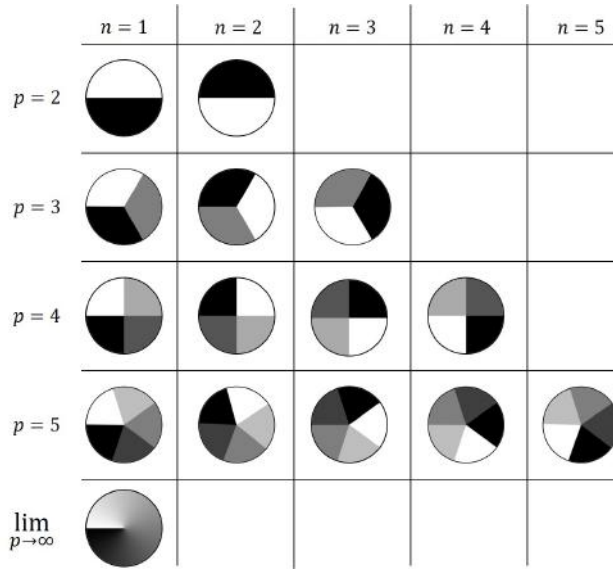


Figure 2.8. Phase of the MSSPF with variation of the  $n$  and  $p$  parameters.

Thus the  $n^{\text{th}}$  filter can be expressed as a combination of the filter, whose orientation of the major discontinuity coincides with the axis  $\theta = 0$ , and a multiplicative factor that only depends on  $n$ . This factor provides the effect of rotation for the different multi-steps spiral phase filters. The effect of varying the parameters  $p$  and  $n$  are sketched in Fig. 2.8. When  $p$  approaches to  $\infty$  the MSSPF becomes the well known spiral phase filter, with topological charge of one.

The convolution kernel  $h_p(x_i, y_i)$  of the MSSPF should be described in order to know the performance of the filter. To calculate this kernel, the Fourier transform is applied to the phase filter  $H_p(u, v)$ :

$$h_p(x_i, y_i) = \mathcal{F}^{-1} \{ \mathbb{H}_p(u, v) \}, \quad (2.23)$$

where  $\mathcal{F}$  and  $\mathcal{F}^{-1}$  are, respectively, the forward and inverse Fourier transform operators. The computed point spread functions (PSF) of the  $p$ -MSSPF ( $|h_p(x_i, y_i)|^2$ ) are shown in Fig. 2.9. The number of lobulus in the PSFs of the MSSPFs increases as the number of steps  $p$  grows; until it reaches the typical doughnut kernel of the continuous spiral phase filter.

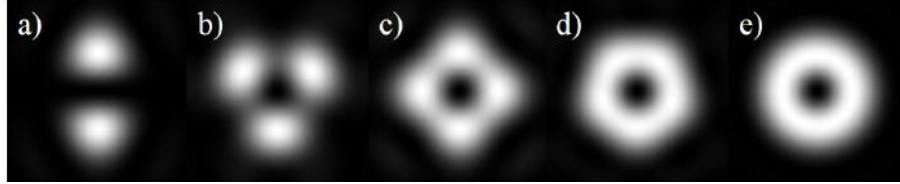


Figure 2.9. Point spread functions of the multi-step spiral phase filter. a)  $|h_2(x_i, y_i)|^2$ , b)  $|h_3(x_i, y_i)|^2$ , c)  $|h_4(x_i, y_i)|^2$ , d)  $|h_5(x_i, y_i)|^2$ , e)  $|h(x_i, y_i)|^2$ .

### 2.2.2.1 4 step phase vortex filter

A particular case of interest arise when the multi-step vortex filter has the number of steps  $p = 4$ . The phase configuration of the four discrete vortices that can be represented with  $p = 4$ , one for each orientation of the major vortex discontinuity can be represented as

$$\begin{aligned} \mathbf{\Psi}_4(u, v) &= \left[ \Psi_4^{(1)}(u, v), \Psi_4^{(2)}(u, v), \Psi_4^{(3)}(u, v), \Psi_4^{(4)}(u, v) \right]^T \\ &= \frac{\pi}{2} \mathbf{R} \mathbf{q}(u, v), \end{aligned} \quad (2.24)$$

where the symbol  $^T$  denotes transposition,

$$\mathbf{q}(u, v) = [H(u)H(v), H(-u)H(v), H(-u)H(-v), H(u)H(-v)]^T, \quad (2.25)$$



and

$$\begin{aligned}
 \mathbf{R} &= [r_{i,j}] \\
 &= [\mathbf{r}_1, \mathbf{r}_2, \mathbf{r}_3, \mathbf{r}_4]^T \\
 &= \begin{pmatrix} 0 & 1 & 2 & 3 \\ 3 & 0 & 1 & 2 \\ 2 & 3 & 0 & 1 \\ 1 & 2 & 3 & 0 \end{pmatrix}.
 \end{aligned} \tag{2.26}$$

Here  $\mathbf{q}(u, v)$  is the quadrant vector (a vector with functions as components), and to  $\mathbf{R}$  as the vortex rotation matrix.  $H(u)$  is the Heaviside step function:  $H(u) = 1$ , if  $u \geq 0$ , and zero otherwise.





Discontinuity orientation $\theta_n$	Phase of the $n$ th filter $\psi_n(u, v) = (\pi/2) \mathbf{r}_n \cdot \mathbf{q}(u, v)$	3D schematic phase filter
$\theta_1 = 0$ (West)	$\mathbf{r}_1 = (0, 1, 2, 3)$	
$\theta_2 = \frac{\pi}{2}$ (North)	$\mathbf{r}_2 = (3, 0, 1, 2)$	
$\theta_3 = \pi$ (East)	$\mathbf{r}_3 = (2, 3, 0, 1)$	
$\theta_4 = \frac{3}{2}\pi$ (South)	$\mathbf{r}_4 = (1, 2, 3, 0)$	

Figure 2.10. 4-Step vortex filter.

In Fig. 2.10, the first column shows the 4 filter orientations, or 4 filters, for that matter, specified by the orientation  $\theta_n$  of their largest phase dis-

continuity . For brevity, this orientation is designated as  $W$  for  $\theta_1 = 0$  ,  $N$  for  $\theta_2 = \pi/2$  ,  $E$  for  $\theta_3 = \pi$  , and  $S$  for  $\theta_4 = 3\pi/2$ , designation that were taken from the initials of the four cardinal points: West, North, East and South. In the second column are the phases of each quadrant of the four filters, written mod  $\pi/2$  , and in the third these phases are represented with grey levels and in relief, with the relief thickness proportional to the phase magnitude. Notice that the  $n$  filter is represented by the vector  $\mathbf{r}_n$ , the  $n$ th row of the matrix  $\mathbf{R}$ . It is worth to point out that, this kind of multi-level phase vortex has been already studied for various topological charges [71].

Thus, the phase filter can be expressed as

$$\begin{aligned} \mathbf{H}_4^{(n)}(u, v) &= \exp[i m \Psi_4^{(n)}(u, v)] \\ &= \exp \left[ i \frac{\pi}{2} \sum_{j=1}^4 r_{n,j} q_j(u, v) \right], \end{aligned} \quad (2.27)$$

and

$$r_{n,j} = r_{1,j} + n - 1 \pmod{4}, \quad (2.28)$$

given that

$$\sum_{j=1}^4 q_j(u, v) = H(u)H(v) + H(-u)H(v) + H(-u)H(-v) + H(u)H(-v) = 1 \quad (2.29)$$

the filter can be written as

$$\begin{aligned} \mathbf{H}_4^{(n)}(u, v) &= \exp[i \Psi_4^{(1)}(u, v)] \exp \left[ i(n-1) \frac{\pi}{2} \sum_{j=1}^4 q_j(u, v) \right] \\ &= \exp \left[ i(n-1) \frac{\pi}{2} \right] \mathbf{H}_4^{(1)}(u, v). \end{aligned} \quad (2.30)$$

It is deduced from Eq. (2.30) that: the rotation of the multi-step filter, as in the continuous vortex filter, can be written as a combination of the original filter  $\mathbf{H}_4^{(1)}(u, v)$  and a phase increment.

The principal difference is that for multi-step vortex the rotation factor depends of  $n$  as stated before, where  $n \in \mathbb{N}$ . Meaning that  $n$  is restricted to values such that  $n < p$ . For instance, for  $p = 4$ ,  $n$  can take the values of  $n = \{0, 1, 2, 3\}$  only. In counterpart for the continuous vortex phase filter, where the rotation can be done for any angle, because the rotation factor

$\alpha_n \in \mathbb{R}$ . This has an important repercussion in the rotation of the multi-step phase vortex filter. For example if  $p = 5$  the only phase increments that can be done would be  $n = \{0 \ 1 \ 2 \ 3 \ 4\}$ , representing a phase change of  $\{0 \ 2\pi/5 \ 4\pi/5 \ 6\pi/5 \ 8\pi/5\}$ , no other phase increment can be done exactly.

### 2.2.2.2 Point spread function of the 4-step vortex phase filter

As for the continuous vortex phase filter, the kernel  $h_4^{(1)}(x_i, y_i)$  should be calculated.

$$h_4^{(1)}(x_i, y_i) = - \iint_{\text{aperture}} \exp[i\Psi_4^{(1)}(u, v)] \exp\left[-i\frac{2\pi}{\lambda f}(ux_i + vy_i)\right] du dv. \quad (2.31)$$

from Eq. (2.27), Eq. (2.31) can be rewritten as:

$$\begin{aligned} h_4^{(1)}(x_i, y_i) = & - \iint_{\text{aperture}} \exp\left[i\left(0 \times H(u)H(v) + 1 \times H(-u)H(v) + \right. \right. \\ & \left. \left. + 2 \times H(-u)H(-v) + 3 \times H(u)H(-v)\right)\right] \times \\ & \exp\left[-i\frac{2\pi}{\lambda f}(ux_i + vy_i)\right] du dv. \end{aligned} \quad (2.32)$$

From Eq. (2.32) that the filter kernel, depends of the aperture symmetry. As stated in [24], usually the vortex filter are displayed in an SLM whose typical shape is shown in Fig. 2.11.

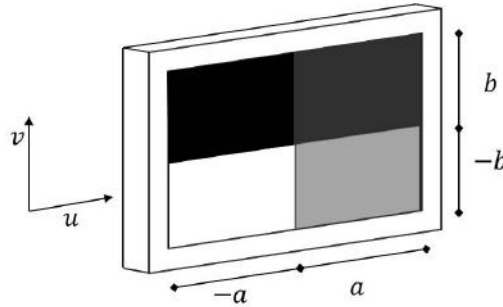


Figure 2.11. Spatial light modulator typical shape.

The limits of the aperture are:

$$\begin{aligned} -a &\leq u \leq a \\ -b &\leq v \leq b \end{aligned}$$

Using these limits, the integral of 2.32 can be evaluated. Thus an analytical form for the kernel can be calculated. As the continuous vortex kernel, the multi-step vortex kernel has its real and imaginary parts.

$$h_4^{(1)}(x_i, y_i) = \text{Re}\{h_4^{(1)}(x_i, y_i)\} + i\text{Im}\{h_4^{(1)}(x_i, y_i)\}, \quad (2.33)$$

where

$$\begin{aligned} \text{Re}\{h_4^{(1)}(x_i, y_i)\} = & \frac{\lambda f}{2\pi^2 x_i y_i} \left[ \sin\left(\frac{2\pi}{\lambda f}(y_i b - x_i a)\right) + \right. \\ & \left. + \sin\left(\frac{2\pi}{\lambda f}x_i a\right) - \sin\left(\frac{2\pi}{\lambda f}y_i b\right) \right], \end{aligned} \quad (2.34)$$

and

$$\begin{aligned} \text{Im}\{h_4^{(1)}(x_i, y_i)\} = & \frac{\lambda f}{2\pi^2 x_i y_i} \left[ -\sin\left(\frac{2\pi}{\lambda f}(y_i b + x_i a)\right) + \right. \\ & \left. + \sin\left(\frac{2\pi}{\lambda f}x_i a\right) + \sin\left(\frac{2\pi}{\lambda f}y_i b\right) \right], \end{aligned} \quad (2.35)$$

It is noticed from Eq. (2.34) that if the dimensions of the SLM are the same ( $a = b$ ) the real part vanishes through the axis.

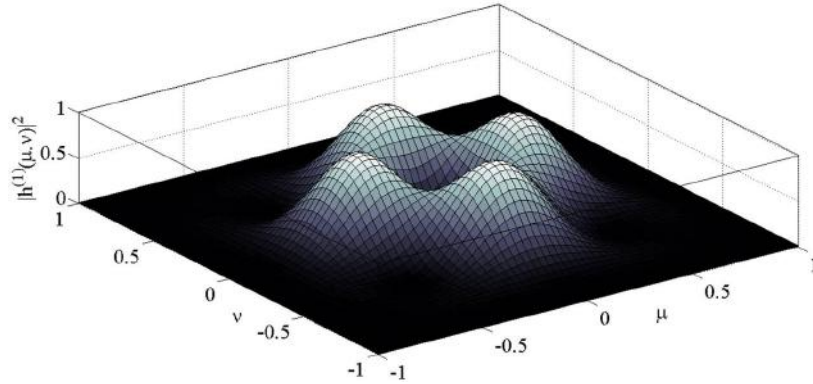


Figure 2.12. 4-Step vortex phase filter PSF  $|h_4^{(1)}(x_i, y_i)|^2$ .

Fig. 2.12 sketches the point spread function of the 4-step vortex phase filter. The PSF of the continuous vortex and the multi-step vortex with infinity number of steps are the same. Thus, it is expected that the result of filtering with the continuous or the multi-step vortex will produce similar results.

## 2.3 Vortex phase filter interference

On previous sections basic concepts of the vortex phase filtering and some variants are explained. Lets assume that a reference field  $U_r(x_i, y_i)$  is added to the image field  $U_i(x_i, y_i)$  of the  $4f$  system, as it is shown in Fig. 2.13. For simplicity, it is assumed that the reference beam is parallel, and incides normally to the image plane  $(x_i, y_i)$ . This means that  $U_r(x_i, y_i) = a_r \exp[i\phi_r]$ , where both phase and amplitude are constant.

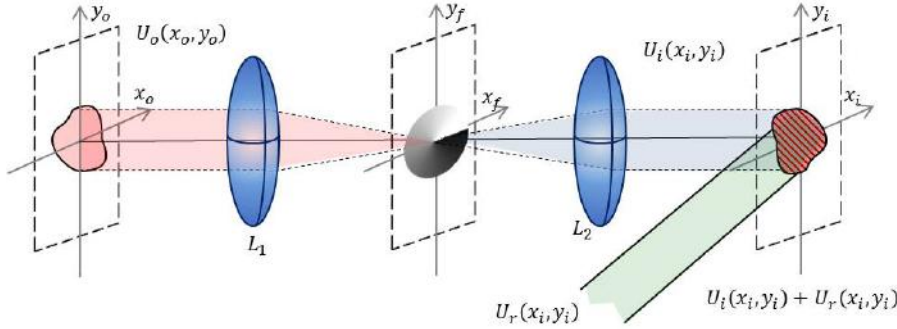


Figure 2.13. Vortex phase filter interference typical setup.

This wave interference is recorded in a camera. Hence, the intensity distribution  $I(x_i, y_i)$  detected by the camera can be expressed as:

$$\begin{aligned} I(x_i, y_i) &= |U_r(x_i, y_i) + U_i(x_i, y_i)|^2 \\ &= \left| U_r(x_i, y_i) + \mathcal{F}^{-1}\{\mathbf{H}(u, v)\mathbf{G}_f(u, v)\} \right|^2. \end{aligned} \quad (2.36)$$

Lets remember that  $\mathbf{G}_f(u, v) = \mathcal{F}\{P(x_o, y_o)U_o(x_o, y_o)\}$ , is the frequency spectrum of the object field bounded by the pupil function.

The interference pattern  $I(x_i, y_i)$  that is obtained in the camera depends mostly of the phase of the object wave field  $U_o(x_o, y_o)$ . This phase can be categorized in two main divisions:

- **weak phase objects:** objects whose phase is  $\ll 2\pi$
- **strong phase objects:** objects whose phase is  $\geq 2\pi$

It is not the same the analysis of a strong phase object such as a lens and a weak phase object such as in biology or thin film analysis. The difference is explained in the following subsections.

### 2.3.1 Weak phase objects

If the field  $U_o(x_o, y_o)$  has the particularity that

$$\max \varphi_o(x_o, y_o) = \max \angle U_o(x_o, y_o) \ll 2\pi,$$

and is propagated through the  $4f$  correlator; here the operator  $\angle$  stands for the argument of the function. The intensity distribution  $I(x_i, y_i)$ , of the reference field and the image field with no pupil restriction, can be expressed as

$$\begin{aligned} I(x_i, y_i) &= |a_r \exp[i\phi_r] + U_i(x_i, y_i)|^2 \\ &= \left| a_r \exp[i\phi_r] + \mathcal{F}^{-1}\{\mathbf{H}(u, v)\mathcal{F}\{U_o(x_o, y_o)\}\} \right|^2 \\ &= |a_r \exp[i\phi_r] + U_o(x_o, y_o) \otimes \mathbf{h}(x_i, y_i)|^2. \end{aligned} \quad (2.37)$$

From Eq. (2.12), and assuming that the reference beam is parallel, and incides normally to the image plane ( $U_r(x_i, y_i) = a_r$ ), the intensity distribution can be expressed as;

$$\begin{aligned} I(x_i, y_i) &= |a_r + \mathcal{H}\mathcal{R}\{U(x_o, y_o)\}|^2 \\ &= a_r^2 + |\mathcal{H}\mathcal{R}\{U(x_o, y_o)\}|^2 + \\ &\quad + a_r \mathcal{H}\mathcal{R}\{U(x_o, y_o)\} + a_r \mathcal{H}\mathcal{R}\{U^*(x_o, y_o)\}, \end{aligned} \quad (2.38)$$

Where  $*$  is the complex conjugate of the field.

If

$$\begin{aligned} \Theta(x_i, y_i) &= \angle \mathcal{H}\mathcal{R}\{U(x_o, y_o)\} \\ \mathcal{A}(x_i, y_i) &= |\mathcal{H}\mathcal{R}\{U(x_o, y_o)\}|, \end{aligned} \quad (2.39)$$

The intensity distribution can be rewritten from substituting Eq. (2.39) into Eq. (2.38).

$$I(x_i, y_i) = a_r^2 + \mathcal{A}^2(x_i, y_i) + 2a_r \mathcal{A}(x_i, y_i) \cos(\Theta(x_i, y_i)). \quad (2.40)$$

Defining

$$\begin{aligned} A(x_i, y_i) &= a_r^2 + \mathcal{A}^2(x_i, y_i) \\ B(x_i, y_i) &= 2a_r \mathcal{A}(x_i, y_i), \end{aligned} \quad (2.41)$$

The classical interference equation is obtained:

$$I(x_i, y_i) = A(x_i, y_i) + B(x_i, y_i) \cos(\Theta(x_i, y_i)) \quad (2.42)$$

If a rotation phase  $\exp[i\alpha_n]$  is induced to the vortex filter.

$$\begin{aligned} \mathcal{F}^{-1}\{\mathbf{H}^{(n)}(u, v)\mathcal{F}\{U_o(x_o, y_o)\}\} &= \mathcal{F}^{-1}\{\mathbf{H}(u, v) \exp[i\alpha_n]\mathcal{F}\{U_o(x_o, y_o)\}\} \\ &= \exp[i\alpha_n]\mathcal{F}^{-1}\{\mathbf{H}(u, v)\mathcal{F}\{U_o(x_o, y_o)\}\} \\ &= \exp[i\alpha_n]U_o(x_o, y_o) \otimes \mathbf{h}(x_i, y_i) \\ &= \exp[i\alpha_n]\mathcal{H}_{\mathcal{R}}\{U(x_o, y_o)\}. \end{aligned} \quad (2.43)$$

The intensity distribution for  $n$ - phase rotation of the vortex is

$$I^{(n)}(x_i, y_i) = A(x_i, y_i) + B(x_i, y_i) \cos(\Theta(x_i, y_i) + \alpha_n) \quad (2.44)$$

The result of this intensity distribution is a relief-like shadow images obtained from the filter process with the vortex. This relief gives an indication of the sample topology [23], which is useful for phase contrast microscopy, therefore this technique is frequently used for SCM.

Depending of the Spiral Phase Filter (SPF) orientation this shadow can be projected in any direction [72], this effect is shown for four orientations in Fig.2.14. It is deduced from Eq. (2.44) that the rotation of the vortex induces a piston term. The piston term acts different than in traditional interferometry, here the piston affects the shadow position rather than a fringe pattern.

The image on Fig.2.14 represents an amplitude-phase image. Where the letters "ABC" corresponds to a phase object and "XYZ" belongs to the amplitude object. It is worth to remark, that only the phase objects present substantial change in the illumination pattern; the relief is more prominent in the phase only elements rather than in the amplitude only elements.



Figure 2.14. Intensity distribution  $I^{(n)}(x_i, y_i)$  for a weak phase object. a)  $I^{(1)}(x_i, y_i)$ ,  $\alpha_1 = 0$ , b)  $I^{(2)}(x_i, y_i)$ ,  $\alpha_2 = \pi/2$ , c)  $I^{(3)}(x_i, y_i)$ ,  $\alpha_3 = \pi$ , d)  $I^{(4)}(x_i, y_i)$ ,  $\alpha_4 = 3\pi/2$ .

### 2.3.1.1 Phase extraction

As in traditional interferometry, the phase can be extracted from the series of interferograms recorded. For an 4 step phase extraction, a 4 phase rotation is implemented with  $\alpha_n = 0, \pi/2, \pi, 3\pi/2$ . The intensity distributions with those rotations can be written as;

$$\begin{aligned}
 I^{(1)}(x_i, y_i) &= A(x_i, y_i) + B(x_i, y_i) \cos(\Theta(x_i, y_i)) \\
 I^{(2)}(x_i, y_i) &= A(x_i, y_i) - B(x_i, y_i) \sin(\Theta(x_i, y_i)) \\
 I^{(3)}(x_i, y_i) &= A(x_i, y_i) - B(x_i, y_i) \cos(\Theta(x_i, y_i)) \\
 I^{(4)}(x_i, y_i) &= A(x_i, y_i) + B(x_i, y_i) \sin(\Theta(x_i, y_i)). \quad (2.45)
 \end{aligned}$$

From Eq. (2.45) the phase  $\Theta(x_i, y_i)$  can be extracted using the four intensity patterns of each step introduced by the rotation:

$$\Theta(x_i, y_i) = \arctan\left(\frac{I^{(2)}(x_i, y_i) - I^{(4)}(x_i, y_i)}{I^{(1)}(x_i, y_i) - I^{(3)}(x_i, y_i)}\right), \quad (2.46)$$

also the average intensity can be determined using

$$A(x_i, y_i) = \frac{1}{4} \left( I^{(1)}(x_i, y_i) + I^{(2)}(x_i, y_i) + I^{(3)}(x_i, y_i) + I^{(4)}(x_i, y_i) \right), \quad (2.47)$$

and the visibility term by

$$\begin{aligned}
 B(x_i, y_i) &= \frac{1}{4} \left| I^{(1)}(x_i, y_i) \exp[-i\alpha_1] + I^{(2)}(x_i, y_i) \exp[-i\alpha_2] + \right. \\
 &\quad \left. + I^{(3)}(x_i, y_i) \exp[-i\alpha_3] + I^{(4)}(x_i, y_i) \exp[-i\alpha_4] \right|, \quad (2.48)
 \end{aligned}$$



and the reference amplitude can be calculated by using:

$$a_r^2(x_i, y_i) = \frac{1}{2}A(x_i, y_i) \pm \sqrt{A^2(x_i, y_i) - B^2(x_i, y_i)}, \quad (2.49)$$

It is matter of concern that Eq. (2.49) has two possible solutions. When the positive sign is selected, most of the intensity is caused by the reference wavefront. This happens when the analyzed object is a thin phase object.

Finally the transformed field can be determined by

$$\mathcal{A}(x_i, y_i) = \sqrt{A(x_i, y_i) - a_r^2}, \quad (2.50)$$

The extracted amplitude  $\mathcal{A}(x_i, y_i)$  and the extracted phase  $\Theta(x_i, y_i)$  are shown in Fig.2.15. This components were calculated employing the 4-step interferograms form Fig.2.14, and using Eq. (2.46) and Eq. (2.50).

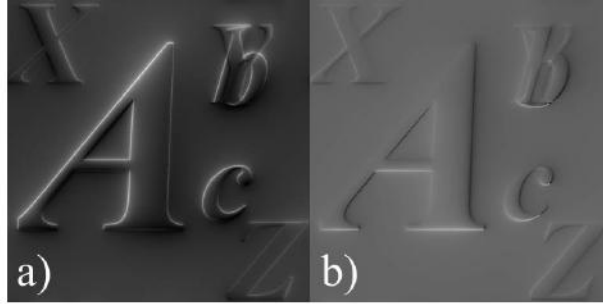


Figure 2.15. Extracted phase and amplitude from the interference patterns displayed on Fig.2.14. a) Amplitude  $\mathcal{A}(x_i, y_i)$ , b) phase  $\Theta(x_i, y_i)$

With Eq. (2.46) and Eq. (2.50), the transformed Radial Hilbert field can be recovered using the extracted amplitude and phase.

$$\mathcal{H}_{\mathcal{R}}\{U(x_o, y_o)\} = \mathcal{A}(x_i, y_i) \exp[i\Theta(x_i, y_i)],$$

Nevertheless, the RHT field is not the main aim for a quantitative analysis of the object field  $U_o(x_o, y_o)$  is sought. An operation of inverse Radial Hilbert Transform must be applied. This operation is the same as performing a deconvolution operation of the transformed field. Fortunately, the deconvolution process is quiet simple. Because the inverse filter required for this operation is the inverse vortex filter,

$$\mathbf{H}^{-1}(u, v) = \exp[-i\Psi(u, v)]. \quad (2.51)$$

The inverse spiral filter show an opposite direction of the phase increment through the angle, so it cancels the effect of the original vortex phase. Thus the extracted field can be obtained by:

$$U(x_e, y_e) = \mathcal{H}_{\mathcal{R}}\{U(x_o, y_o)\} \otimes \mathbf{h}^{-1}(x_i, y_i). \quad (2.52)$$

where  $(x_e, y_e)$  stands from extracted coordinates plane, that are related with the object plane by  $(x_e, y_e) = (-x_o, -y_o)$ , this sign inversion is caused by the configuration of the  $4f$  correlator.

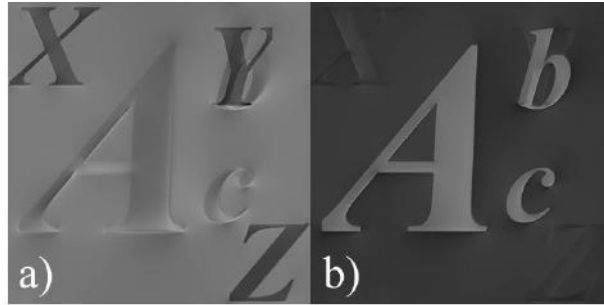


Figure 2.16. Denconvoluted phase and amplitude extraction from the interference patterns displayed on Fig.2.16. a) Amplitude  $a_o(x_e, y_e)$ , b) phase  $\varphi_o(x_e, y_e)$ .

The extracted phase after the deconvolution is shown in Fig. 2.16. In contrast with other phase extraction methods, it is important to stand out that the amplitude and the phase of the field can be independently extracted. Moreover, this attributes can be quantified and evaluated numerically. Making this the main difference between Zernike's microscopy technique and SPM.

### 2.3.2 Strong phase objects

If the field  $U_o(x_o, y_o)$  has the particularity that

$$\max \varphi_o(x_o, y_o) = \max \angle U_o(x_o, y_o) \geq 2\pi,$$

and is propagated through the  $4f$  correlator. The intensity distribution  $I(x_i, y_i)$ , of the reference field and the image field with no pupil restriction,

can be expressed just the same as for the weak phase, Eq. (2.38). A treatment similar to the weak phase extraction technique can be deduced with the same arguments. But, for this case is worth to explore the intensity distribution due the continuous spiral phase vortex and a multi-step phase vortex.

### 2.3.2.1 Continuous phase vortex

The intensity distribution  $I(x_i, y_i)$ , for continuous spiral phase filter can be seen in Fig. 2.17. The main characteristic of this interference pattern is an spiral carrier. This spiral carrier presents an advantage over traditional interferometry. It can be seen in Fig. 2.17 that the spiral direction varies. There are spirals whose direction is right handed and spirals whose direction is out left handed. This direction is a consequence of the extracted phase sign [73, 74].

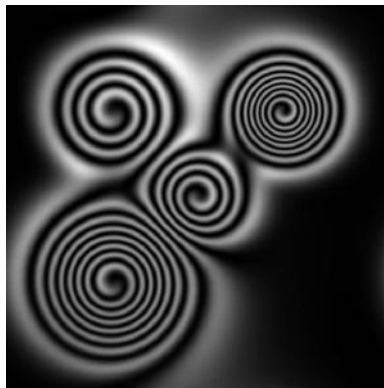


Figure 2.17. Intensity distribution  $I(x_i, y_i)$  with spiral carrier, for a continuous vortex phase filter.

The main difference between the strong phase objects and the weak phase object intensity distribution are the fringes with the spiral carrier.

### 2.3.2.2 Multi-step phase vortex

It was analysed in section 2.2.2.2 that the PSF of the multi-step spiral filter and the continuous one bear a similar resemblance. Even so, there are slight differences that are worth to pointed out. The intensity distribution can be

expressed as:

$$\begin{aligned}
 I_p(x_i, y_i) &= |a_r \exp[i\phi_r] + U_i(x_i, y_i)|^2 \\
 &= \left| a_r \exp[i\phi_r] + \mathcal{F}^{-1}\{\mathbf{H}_p(u, v)\mathcal{F}\{U_o(x_o, y_o)\}\} \right|^2 \\
 &= |a_r \exp[i\phi_r] + U_o(x_o, y_o) \otimes \mathbf{h}_p(x_i, y_i)|^2. \tag{2.53}
 \end{aligned}$$

In Eq. (2.53) the operation  $\mathcal{F}^{-1}\{\mathbf{H}_p(u, v)\mathcal{F}\{U_o(x_o, y_o)\}\}$  takes place. When the transfer function corresponded to the spiral phase filter, this operation was called RHT. Although the multi-step filter has a similar kernel, the same operation should be calculated each step. So, the Partial Radial Hilbert Transform PRHT is defined as:

$$\begin{aligned}
 \mathcal{H}_{\mathcal{R}_p}\{g(x_o, y_o)\} &= \mathcal{F}^{-1}\{\mathcal{F}\{g_o(x_o, y_o)\}\mathbf{H}_p(u, v)\} \\
 &= g_o(x_o, y_o) \otimes \mathbf{h}_p(x_o, y_o)
 \end{aligned}$$

Thus, Eq. (2.53) can be rewritten as

$$\begin{aligned}
 I_p(x_i, y_i) &= |a_r + \mathcal{H}_{\mathcal{R}_p}\{U(x_o, y_o)\}|^2 \\
 &= a_r^2 + |\mathcal{H}_{\mathcal{R}_p}\{U(x_o, y_o)\}|^2 + \\
 &\quad + a_r \mathcal{H}_{\mathcal{R}_p}\{U(x_o, y_o)\} + a_r \mathcal{H}_{\mathcal{R}_p}\{U^*(x_o, y_o)\}, \tag{2.54}
 \end{aligned}$$

If

$$\begin{aligned}
 \Theta_p(x_i, y_i) &= \angle \mathcal{H}_{\mathcal{R}_p}\{U(x_o, y_o)\} \\
 \mathcal{A}_p(x_i, y_i) &= |\mathcal{H}_{\mathcal{R}_p}\{U(x_o, y_o)\}|, \tag{2.55}
 \end{aligned}$$

The intensity distribution can be rewritten from substituting Eq. (2.55) into Eq. (2.54).

$$I_p(x_i, y_i) = a_r^2 + \mathcal{A}_p^2(x_i, y_i) + 2a_r \mathcal{A}_p(x_i, y_i) \cos(\Theta_p(x_i, y_i)). \tag{2.56}$$

Defining

$$\begin{aligned}
 A_p(x_i, y_i) &= a_r^2 + \mathcal{A}_p^2(x_i, y_i) \\
 B_p(x_i, y_i) &= 2a_r \mathcal{A}_p(x_i, y_i), \tag{2.57}
 \end{aligned}$$

The interference equation for the Multi-Step spiral filter is obtained:

$$I_p(x_i, y_i) = A_p(x_i, y_i) + B_p(x_i, y_i) \cos(\Theta_p(x_i, y_i)) \tag{2.58}$$

The intensity distribution  $I_4(x_i, y_i)$ , for a 4-Step spiral phase filter can be seen in Fig. 2.18. The multi-step spiral phase filtering produces similar patterns as the obtained due to the continuous vortex phase filter. Except that a diffraction pattern appears due the the multi-steps vortex filter. When more steps are added to the filter, the more it resembles the effect caused by the continuous vortex filter.

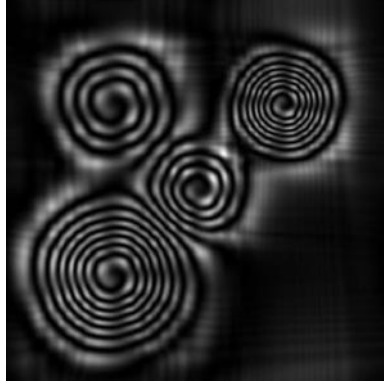


Figure 2.18. Intensity distribution  $I_4(x_i, y_i)$  with spiral carriers, caused by multi-step spiral phase filter.

### 2.3.2.3 Phase extraction through one interferogram

Another advantage of the spiral vortex filtering is that the phase can be recovered using a single interferogram. As the Hilbert transform, the radial Hilbert transform posses the property of generate a quadrature signal. In case of the vortex phase filtering a type of 2-D quadrature image is obtained [63]. An analytic function can be defined as [75]:

$$g(x, y) - i\hat{g}(x, y) = \exp[i\varphi(x, y)], \quad (2.59)$$

where the analytic function has a real part and its quadrature function. For the vortex filtered interference pattern, the real part is

$$\begin{aligned} g(x_i, y_i) &= I(x_i, y_i) - A(x_i, y_i) \\ &= B(x_i, y_i) \cos(\Theta) \end{aligned} \quad (2.60)$$

And the expected quadrature function is

$$\begin{aligned} \hat{g}(x, y) &= I(x_i, y_i) - A(x_i, y_i) \\ &= -B(x_i, y_i) \sin(\Theta). \end{aligned} \quad (2.61)$$

If the RHT operator is applied to the real part of the analytic function, an approximation can be obtained in order to produce a quadrature function Eq. (2.62). When the interference fringes are considered as straight.

$$\begin{aligned} \mathcal{F}^{-1}\{\mathcal{F}\{g(x_i, y_i)\}\mathcal{H}(u, v)\} &= \mathcal{H}_{\mathcal{R}}\{g(x_o, y_o)\} \\ &\cong i \exp[i\beta(x_i, y_i)]B(x_i, y_i) \sin(\Theta). \end{aligned} \quad (2.62)$$

Where  $\beta(x_i, y_i)$  is an orientation angle associated with each point as shown in Fig. 2.19.

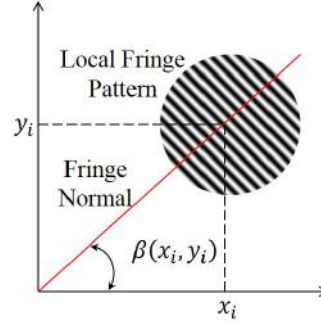


Figure 2.19. Local fringe orientation definition  $\beta(x_i, y_i)$ .

The orientation angle is related with the gradient of  $g(x, y)$ , as the direction of the gradient. Consequently the direction of a structure in a 2D domain is given by:

$$\beta_\pi(x_i, y_i) = \arctan \left( \frac{\partial g(x_i, y_i)}{\partial y_i} / \frac{\partial g(x_i, y_i)}{\partial x_i} \right). \quad (2.63)$$

The problem with this direction estimation is that is wrapped modulus  $\pi$ . There are algorithms that allow the unwrapping of this direction patterns [76]. But normalization techniques have to be applied [77]. There are different approaches that are used to calculate the orientation angle term [78, 79, 80]. The local fringe orientation extracted map  $\beta(x_i, y_i)$  is shown in Fig. 2.20.

Once the orientation map is extracted, the quadrature signal can be calculated.

$$\begin{aligned} \hat{g}(x_i, y_i) &= \text{Re}[\mathcal{V}\{g(x_i, y_i)\}] \\ &= \text{Re}[-i \exp[-i\beta(x_i, y_i)] \mathcal{H}_{\mathcal{R}}\{g(x_o, y_o)\}] \end{aligned} \quad (2.64)$$

Where  $\mathcal{V}\{(\ )\}$  is the Vortex operator. So, the convolved phase can be extracted using:

$$\Theta_w(x_e, y_e) = \arctan \left( \frac{\hat{g}(x_i, y_i)}{g(x_i, y_i)} \right). \quad (2.65)$$

The extracted phase  $\Theta_w(x_e, y_e)$  is the convolved phase of the object field, the subindex  $_w$  stands for wrapped phase. The deconvolution process is the

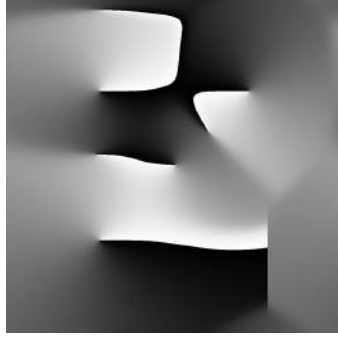


Figure 2.20. Local fringe orientation extracted map  $\beta(x_i, y_i)$  from the interference pattern  $I(x_i, y_i)$  from Fig. 2.17.

same as the process for weak phases, Eq. (2.52). The extraction of the phase with only one interferogram also works for intensity patterns obtained with a multi-step vortex filter.

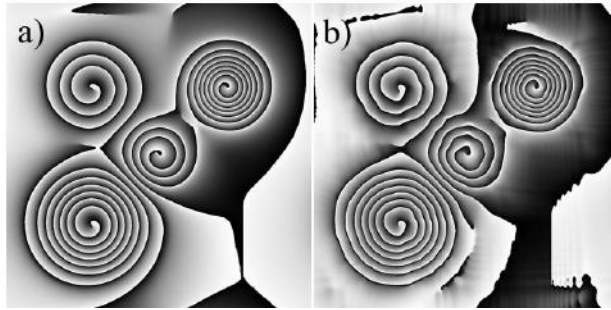


Figure 2.21. Extracted phase of the spiral interference pattern using one interferogram. a) Extracted convolved phase  $\Theta_w(x_e, y_e)$  from Fig.2.17, b) extracted convolved phase  $\Theta_4(x_e, y_e)$  from Fig.2.18

Fig. 2.22 shows the extracted phase using the interferograms from Fig. 2.17 and 2.18. It is shown that the convolved phase still has the spiral pattern and the sign ambiguity is lost even when the phase is convolved. When the deconvolution is done using Eq. (2.52), the phase has to be unwrapped, and many unwrapping algorithms have been developed for this purpose [81, 82, 83].

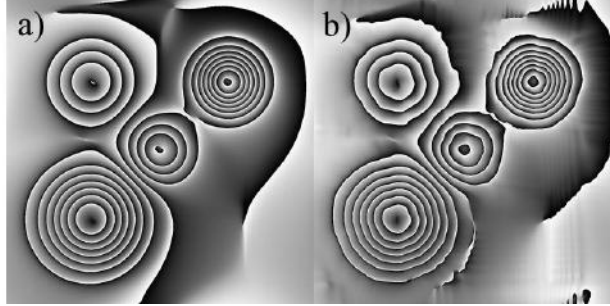


Figure 2.22. a) Deconvoluted phase  $\varphi(x_e, y_e)$  using phase map from Fig. 2.21a, b) deconvoluted phase  $\varphi(x_e, y_e)$  using phase map of 2.21b.

## 2.4 Phase extraction using vortex rotation

To obtain the interference pattern in the image plane, let's assume a reference wavefront  $U_r(x_i, y_i)$  to the filtered wavefront  $U_i(x_i, y_i)$ . For simplicity, it is further assumed that this reference beam is parallel, and incides normally to the camera, with a constant amplitude  $a_r$ , then  $U_r(x_i, y_i) = a_r$ . Therefore the recorded interference distribution is

$$\begin{aligned} I_p^{(n)}(x_i, y_i) &= \left| U_r(x_i, y_i) + U_{i_p}^{(n)}(x_i, y_i) \right|^2 \\ &= \left| a_r + \mathcal{F}^{-1} \left\{ \mathbb{H}_p^{(n)}(u, v) G_f(u, v) \right\} \right|^2. \end{aligned} \quad (2.66)$$

The subindex  $p$  also appears in the intensity distribution  $I(x_i, y_i)$ , this means that the number of steps affect the interferogram detected by the camera. Eq. (2.66) can be rewritten using Eq. (2.20).

$$\begin{aligned} I_p^{(n)}(x_i, y_i) &= \left| a_r + \exp \left[ i \left( \frac{2\pi(n-1)}{p} \right) \right] \right. \\ &\quad \times \left. \mathcal{F}^{-1} \left\{ \mathbb{H}_p^{(1)}(u, v) G_f(u, v) \right\} \right|^2 \\ &= \left| a_r + \exp \left[ i \left( \frac{2\pi(n-1)}{p} \right) \right] U_{i_p}^{(1)}(x_i, y_i) \right|^2 \end{aligned} \quad (2.67)$$

Developing the expression we can find

$$\begin{aligned} I_p^{(n)}(x_i, y_i) &= \mathcal{A}_p(x_i, y_i) \\ &\quad + \mathcal{B}_p(x_i, y_i) \cos \left[ \Theta_p(x_i, y_i) + \frac{2\pi(n-1)}{p} \right] \end{aligned} \quad (2.68)$$



where

$$\begin{aligned}\mathcal{A}_p(x_i, y_i) &= a_r^2 + \left| U_{i_p}^{(1)}(x_i, y_i) \right|^2, \\ \mathcal{B}_p(x_i, y_i) &= 2a_r \left| U_{i_p}^{(1)}(x_i, y_i) \right|^2, \\ \Theta_p(x_i, y_i) &= \arg \left[ U_{i_p}^{(1)}(x_i, y_i) \right].\end{aligned}\quad (2.69)$$

Eq. (2.68) is the classic interference equation, where the rotation of the MSSPF is all but a piston term in the interferogram. As the rotation of the filter can be done only in equispaced increments (unlike continuous spiral phase plate), the analytic signal of the  $n$ -interferograms, for  $p \geq 3$  can be calculated using [84],

$$U_{i_p}^{(1)}(x_i, y_i) = \sum_{n=1}^p I_p^{(n)}(x_i, y_i) \exp \left[ i \frac{2\pi(n-1)}{p} \right] \quad (2.70)$$

The extracted parameters are convolved with the MSSPF kernel. Therefore, a deconvolution process is applied.

$$U_o(x_i, y_i) = U_{i_p}^{(1)}(x_i, y_i) \otimes h_p^{-1}(x_i, y_i). \quad (2.71)$$

The symbol  $\otimes$  stands for the convolution operation and  $h^{-1}(x_i, y_i)$  is the inverse of the kernel of the MSSPF.

The phase increments introduced by the object displacement at the image fields are approximately equal at conjugate points  $(x_i, y_i) = (Mx_o, My_o)$ , where  $M$  is the magnification of the system, and is equal to  $-1$  in the case of a  $4f$  correlator. Therefore the phase increment that we sought is given by

$$\varphi_o^{(e)}(x_o, y_o) \simeq \arg [U_o(-x_i, -y_i)], \quad (2.72)$$

where the superscript  $e$  stands for extracted.

## 2.5 Numerical simulation

To verify the phase extraction equations, a numerical simulation of a Mach-Zehnder interferometer in a MSSPF configuration was devised. Depending on the magnitude of the phase introduced by the objects under analysis by the proposed technique, two different scenarios can be anticipated for the

kind of interferograms obtained with the proposed technique: first, when the object phases have values  $\geq 2\pi$  producing fringes that do not exceed the Nyquist sampling limit, in this case a typical interferogram depicts spiral fringe patterns for smooth phase changes. On the other hand, when the object phases are weak e.g. as occur in Zernike phase contrast microscopy, only an edge enhancement effect can be observed instead of fringe patterns. The numerical simulations of these two scenarios are presented next, to show that phase extraction with the proposed method is effective for weak and non-weak phase magnitudes.

### 2.5.1 Spiral fringe patterns

In order to make the numerical simulation preliminary values for the amplitude  $E_o(x_o, y_o)$  and phase  $\varphi_o(x_o, y_o)$  of the object field were defined, where the maximum value of the phase corresponded to  $6\pi$ . The field  $U_{i_p}^{(n)}(x_i, y_i)$  at the image plane of the  $4f$  correlator (Fig. 2.13) was obtained after two numerical Fourier transformations, indicated using  $p = 4$ . After computing this field, the intensity resulting from the superposition of  $U_{i_p}^{(n)}(x_i, y_i)$  and a plane wave of constant amplitude  $a_r$  and zero phase is found. As a result of this numerical simulation, the intensity distribution  $I_4^{(n)}(x_i, y_i)$  in Fig. 2.23 shows the result of this operation. It can be seen that a spiral carrier is obtained as for the continuous spiral phase plate. Unlike continuous spiral phase plate, an extra diffraction pattern caused by the incomplete doughnut kernel of the continuous spiral phase plate can be noticed. Using Eq.

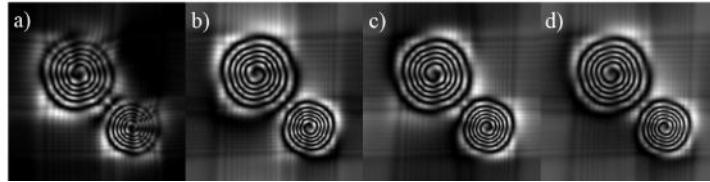


Figure 2.23. Computed interference pattern for  $p = 4$ . a)  $I_4^{(1)}(x_i, y_i)$ , b)  $I_4^{(2)}(x_i, y_i)$ , c)  $I_4^{(3)}(x_i, y_i)$ , d)  $I_4^{(4)}(x_i, y_i)$  of a double element phase object.

(2.70) and (2.71) the convolved and deconvolved phase are extracted using the interference patterns shown in Fig. 2.23.

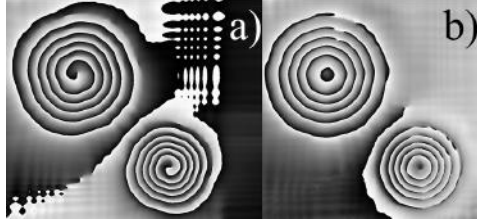


Figure 2.24. Extracted wrapped phase using the interferograms of Fig. 2.23. a) Convolved phase  $\Theta_4(x_i, y_i)$ , b) deconvolved phase  $\varphi_o^e(x_o, y_o)$ .

### 2.5.2 Phase contrast patterns

In order to illustrate the effect of this method when a weak phase object ( $\ll \pi$ ) is observed, numerical simulation was carried out. We have then defined the preliminary values for the amplitude  $E_o(x_o, y_o)$  and phase  $\varphi_o(x_o, y_o)$  of the object field, where the maximum value of the phase corresponded to  $0.1\pi$ . For this simulation, an USAF optical test pattern was used as the phase object  $\varphi_o(x_o, y_o)$ . As for the strong phase object simulation the field  $U_{i_p}^{(n)}(x_i, y_i)$  at the image plane of the  $4f$  correlator (Fig. 2.13) was obtained after two numerical Fourier transformations, indicated in Eq. (2.66) using  $p = 4$ . After computing this field, the intensity resulting from the superposition of  $U_{i_p}^{(n)}(x_i, y_i)$  and a plane wave of constant amplitude  $a_r$  and zero phase is found. As a result of this numerical simulation, the intensity distributions  $I_4^{(n)}(x_i, y_i)$  were calculated, this interferograms can be seen in Fig. 2.25.

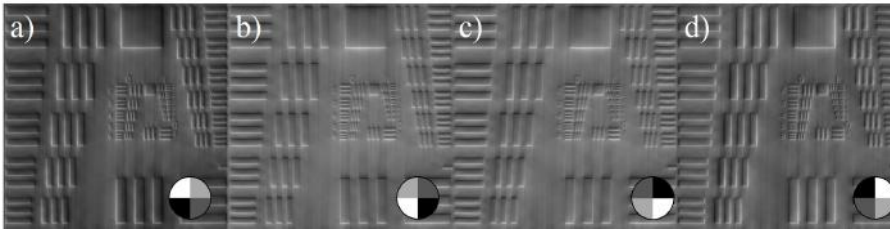


Figure 2.25. Computed interference pattern for  $p = 4$ , a)  $I_4^{(1)}(x_i, y_i)$ , b)  $I_4^{(2)}(x_i, y_i)$ , c)  $I_4^{(3)}(x_i, y_i)$ , d)  $I_4^{(4)}(x_i, y_i)$  of an only phase USAF optical test pattern.

It can be seen that there is no spiral carrier in the interferograms, but an

edge enhancement of the object is obtained. This effect is the same as the one obtained using the continuous spiral plate [23]. So this technique can be applied in spiral phase contrast microscopy, allowing the implementation of the MSSPF in a quantitative phase contrast microscopy. The phase can be extracted implementing Eqs. (2.70) and (2.71) using the interference patterns shown in Fig. 2.25. The extracted phase is displayed in Fig 2.26

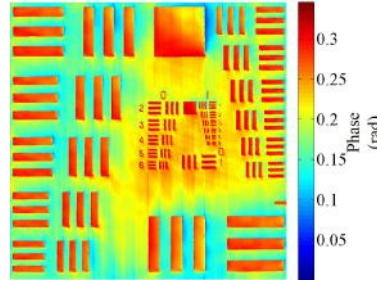


Figure 2.26. Extracted phase using the interferograms of Fig. 2.25.

### 2.5.3 Effect of incrementing the number of steps in the extracted phase

To test the reliability of this method, we made use of the Universal Quality Image Index  $Q$ , which provides a measure of the similitude of two gray level images [85]. It is given by the expression

$$Q = \frac{\sigma_{xy}}{\sigma_x \sigma_y} \frac{2\bar{x}\bar{y}}{\bar{x}^2 + \bar{y}^2} \frac{2\sigma_x \sigma_y}{\sigma_x^2 + \sigma_y^2} \quad (2.73)$$

where  $\bar{x}$  and  $\bar{y}$  are the average of  $N$ th dimensional vectors  $\mathbf{x}$  and  $\mathbf{y}$  and  $\sigma_x^2$ ,  $\sigma_y^2$ , and  $\sigma_{xy}$  are the co-variances of these vectors. The range of  $Q$  is  $[-1, 1]$ , then if  $Q = 1$ , the images are exactly the same. The  $Q$  index is used to compare the extracted phase and the original simulated phase. The extracted analyzed phase was unwrapped by following [86] as shown in Fig. 2.27a, and then  $Q$  was calculated using Eq. (2.73). To illustrate the error generated by the extracted phase, an absolute error map is shown in Fig. 2.27b. Nevertheless to make an accurate comparison  $Q$  was used obtaining the results that can be seen in Table 2.1

It can be seen that the three step method is a good approximation for the phase, this algorithm can be used to estimate the phase from objects whose

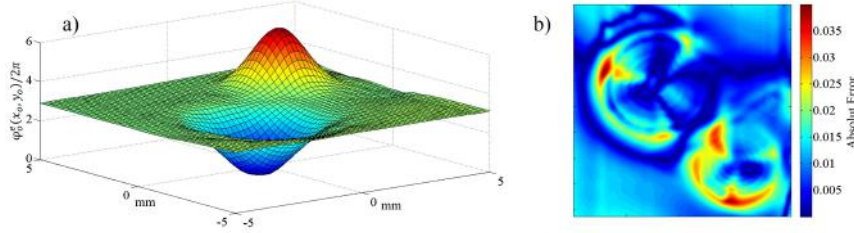


Figure 2.27. a) Unwrapped extracted phase, b) absolute error map, between the unwrapped extracted phase and the simulated phase

Table 2.1. Dependence of the quality index and the number of steps of the MSSPF

$p$	$Q$
3	0.884
4	0.905
5	0.912
6	0.912
7	0.913
8	0.914
10	0.914
20	0.915

phase change quickly letting no further interferograms to be obtained. From the results shown in table 2.1, it is observed that the quality index of the extracted phase depends on the number of steps  $p$  of the MSSPF; the phase quality rises as the number of steps grow. Nevertheless, a residual error is presented in the extracted phase despite the addition of more steps to the method. From Fig. 2.27b, it can be seen that the largest error (up to 4%) is presented in the borders of the phase. This steady error is also presented in the extraction of continuous spiral fringe demodulation techniques [63, 74].

## 2.6 Experimental results

Fig.2.28 shows the experimental setup for the phase extraction of a phase object using the MSSPF. The light from a He-Ne Laser  $L$  ( $\lambda = 632.8$  nm) is expanded using a microscope objective  $MO$  and collimated by the lens  $L_0$ .

The light is divided by a beam splitter  $BS_1$  into a reference beam (described with a dashed line) and the object beam (presented with a dotted line). The phase object  $Ob$  is a biconvex lens of 6 mm diameter. The examined area is  $10 \times 12$  mm. The object is placed at the back focal plane of the lens  $L_1$ , with 400 mm focal length and 35 mm diameter. The LCoS model LC-R 2500 by Holoeye <sup>TM</sup>, is placed at the back focal plane of  $L_2$ , both  $L_1$  and  $L_2$  are identical. The light reflected by the LCoS is collected by the lens  $L_2$  which incides directly to the CCD. The reference beam, generated by the beam splitter  $BS_1$ , and directed to the beam splitter  $BS_3$  by mirror  $M_1$ . Finally the interference pattern is recorder by the CCD.

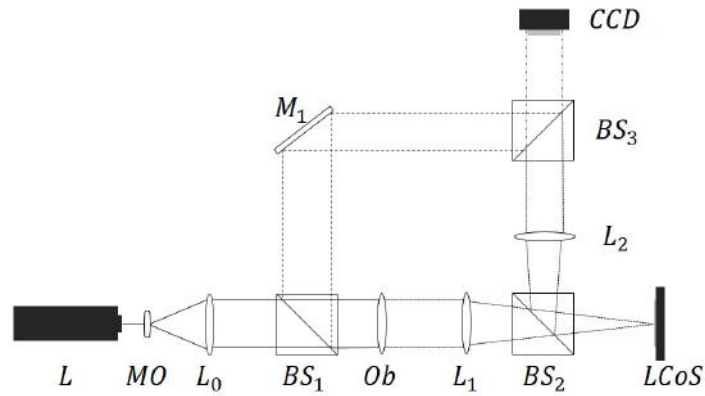


Figure 2.28. Schematic diagram of the experimental setup. A detailed description of the elements and their function is given in the text.

The LCoS has to be calibrated to get the correct polarization and for the given laser frequency to display the correct steps, otherwise the spiral carrier is not presented. From previous work, [87, 88] it is shown that this model of LCoS has not a dynamic range of  $2\pi$  for this particular setup; so the number of steps of the MSSPF are restricted. It is important to remark that a continuous spiral phase plate can not be displayed for this SLM for this particular polarization and wavelength. Fig 2.29 shows the experimental interference pattern  $I_p^{(n)}(x_i, y_i)$  obtained with the experimental setup of Fig. 2.28. There were used three different filters to prove the effectiveness of the technique  $p = 3, 4, 5$ . The obtained interferograms are presented in Fig 2.29, where it can be seen that the spiral carrier is preserved and a slightly diffraction pattern is shown in the interferograms.

Using the captured sequence  $I_4^{(1)}(x_i, y_i)$ ,  $I_4^{(2)}(x_i, y_i)$ ,  $I_4^{(3)}(x_i, y_i)$  and,  $I_4^{(4)}(x_i, y_i)$ ,

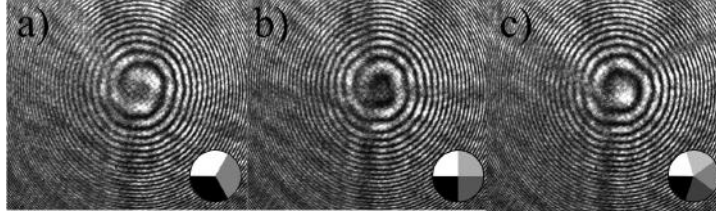


Figure 2.29. Experimental interference pattern  $I_p^{(n)}(x_i, y_i)$  with the MSSPF gray representation in the right corner. a)  $I_3^{(1)}(x_i, y_i)$ , b)  $I_4^{(1)}(x_i, y_i)$ , c)  $I_5^{(1)}(x_i, y_i)$ .

and using Eq. (2.70) the convolved wrapped phase can be extracted; the result is shown in Fig. 2.30a. As in the numerical simulation, the deconvolution of the phase has to be accomplished, the computed wrapped phase can be seen in Fig. 2.30b. The performance of the technique was

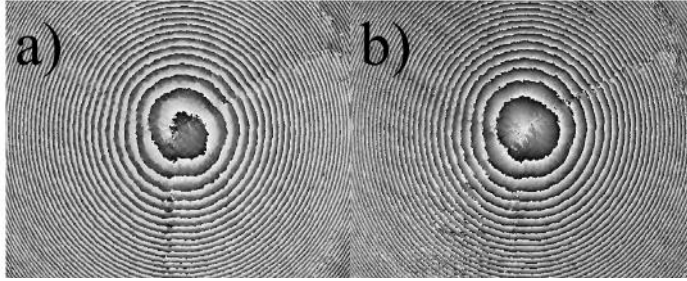


Figure 2.30. Experimental extracted wrapped phase. a) Convolved phase  $\Theta_4(x_i, y_i)$ , b) deconvolved phase  $\varphi_o^e(x_o, y_o)$ .

compared with a Wyco<sup>TM</sup> interferometer, the quality index for the experimental results confirms what theory predicted. For 3 steps,  $Q = 0.847$ , but there is an increment of quality index if the filter is changed into a four steps MSSPF,  $Q = 0.898$ . The best performance is achieved using five steps, where  $Q = 0.902$ . It is worth to emphasise that for this particular SLM, continuous spiral vortex can not be displayed, because the restricted dynamic range of the SLM. Nonetheless, MSSPF with  $p = 3, 4, 5$  can be displayed with no further problem.

## 2.7 Point diffraction interferometer with spiral carrier

The point diffraction interferometer known by its acronym PDI, is a common path interferometer invented in 1972 by Smartt [89]. Which is used for direct measurement of the optical path difference. The PDI is used for measuring different devices such as lenses [90], mirrors used in telescopes and even microscope objectives [91]. This type of interferometer is usually manufactured for individual wavelengths, from the infrared [92] to the ultraviolet [93]; therefore increasing with this their applications in the field of optical metrology. On this section the consequences of combining a multi-step vortex filter in a PDI are analyzed.

The point diffraction interferometer is also known as Smartt interferometer. It consists of a positive lens which is used to perform a Fourier transform of the transmitted or reflected light of an object placed at the focal distance of the lens, wherein a semitransparent plate (amplitude filter) attenuates the high frequencies of the transformed light field. This amplitude filter has a small hole, in the center, where the light amplitude is not attenuated, as seen on Fig. 2.31, referred as Smartt filter. The size of the amplitude orifice plate is usually chosen as approximately half the Airy disk; while the transmittance of the plate is chosen as approximately 0.01%. Diffraction caused by the small aperture on the amplitude filter generates a spherical wave front, this spherical wave front interferes with the wave front associated with the high frequencies of the system which are transmitted through the semitransparent plate section. The light that interferes after passing through the filter, is collected by a second lens, and an interference pattern is formed on a detector as shown in Fig. 2.31.

Several modifications of the PDI have been suggested: the central hole of the Smartt filter has been replaced by several smaller holes [94], the placement of the Smartt filter has been placed out of the  $L_1$  focus and called Hole Diffraction Interferometer (HDI) [90]. Also a variety of techniques have been suggested to extract the phase corresponding to the object. The addition of a phase step to the reference beam, which is generated by the diffraction spot, it is usually required in order to achieve phase measurement. Different phase shifting techniques have been proposed, such as the implementation of liquid crystals devices on the amplitude hole [95] or incorporating a beam splitter to make this shift [96].



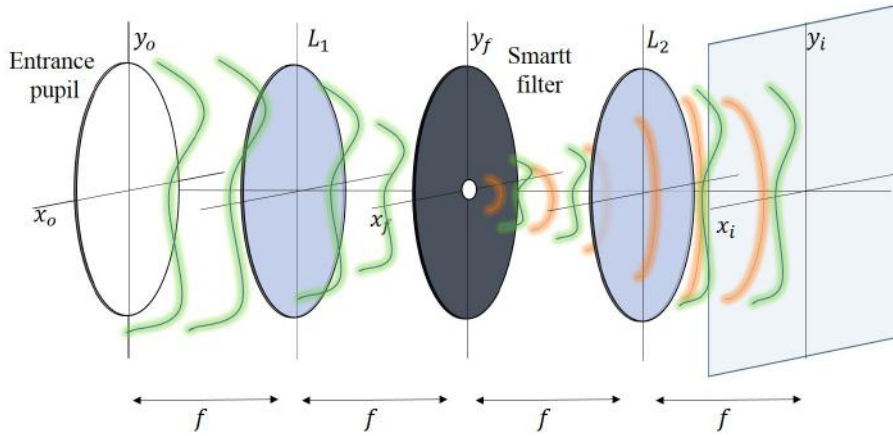


Figure 2.31. Schematic diagram of a point diffraction interferometer. The entrance pupil emits light transmitted or reflected by an object. Lens  $L_1$  collects the light shown in green color that is focused on a pinhole and its neighborhood. The transmitted and diffracted light, shown in green and red, after the Smartt filter are collected by lens  $L_2$  to form an interference pattern on plane  $(x_i, y_i)$  where a camera detector is usually positioned.

The main problem of the conventional PDI, is that the recorded interferogram has sign ambiguity and is not easy to implement phase shifting for phase extraction. One solution to this problem is to make the convolution of the input wavefront with the point spread function of a vortex filter. If this point spread function is used, the sign ambiguity is removed due to the orientation of the spiral, which gives information about the sign. Another advantage of the spiral interferograms is the extraction of phase from a single interferogram [97]. So in this section it relates the use of a hybrid phase filter with multi-step vortex phase is proposed. Here it is referred to this interferometer as point diffraction interferometer with discrete spiral (PDI-D). Unlike previous inventions proposed interferometer uses a discrete vortex combined with PDI. Also this hybrid filter can be rotated to introduce phase shifts in the point spread function of the interferometer.

The combined filter is a Smartt filter stacked with a discrete vortex. This filter can be seen on Fig. 2.32

This complex filter, can be described by

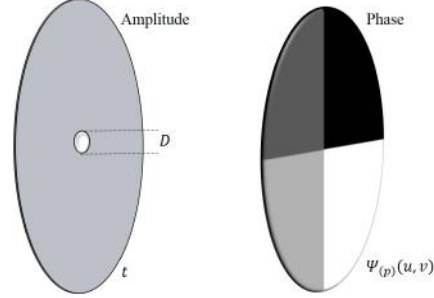


Figure 2.32. Combined filter: Smartt and discrete phase vortex of four steps are placed in a stack. Each gray level in the phase vortex represent a constant phase of  $0, \pi/2, \pi$  and  $3\pi/2$ .

$$H_{(p)}(u, v) = \text{circ}\left(\sqrt{u^2 + v^2}/D\right) \quad (2.74)$$

$$+t \left[1 - \text{circ}\left(\sqrt{u^2 + v^2}/D\right)\right] \exp\left(i\Psi_{(p)}(u, v)\right) \quad (2.75)$$

Where  $t$  corresponds to the transmittance of the filter which scale the amplitude of the discrete vortex,  $(u, v)$  are the coordinates in the complex spatial frequency domain,  $D$  is the orifice diameter filter and  $\Psi_{(p)}(u, v)$  corresponds to the phase of multi-step vortex.

The purposed filter is placed at a  $L_1$  focal length, the pinhole of the filter generates a spherical wave front, which interferes with the wavefront that has been modified by combined amplitude and a phase filter. After the filter the wavefront interference is created, a second lens  $L_2$ , located at a focal length of the filter is used to produce the interference of an uniform beam with the original wavefront. This collecting system is responsible for focusing the wavefront disturbed by the filter such as an image of the object placed on the input aperture is imaged at the camera detector plane.

The interferogram at the detector  $I(x_i, y_i)$ , can be modeled using the complex amplitude of the light reflected or transmitted from  $U(x_o, y_o)$  using

$$I(x_i, y_i) = \left| \mathcal{F}^{-1} \left\{ \mathcal{F} \{U_{in}(x_o, y_o)\} \times H_{(p)}(u, v) \right\} \right|^2, \quad (2.76)$$

Where  $\mathcal{F}$  and  $\mathcal{F}^{-1}$  are the Fourier transform operator and inverse fourier

transform operator respectively. The phase  $\Psi_{(p)}(u, v)$  of the complex filter  $H(u, v)$  as shown in Fig. 2.33 corresponds to the multi-step vortex with  $p = 4$ . The discrete phase introduced by the spiral filter transforms the standard Smartt amplitude filter into the combined (amplitude and phase) filter, being this component the main difference between the previously known techniques. It is recommended to use a filter transmittance between 0.01% and 0.12% depending on the application. While the diameter of the filter can be found from the following relation.

$$D < 1.22\lambda f_{\#} \quad (2.77)$$

Where  $\lambda$  is wavelength of the light being propagated through the system and  $f_{\#}$ , is called the f-number.

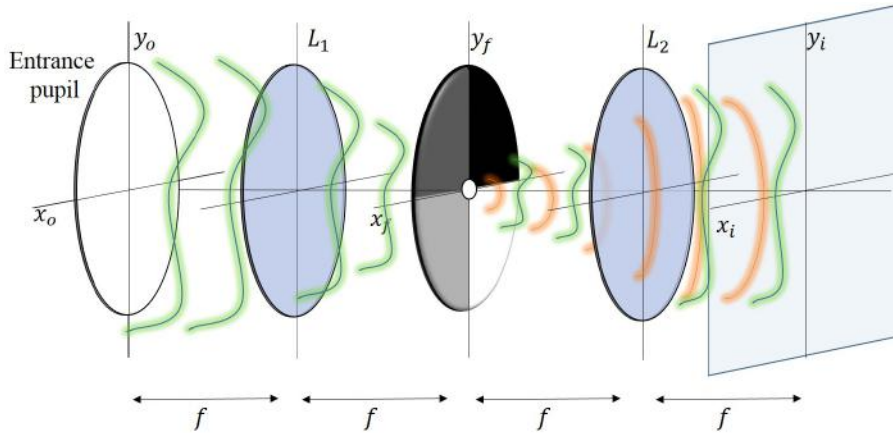


Figure 2.33. Optical setup of a point diffraction interferometer with the proposed combined filter.

Phase filters are vortices of topological charge one (this implies that the phase of the filter ranges from 0 to  $2\pi$ ). However, vortices may be quantized in steps as explained in previous sections. It has been shown that the multi-step vortex can be described by

$$\psi_{(p)}(u, v) = \frac{2\pi}{p} \left\lfloor \frac{\tan^{-1}(u/v) + \pi}{2\pi} p \right\rfloor, \quad (2.78)$$

Where the symbol  $\lfloor \cdot \rfloor$  is the floor operation, while the term  $\tan^{-1}(u/v)$  must be limited by  $-\pi \leq \tan^{-1}(u/v) \leq \pi$ .

### 2.7.1 Phase extraction

For the extraction phase of the wavefront to be analyzed, it can be used the method of recovering the phase just for one interferogram. However, it is also possible to extract the phase of the object by rotating the combined phase-amplitude filter. Upon rotating the filter, a factor  $R_p^{(n)}(u, v) = \exp\left[i\frac{2\pi(n-1)}{p}\right]$ , this means that a  $n$ -esim filter is generated, one for each rotation of the initial filter

$$H_{(p)}^{(n)}(u, v) = H_{(p)}(u, v) R^{(n)}(u, v). \quad (2.79)$$

Wherein each  $n$  rotation contributes to a piston-type factor in the interferogram,  $n$  is an integer which varies depending on the number of steps to be obtained, for example, if four steps are required  $n = 1, 2, 3, 4$ . Each value of  $n$  corresponds to a rotation of the filter. Therefore Eq. (2.76) can be rewritten as follows

$$I^{(n)}(x_i, y_i) = \left| \mathcal{F}^{-1} \left\{ \mathcal{F} \{U_{in}(x_o, y_o)\} \times H_{(p)}^{(n)}(u, v) \right\} \right|^2. \quad (2.80)$$

as explained in section 2.3.2, the obtained interferograms have an spiral fringe carrier, as shown on Fig. 2.17.

The interferograms present the same characteristics as the ones before, so the extraction of the phase can be done using Eq. (2.70). As well as before, deconvolution operation has to be done in order to extract the object phase.

## 2.8 Conclusions

In this chapter the characteristics of the vortex filter as well as the characteristics in interference were analyzed. It was shown that the spiral phase filter has different characteristics. For instance, when the continuous spiral filter is applied to an object it works as a Radial Hilbert Transform, which is the same as Riesz transform but with a complex kernel. Also, the topological charge of the spiral phase filter can be used to make emphasis in phase objects, making a fractional radial Hilbert transform. Likewise, the filter can be rotated; the rotation can be done without restrictions. Moreover, a spatial carrier can be added to the vortex phase to modulate the vortex kernel in the  $\pm 1$  diffraction orders.

Furthermore, the concept of Multi-Step phase filter is introduced. This Multi-Step filter is a discretized version of the spiral phase filter. In contrast the spiral phase, the multi-step phase filter can be rotated only using integer of the steps, and no intermediated values are accepted. This filter has a similar point spread function as the continuous vortex, therefore similar results are expected when it is applied.

The effect of phase-amplitude objects being filtered and then interfered with a reference beam are examined, where the effects of interference vary depending on the phase magnitude of the object. If the phase of the object is weak the interference pattern resembles a shadow relief of the phase object. In contrast, the interference pattern for strong phase objects presents spiral carrier.

When the phase extraction method for weak phase objects is performed using the rotation of the phase vortex to get a  $n$ -number of interferograms, the extracted amplitude and phase have to be deconvolved using the inverse spiral phase filter. This method is well known to be used for phase contrast microscopy, being the principle for spiral phase microscopy.

For the strong phase objects, there are two methods that can be applied to extract the phase of the object. The first one is based on the quadrature analytic signal concept. Where, just one interfereogram is used to extract the phase. The inconvenience is that different computational methods have to be applied in order to get all the parameters required. The second method is based on the rotation of the filter. The rotation induces a piston term to the interferogram, this allows using the traditional phase-stepping recovering phase algorithms. For both techniques the phase has to be deconvolved.

In conclusion, we presented an alternative method for phase extraction from interferograms obtained with multi-step spiral phase filter (MSSPF) that can be seen as a quantitative method of phase contrast microscopy. The phase extraction is based on the rotation of the MSSPF, which can be easily achieved with a spatial light modulator (SLM). This method has some advantages over traditional single-shot spiral interferometry. First of all, this technique can be implemented in phase extraction of weak phase objects, where no spiral carrier is presented, leading to a quantitative phase contrast method. Unlike the continuous spiral phase filter the MSSPF dynamic range depends directly on the number of steps of the filter, therefore the MSSPF can be displayed in an SLM with dynamic range smaller than  $2\pi$ . Nonetheless the reduced phase modulation, spiral fringe are still obtained in the interferograms which can be used with the proposed phase extraction method. The calibration of SLM is easier as it only consists of fixing a reduced number of phase steps, avoiding detuning of a large set of steps required for a continuous vortex generation. Compared to PZT transducers, there is no hysteresis. Not only twisted nematic nor parallel aligned SLM can be used but also binary SLM, due to the intrinsic discontinuity of the MSSPF. An additional advantage of the proposed method is that most of the reported techniques use the first diffraction order to introduce the vortex, however this method introduces the vortex in the zero order with increased light efficiency. It is also shown that the proposed method gives a phase reconstruction with residual noise depending on the number of steps, with similar remanent noise for steps greater than or equal to four.

## CHAPTER 3

# SCATTERED LIGHT FILTERING USING OPTICAL VORTICES

### Contents

---

<b>3.1</b>	<b>Introduction</b>	<b>72</b>
3.1.1	Speckle pattern properties	73
3.1.2	Out-of-plane measurement	76
3.1.3	In-plane measurement	79
3.1.4	Speckle shearing interferometer	81
<b>3.2</b>	<b>Displacement measurement with multi-level spiral phase plate in out-of-plane speckle interferometry</b>	<b>82</b>
3.2.1	Introduction	83
3.2.2	Phase extraction	85
3.2.3	Numerical simulation	90
3.2.4	Experimental results	94
<b>3.3</b>	<b>Conclusions</b>	<b>97</b>

---

In the previous chapter the effect of vortex filtering for non-scattering objects was analyzed. But, when the object is rough enough to produce scattering, the properties of vortex filtering varies in comparison with non-scattering phase objects. In this chapter the effect of vortex filtering for this condition is analyzed. For this chapter a brief introduction on speckle and speckle interferometry are presented as well as an experimental setup which involves the process of vortex filtering explaining the effect of this process when objects with rough surfaces are considered.

### 3.1 Introduction

Speckle patterns are formed when a rough object is illuminated with coherent or partially coherent light sources. However for the analysis presented here will be restricted to the use of monochromatic light, usually produced by lasers. For the analysis a material surface of roughness greater than the wavelength of the light  $\lambda$ , illuminated as shown in Fig. 3.1a. Each element of area absorbs and diffuses the light it receives, so those areas can be considered as individual coherent light sources  $S_i, S_j$  [98]. A point  $P$  of the detector is illuminated by the individual sources generated by the rough surface. Each one of the waves has an amplitude and a phase and can be written as  $a_n \exp i\varphi_n$  at the point  $P$  or in its phasor form represented in vectors as shown in Fig. 3.1b. Where  $a_n$  is the amplitude of each individual source and  $\varphi_n$  its phase.

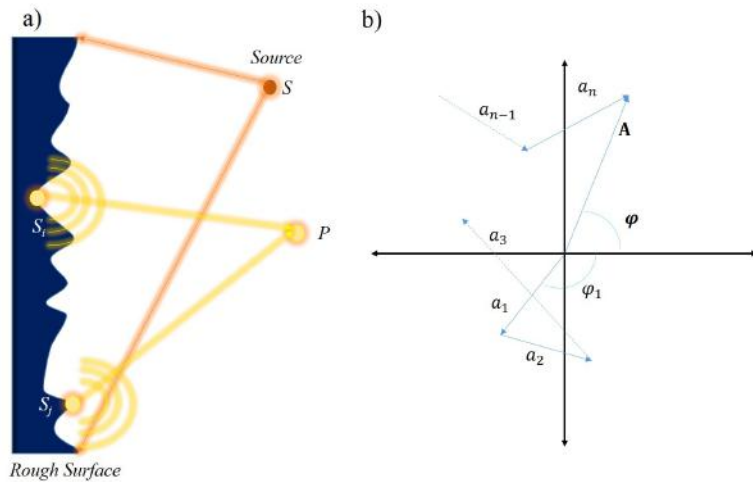


Figure 3.1. Speckle formation over a detector  $P$ . a) Objective Speckle formation on a rough surface, b) random phasor on  $P$ .

Because of the roughness of the surface the phase and modulus of the individual light sources is random. That is why the sum of this phasor can be represented as the sum of all the contributions of the individual light sources. The amplitude  $\mathbf{A}$  at the point  $P$  of the detector is equivalent to the result of a random walk in a plane as observed on 3.1b[99].



### 3.1.1 Speckle pattern properties

The real and imaginary parts of the phasor  $\mathbf{A}$  are Gaussian random variables. This vector is called "circular complex Gaussian random variable" [100], if a transformation on the real and imaginary part of the phasor  $\mathbf{A}$  and the couple  $(I, \varphi)$  a probability density function of the intensity  $I = \mathbf{A}\mathbf{A}^*$  and the phase  $\varphi$  can be obtained. For the ideal case when the speckle phase is uniformly distributed over  $[0, 2\pi]$  the probability density function can be written as

$$P(I) = \exp\left(-\frac{I}{\langle I \rangle}\right), \quad (3.1)$$

where  $\langle I \rangle$  is the mean intensity value also known as the first momentum [101].

The intensity pattern  $I$  can be seen on Fig. 3.2a. Here it can be observed that low intensities are more probable than high intensity values. This speckle pattern can be obtained on a lensless CCD camera. High intensity regions tend to saturate the detector locally but dark regions represent a larger portion on the image. This can be confirmed by the histogram of the image shown on Fig. 3.2b. Which is related to the probability density function explained on Eq. (3.1).

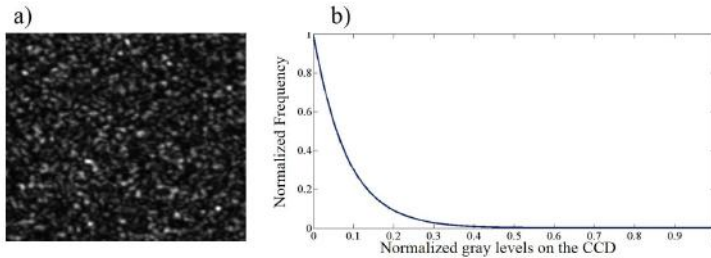


Figure 3.2. Speckle pattern. a) Probability function, b) pattern recorded by a CCD camera.

However the probability density function shown on Eq. (3.1) can be only applied if the detector sampling is infinitely small. If the intensity is measured with a detector such as a camera pixel, the sampling is done by the pixel area where an integration of the intensity takes place. This affects the probability distribution, which now depends of an integration factor  $m$

given by the ratio of speckles that are integrated in the pixel area resulting in a density function given by

$$P(I') = \frac{1}{\Gamma(m)} \left( \frac{m}{\langle I' \rangle} \right)^m I'^{m-1} \exp \left( -m \frac{I'}{\langle I' \rangle} \right), \quad (3.2)$$

where  $I'$  is the intensity distribution that has been modified by the integration of the speckle on the detector. The influence of this integration phenomena on the probability density function can be observed in Fig. 3.3. It can be observed that for larger values of  $m$  the probability density function of the intensity pattern tends toward a Gaussian distribution.

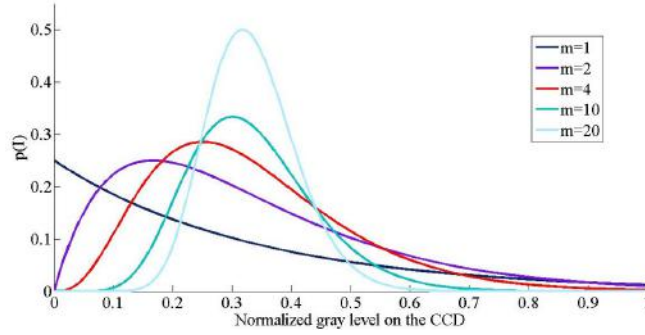


Figure 3.3. Influence of the integration of speckles on the probability density function of the intensity.

### 3.1.1.1 Average speckle dimensions

It can be seen in Fig. 3.2a that some "grains" on the intensity distribution can be defined as regions of roughly constant intensity. The average lateral size of these grains can be estimated by using the first zero of the autocorrelation of the intensity. This size depends on the shape of the illuminated region. For a circular area, the lateral and longitudinal average widths  $w_l$  and  $w_L$  can be described by [102]

$$w_l \approx \frac{\lambda d}{\sigma_o} \quad \text{and} \quad (3.3)$$

$$w_L \approx \frac{8\lambda d^2}{\sigma_o^2} \quad , \quad (3.4)$$

where  $\lambda$  is the wavelength of the light,  $d$  is the distance between the illumination diffusing area of width  $\sigma_o$  and the plane where the speckle is observed as seen on Fig. 3.4.

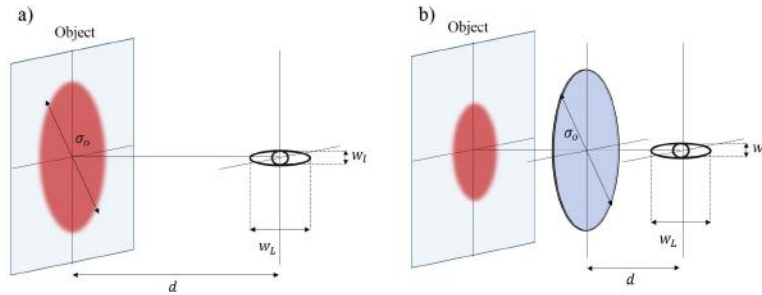


Figure 3.4. Average speckle dimension for an illuminated area shown in red. a) Objective speckle size, b) subjective speckle size.

The first case shown on Fig. 3.4a, is called objective speckle. But if the speckle pattern is formed after a lens as shown in Fig 3.4b, the lens pupil causes the speckle effect. So, the same formulas are applied for each speckle size. But with the pupil calculated either from the illuminated area or from the lens aperture, with the respective distance  $d$  either from the illuminated area or from the lens aperture.

For variations around the illumination wavelength of the illumination direction or object position in space the speckle patterns are preserved approximately with the same shape. This means that the shape is related to the diffuser roughness. However large displacements or deformations will change the fine grain structure of the speckle pattern creating a new speckle pattern, no longer correlated with the initial one. However, when the speckle grains retain their shape this makes possible to use them in metrological applications, such as speckle photography or speckle interferometry [103].

One of the effects that is frequently avoided, is the decorrelation of the speckle pattern. Which correspond to an alteration of the amplitude and phase of the speckle field between the two exposures that allows to the measure a deformation of an illuminated area. There are different kind of decorrelations that influence the total decorrelation of the speckle pattern on the observation field, such as image plane and pupil plane decorrelation [104, 105]. Both decorrelations produce phase in speckle interferometry [106]. Thus is highly recommended to avoid this effect.

### 3.1.2 Out-of-plane measurement

Speckle interferometry had its origins in 1971 [98], being the correlation on photographic plates the first one used in order to record the correlation speckle patterns using fringe patterns. The analysis of deformation or contouring has been shown to be proportional to the number of fringes. Contrary to classic interferometry, speckle techniques requires two speckle patterns in order to observe correlation fringes, from which the measurement of displacement or deformation can be computed. The first step of most speckle experiments consist of recording the intensity of the speckle pattern on its reference state, meaning no deformation is introduced as seen in Fig. 3.5a. This initial intensity speckle pattern can be written as:

$$I(x, y) = a(x, y) + b(x, y) \cos(\varphi_i(x, y)), \quad (3.5)$$

this equation corresponds to the intensity pattern on a CCD shown in Fig. 3.5c, where  $a(x, y)$  and  $b(x, y)$  are the background signal and the visibility of the intensity pattern respectively, and  $\varphi_i(x, y)$  is the initial phase variation, which includes the random phase of the speckle. It can be seen that for an out-of-plane interferometer a reference beam interferes with a beam which carries the information of the object. And then recorded over the CCD as shown on Fig. 3.6.

After the object is deformed as seen on Fig. 3.5b, a second image of the speckle pattern is recorded. This intensity pattern denoted by  $\tilde{I}(x, y)$  is frequently recorded over a camera as shown in the image of Fig. 3.5d, this intensity pattern can be described as

$$\tilde{I}(x, y) = \tilde{a}(x, y) + \tilde{b}(x, y) \cos(\varphi_d(x, y)). \quad (3.6)$$

By comparing Eq. (3.5) and Eq. (3.6) it can be seen that the form is the same. However, for the intensity pattern that corresponds to the deformation  $\tilde{I}(x, y)$ , the phase  $\varphi_d(x, y)$  includes the deformation phase.

As both phases  $\varphi_i(x, y)$  and  $\varphi_d(x, y)$  are affected by the random variables of the speckle there are no fringes over the intensity patterns  $I(x, y)$  and  $\tilde{I}(x, y)$  as shown on Fig. 3.5c and d. However correlation fringe pattern can be obtained if the square difference between the two intensity pattern is calculated as follow

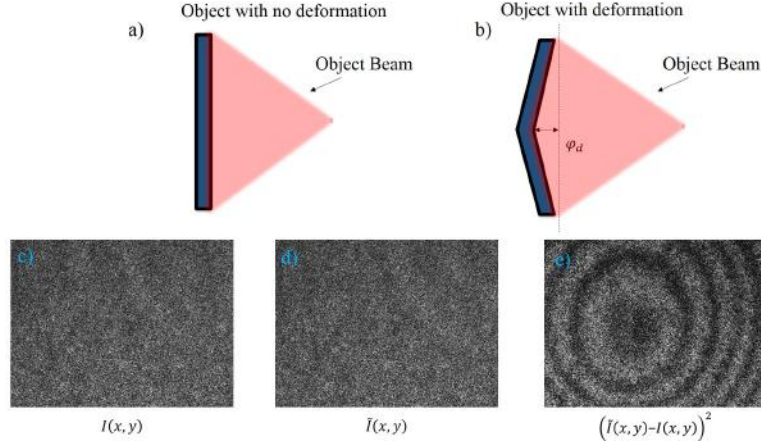


Figure 3.5. Example of out-of-plane correlation fringes. a) Object with no deformation, b) object with deformation, c) intensity pattern on the CCD with no deformation, d) intensity pattern on the CCD with deformation, e) correlation fringe pattern.

$$\left(\tilde{I}(x, y) - I(x, y)\right)^2 = 2b^2(x, y) \sin^2 \left( \varphi_i(x, y) + \frac{1}{2}\varphi_d(x, y) \right) (1 - \cos \varphi_d(x, y)) \quad (3.7)$$

This correlation fringe pattern can be observed in Fig. 3.5e, where fringes that corresponds to the deformation can now be observed. Using these correlation patterns, deformation as well other phenomena such as vibration can be measured by Electronic Speckle Pattern Interferometry (ESPI) [107, 108, 109, 110].

For an out-of-plane ESPI system, the only component of the optical path difference that is different from zero lies along the  $z$  axis, that's why the correlation fringes gives only information of the deformation such that is perpendicular to the object plane.

From the setup shown in Fig. 3.6 it can be observed that a small portion of the laser beam is divided by a beamsplitter plate that directs the light through a lens onto the detector, this is known as the reference beam. Most of the initial laser beam is used to illuminate the object which is then imaged to the camera detector by the lens. The sensitivity or amount of object deformation along the  $z$ - axis that produces one correlation fringe is

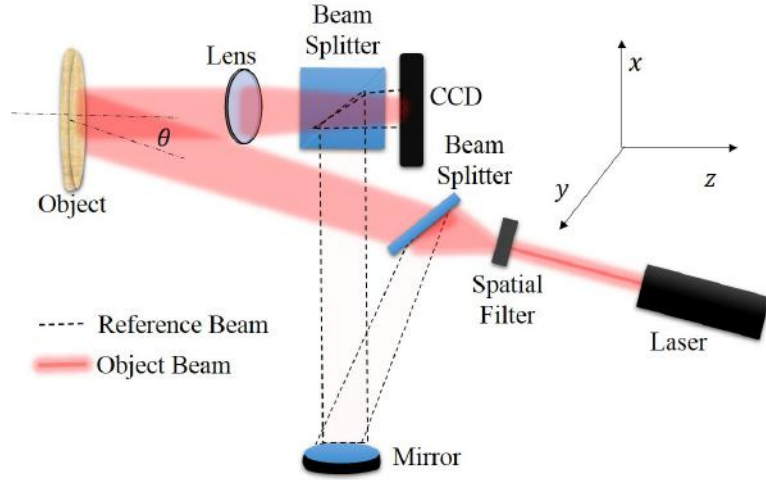


Figure 3.6. Example of out-of-plane interferometer.

$$s_z = \frac{\lambda}{1 + \cos \theta}, \quad (3.8)$$

where  $\theta$  is the angle between the illumination light beam and the observation direction from the entrance pupil of the system. So it is desirable that the angle between the the illumination beam and the object normal becomes the smallest as possible, so the sensitivity of the system improves.

by construction the sensitivity along the  $y$ -axis is zero. It has to be pointed out that the maximum sensitivity of this arrangement is  $\lambda/2$ . This high sensitivity means that the smallest environmental perturbation in the experimental will translate in perturbation of the fringe pattern.

### 3.1.3 In-plane measurement

The typical in-plane speckle interferometer is shown in Fig. 3.7, it can be seen that two uniform beams are directed to the object by means of two mirrors. In a well adjusted optical setup, both beams should illuminate the object under symmetrical orientation with respect to the normal of the object,  $\theta_1 = -\theta_2$ .

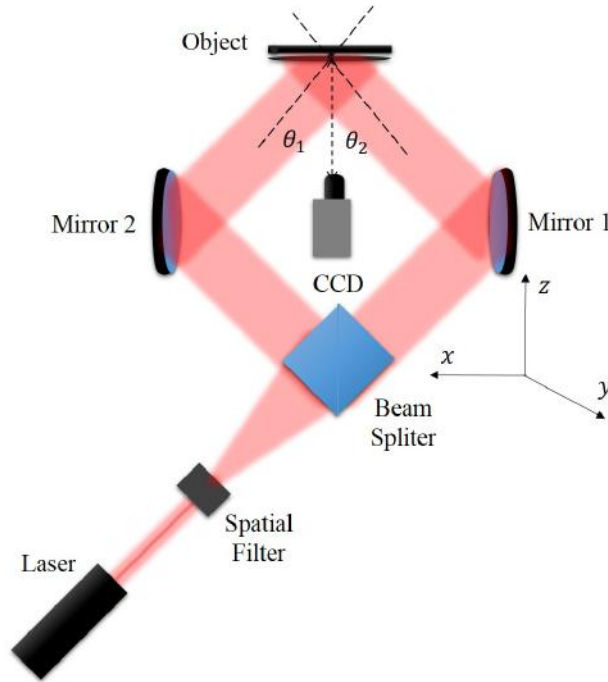


Figure 3.7. Example of in-plane ESPI.

The phase of the two speckle fields that interferes changes but as the optical path difference is given by their difference there is only sensitivity through the axis  $x$ . The sensitivity of an in-plane setup is described by

$$s_x = \frac{\lambda}{2 \sin \theta}, \quad (3.9)$$

where the out plane sensitivity  $s_z$  is zero. But for points where the two angles are no longer symmetrical, the  $x$ -axis sensitivity in-plane becomes

$$s_x = \frac{\lambda}{\sin \theta_1 - \sin \theta_2}, \quad (3.10)$$

while the out-plane sensitivity along the  $z$ -axis becomes

$$s_z = \frac{\lambda}{\cos \theta_1 - \cos \theta_2}. \quad (3.11)$$

As is the case of an out-of-plane interferometer, there is a small sensitivity to  $y$ -axis in-plane displacement. It can be observed that the illumination position affects the sensitivity of the interferometer. Therefore, it is usual that the sensitivity to few tens of  $\lambda$  or up to  $\lambda/1.8$  [103].

Interpretation of in-plane correlation fringes can be not an easy task or as intuitive as for the out-of-plane interferometer, it is not only used for displacement measurement [111] or vibration analysis as out-of-plane interferometer [112]. But for a rotation of the object in plane  $xy$ . For example, on Fig. 3.8a a bar is bend over two points, generating a correlation fringe pattern shown in Fig. 3.8b composed by parallel lines denoting a small rotation of the bar plus the bending deformation. This rotation detection capability can be applied for in other areas such as medicine [113].

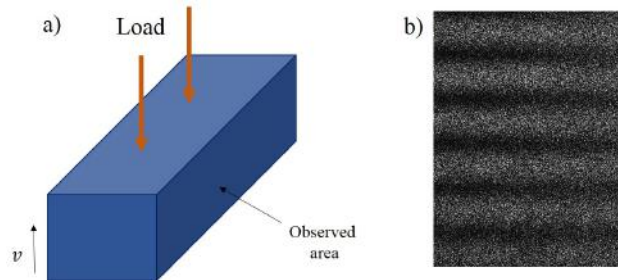


Figure 3.8. Displacement by a load measured by an in-plane optical setup. a) Induced force over a bar causing a displacement  $v$ , b) experimental in-plane displacement fringes over the observed area.



### 3.1.4 Speckle shearing interferometer

Fig. 3.9 shows a schematic diagram of a speckle shearing interferometer, a single light beam illuminates the object, where the reflected light is collected by the camera through a Michelson interferometer and a lens. One of the images is formed directly onto the CCD, as seen on Fig. 3.10a. However the other image is formed by the mirror that is slightly inclined producing lateral shifted on the detector as seen on Fig. 3.10b. Here the two speckle fields interfere at one given point of the detector corresponding to two spaced points on the object, as seen on Fig.3.10c by an amount  $\Delta x$  [114].

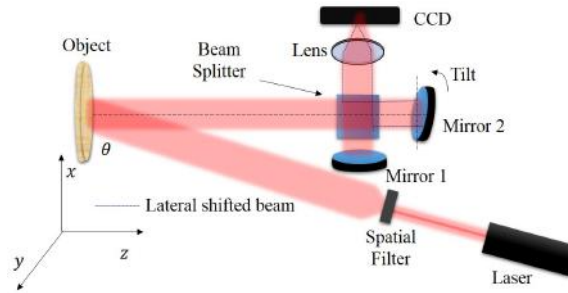


Figure 3.9. Schematic diagram of an optical setup of a speckle shearing interferometer.

The phase change of the interferogram is proportional to the difference of the displacement of the two points [101]

$$\Delta\phi = k \frac{\partial w}{\partial x} (\cos(\theta) + 1) \Delta x, \quad (3.12)$$

where  $w$  is the displacements of the points along the  $z$ -axis,  $\theta$  the angle between the normal of the object and the mirror and  $k$  is the wave number.

Speckle shearing interferometry is a technique sensitive to the derivative of the displacement in the direction of shear. Being used in several application such as strain measurement [115, 116], vibration analysis [117], and surface displacement measurement [118, 114]. Also this type of ESPI technique has been subject of study as the superposed images produce error when the phase is recovered [101], computational algorithms have been designed to solve that problem [119].

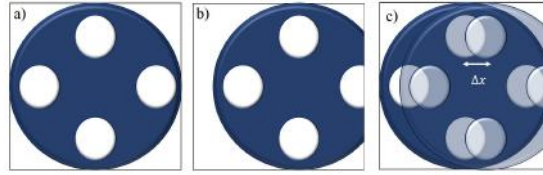


Figure 3.10. Example of an object seen in the camera detector on a shearing interferometer configuration. a) Reference object, b) object displaced by the mirror a distance  $\Delta x$ , c) superposition of the reference object and the shifted version of the object recorded by the camera detector.

### 3.2 Displacement measurement with multi-level spiral phase plate in out-of-plane speckle interferometry

Speckle Interferometry is a technique for displacement measurements that uses rough surfaces illuminated by laser light, assuming that such surfaces are capable of generating fully developed speckle patterns [98]. Given the random nature of the speckle phase, there are chances that optical vortices occur naturally in speckle interferometry, and its density has been found to depend on the roughness of the samples [120]. Tracking of the vortex positions has allowed applications for nanometric displacement measurement [121] and dynamic speckle from biological samples [122]. Recently, continuous phase vortices have been introduced for spiral phase contrast microscopy [23, 24]. Instead of generating vortices in the image field, the phase vortex is used as a spatial filter in microscopy techniques where the speckle present is not fully developed. In practice the continuous phase vortices used in microscopy are difficult to generate, and not entirely appropriate for high speed speckle correlation interferometry. Therefore, a multi-level spiral phase with specific phase steps is proposed here to simplify its generation, aiming to increase processing speed and reduce complexity in the phase extraction process of speckle correlation fringes. Our aim was to process fully developed speckle patterns of an out-of-plane speckle interferometer which includes a multi-level spiral phase filter, and finding ways of extracting the juxtaposed phase in the vortex filtered speckle pattern (VF-SP). Since the technique uses a single phase vortex in the Fourier domain, we assumed that a modification of this vortex would simultaneously affect the phase of each speckle in the spatial domain. In particular, it is shown that phase stepping in the

whole spatial domain can be easily implemented for each random phase of unresolved speckles by the simple expedient of rotating the proposed multi-level spiral filter included in the ESPI system. Furthermore, it also shown that the correlation of VF-SPs makes unnecessary the deconvolution procedures used in microscopy for the purpose of phase extraction. Since vortex rotation can be controlled with high accuracy, the required phase stepping is achieved with comparable precision. Therefore, piezo-electric transducer (PZT) problems, such as wobbling and hysteresis, are avoided with this technique [123].

### 3.2.1 Introduction

In polar coordinates  $(\rho, \theta)$ , the complex amplitude of a phase vortex of order one, with its angular discontinuity at  $\theta_n$ , is  $\exp[i(\theta - \theta_n)]$ , where  $0 \leq \theta - \theta_n < 2\pi$ . When this continuous spiral phase object is used as a spatial filter, like in the case of microscopy, the spatial filtering operation can be represented as

$$U_i^{(n)}(x_i, y_i) = \mathcal{F}^{-1} \left\{ H^{(n)}(u, v) \mathcal{F} \{ P(x_o, y_o) U_o(x_o, y_o) \} \right\}, \quad (3.13)$$

where  $\mathcal{F}$  and  $\mathcal{F}^{-1}$  are, respectively, the forward and inverse Fourier transform operators,

$$U_o(x_o, y_o) = A(x_o, y_o) \exp[i\varphi(x_o, y_o)], \quad (3.14)$$

is the object complex amplitude distribution,  $P(x_o, y_o)$  is the generalized pupil function, and

$$H^{(n)}(u, v) = \text{circ} \left( \frac{\rho}{\rho_0} \right) \exp[i\psi_n(u, v)], \quad (3.15)$$

where

$$H^{(n)}(u, v) = H^{(n)} \left( \frac{x_f}{\lambda f}, \frac{y_f}{\lambda f} \right), \quad (3.16)$$

is the transfer function of the filter,  $x_f, y_f$  are Cartesian coordinates at the spatial frequency plane,  $f$  the focal length of the Fourier transforming lens, and  $\lambda$  the illumination wavelength. The amplitude  $A(x_o, y_o)$  and the phase  $\varphi(x_o, y_o)$  in Eq. (3.14) are random functions if rough surfaces are used to generate  $U_o(x_o, y_o)$ . In Eq. (3.15)  $\rho = \sqrt{u^2 + v^2}$ , and  $\rho_0 = l_{y_f}/(\lambda f)$  is the radius of the filter in spatial frequency units, where  $2l_{y_f}$  is the smaller side

of the SLM - typically, its height. This radius, however, can be reduced with an iris diaphragm if we want to increase the speckle size in the output intensity distribution [124].

Finally, in the same equation  $\psi_n(u, v)$  is the vortex phase as function of the spatial frequencies  $u = \rho \cos \theta$  and  $v = \rho \sin \theta$  [80]. As usual,  $\text{circ}(\rho/\rho_0) = 1$  if  $\rho \leq \rho_0$ , and zero otherwise. In this description we assume that the object is placed at the front focal plane of the Fourier transforming lens, and that vignetting is neglected.

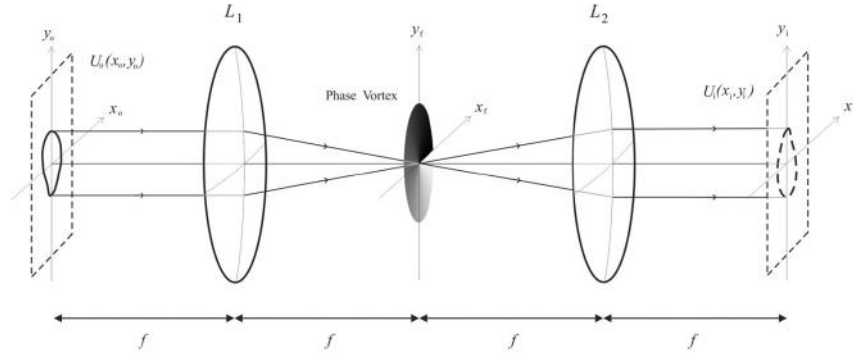


Figure 3.11. Schematic diagram of a  $4f$  optical correlator with a phase vortex filter represented in gray levels.

The filtering operation can be easily implemented in a  $4f$  optical system, in which the phase vortex is inserted, and its radius adjusted, in the frequency plane  $(x_f, y_f)$ , as shown in Fig. 3.11. In this system, the Fourier transform of the complex amplitude distribution  $P(x_o, y_o) U_o(x_o, y_o)$ , generated by coherent light scattered from a rough surface at the plane  $(x_o, y_o)$ , and bounded by the pupil function  $P(x_o, y_o)$ , is obtained at the back focal plane  $(x_f, y_f)$  of the lens  $L_1$ . The vortex filter, shown with its angular discontinuity  $0 - 2\pi$  oriented in the positive direction of the  $u$  axis, adds its phase to the phase of the spectrum  $G_f(u, v) = \mathcal{F}\{P(x_o, y_o) U_o(x_o, y_o)\}$ , and the resulting complex amplitude is Fourier transformed by the lens  $L_2$  to generate the VF-SP at the plane  $(x_i, y_i)$ . This VF-SP can be seen as the contribution of Dirac deltas that were filtered by the vortex filter and added on the image plane; here the PSF of the 4-step vortex as seen on Fig. 3.12.

In practice, small angular phase increments, like those required to produce acceptable vortices, are difficult to make with digital devices. They have been made with deformable mirrors [125], and also with digital SLMs, mainly

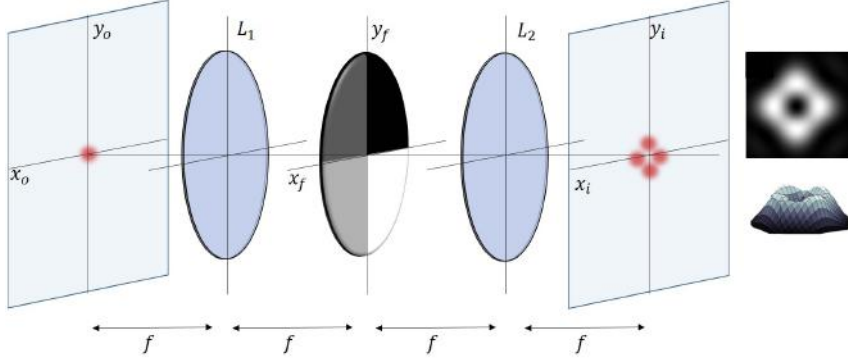


Figure 3.12. Influence of the four-step vortex on the speckle.

LCoSs [24], and more recently with digital micro-mirror devices (DMD) [126].

To understand the effects to which the phase transformations at the frequency plane  $(u, v)$  give rise, we shall consider a discrete phase vortex made up of four steps, one for each quadrant of the Cartesian coordinate system. For a vortex of order one, it implies a phase increment of  $\pi/2$  between two contiguous steps, except at the original phase discontinuity, where the step size becomes  $3\pi/2$ . A similar approach to generate a phase vortex, but with polarizing elements, was reported in [127].

The phase configurations of the four discrete vortices that we need, one for each orientation of the major vortex discontinuity, can be found with further detail on section 2.2.2.1.

### 3.2.2 Phase extraction

A reference field to the field of the VF-SP,  $U_i^{(n)}(x_i, y_i)$  is added. For simplicity, it is assumed that this reference beam is parallel, and incides normally to the camera CCD, with a constant amplitude  $a_r$ . We shall then record at this plane the intensity distribution

$$\begin{aligned} I^{(n)}(x_i, y_i) &= \left| a_r + U_i^{(n)}(x_i, y_i) \right|^2 \\ &= \left| a_r + \mathcal{F}^{-1} \left\{ H^{(n)}(u, v) G_f(u, v) \right\} \right|^2. \end{aligned} \quad (3.17)$$

Since

$$\begin{aligned}
H^{(n)}(u, v) &= \text{circ} \left( \frac{\rho}{\rho_0} \right) \exp [i \psi_n(u, v)] \\
&= \text{circ} \left( \frac{\rho}{\rho_0} \right) \exp \left[ i \frac{\pi}{2} \sum_{j=1}^4 r_{n,j} q_j(u, v) \right],
\end{aligned} \tag{3.18}$$

and

$$r_{n,j} = r_{1,j} + n - 1 \pmod{4} \tag{3.19}$$

$$\begin{aligned}
H^{(n)}(u, v) &= \text{circ} \left( \frac{\rho}{\rho_0} \right) \exp(i \psi_1) \exp \left[ i(n-1) \frac{\pi}{2} \sum_{j=1}^4 q_j(u, v) \right] \\
&= \exp \left[ i(n-1) \frac{\pi}{2} \right] H^{(1)}(u, v),
\end{aligned} \tag{3.20}$$

given that

$$\sum_{j=1}^4 q_j(u, v) = H(u)H(v) + H(-u)H(v) + H(-u)H(-v) + H(u)H(-v) = 1. \tag{3.21}$$

Therefore, if we use Eq. (3.20) in Eq. (3.21) we have

$$\begin{aligned}
I^{(n)}(x_i, y_i) &= \left| a_r + \mathcal{F}^{-1} \left\{ H^{(n)}(u, v) G_f(u, v) \right\} \right|^2 \\
&= \left| a_r + \exp \left[ i(n-1) \frac{\pi}{2} \right] \mathcal{F}^{-1} \left\{ H^{(1)}(u, v) G_f(u, v) \right\} \right|^2 \\
&= \left| a_r + \exp \left[ i(n-1) \frac{\pi}{2} \right] U_i^{(1)}(x_i, y_i) \right|^2.
\end{aligned} \tag{3.22}$$

Developing the last equation it is obtained

$$I^{(n)}(x_i, y_i) = a(x_i, y_i) + b(x_i, y_i) \cos \left[ \varphi_i(x_i, y_i) + (n-1) \frac{\pi}{2} \right], \tag{3.23}$$

where

$$\begin{aligned}
 a(x_i, y_i) &= a_r^2 + \left| U_i^{(1)}(x_i, y_i) \right|^2, \\
 b(x_i, y_i) &= 2a_r \left| U_i^{(1)}(x_i, y_i) \right|, \\
 \varphi_i(x_i, y_i) &= \arg \left[ U_i^{(1)}(x_i, y_i) \right].
 \end{aligned} \tag{3.24}$$

from Eq. (3.23) follows that

$$\begin{aligned}
 I^{(1)}(x_i, y_i) &= a(x_i, y_i) + b(x_i, y_i) \cos[\varphi_i(x_i, y_i)], \\
 I^{(2)}(x_i, y_i) &= a(x_i, y_i) - b(x_i, y_i) \sin[\varphi_i(x_i, y_i)], \\
 I^{(3)}(x_i, y_i) &= a(x_i, y_i) - b(x_i, y_i) \cos[\varphi_i(x_i, y_i)], \\
 I^{(4)}(x_i, y_i) &= a(x_i, y_i) + b(x_i, y_i) \sin[\varphi_i(x_i, y_i)].
 \end{aligned} \tag{3.25}$$

Therefore,

$$\tan[\varphi_i(x_i, y_i)] = \frac{I^{(4)}(x_i, y_i) - I^{(2)}(x_i, y_i)}{I^{(1)}(x_i, y_i) - I^{(3)}(x_i, y_i)} = z(x_i, y_i). \tag{3.26}$$

If we now displace the object, assuming that its microstructure remains undistorted, the object field becomes (Eq. (3.14))

$$\begin{aligned}
 \tilde{U}_o(x_o, y_o) &= A_o(x_o, y_o) \exp[i\tilde{\varphi}_o(x_o, y_o)], \\
 &= U_o(x_o, y_o) \exp\{i[\tilde{\varphi}_o(x_o, y_o) - \varphi_o(x_o, y_o)]\}, \\
 &= \exp[i\Delta\varphi_o(x_o, y_o)] U_o(x_o, y_o),
 \end{aligned} \tag{3.27}$$

where

$$\Delta\varphi_o(x_o, y_o) = \tilde{\varphi}_o(x_o, y_o) - \varphi_o(x_o, y_o) \tag{3.28}$$

is the phase increment introduced by the displacement. Thus, from Eq. (3.14) and (3.17) it is obtained

$$\tilde{I}^{(n)}(x_i, y_i) = \left| a_r + \exp\left[i(n-1)\frac{\pi}{2}\right] \tilde{U}_i^{(1)}(x_i, y_i) \right|^2, \tag{3.29}$$

where

$$\begin{aligned}
\tilde{U}_i^{(1)}(x_i, y_i) &= \mathcal{F}^{-1} \left\{ H^{(1)}(u, v) \mathcal{F} \left\{ P(x_o, y_o) \tilde{U}_o(x_o, y_o) \right\} \right\} \\
&= \mathcal{F}^{-1} \left\{ H^{(1)}(u, v) \mathcal{F} \left\{ \exp [i \Delta\varphi_o(x_o, y_o)] P(x_o, y_o) U_o(x_o, y_o) \right\} \right\}.
\end{aligned} \tag{3.30}$$

Since  $\Delta\varphi_o(x_o, y_o)$  is a slow varying function compared to the amplitude and phase of the object speckle field,  $U_o(x_o, y_o)$ , we can write

$$\begin{aligned}
\tilde{U}_i^{(1)}(x_i, y_i) &= \exp [i \Delta\varphi_i(x_i, y_i)] U_i^{(1)}(x_i, y_i) \\
&\simeq \exp [i \Delta\varphi_o(-x_i, -y_i)] U_i^{(1)}(x_i, y_i).
\end{aligned} \tag{3.31}$$

In other words, the phase increments introduced by the displacement of the object at the object and the image fields are approximately equal at conjugate points  $(x_i, y_i) = (Mx_o, My_o) = (-x_o, -y_o)$ , where  $M$  is the magnification of the system, which is in the case of a  $4f$  correlator. Therefore

$$\begin{aligned}
\tilde{I}^{(1)}(x_i, y_i) &= \tilde{a}(x_i, y_i) + \tilde{b}(x_i, y_i) \cos [\tilde{\varphi}_i(x_i, y_i)], \\
\tilde{I}^{(2)}(x_i, y_i) &= \tilde{a}(x_i, y_i) - \tilde{b}(x_i, y_i) \sin [\tilde{\varphi}_i(x_i, y_i)], \\
\tilde{I}^{(3)}(x_i, y_i) &= \tilde{a}(x_i, y_i) - \tilde{b}(x_i, y_i) \cos [\tilde{\varphi}_i(x_i, y_i)], \\
\tilde{I}^{(4)}(x_i, y_i) &= \tilde{a}(x_i, y_i) + \tilde{b}(x_i, y_i) \sin [\tilde{\varphi}_i(x_i, y_i)],
\end{aligned} \tag{3.32}$$

with

$$\begin{aligned}
\tilde{a}(x_i, y_i) &= a_r^2 + \left| \tilde{U}_i^{(1)}(x_i, y_i) \right|^2 = a(x_i, y_i), \\
\tilde{b}(x_i, y_i) &= 2a_r \left| \tilde{U}_i^{(1)}(x_i, y_i) \right| = b(x_i, y_i), \\
\tilde{\varphi}_i(x_i, y_i) &= \arg \left[ \tilde{U}_i^{(1)}(x_i, y_i) \right] = \varphi_i(x_i, y_i) + \Delta\varphi_i(x_i, y_i).
\end{aligned} \tag{3.33}$$

From Eq. (3.32)

$$\tan [\tilde{\varphi}_i(x_i, y_i)] = \frac{\tilde{I}^{(4)}(x_i, y_i) - \tilde{I}^{(2)}(x_i, y_i)}{\tilde{I}^{(1)}(x_i, y_i) - \tilde{I}^{(3)}(x_i, y_i)} = \tilde{z}(x_i, y_i), \tag{3.34}$$



from Eq. (3.34) and Eq. (3.26)

$$\Delta\varphi_i(x_i, y_i) = \tilde{\varphi}_i(x_i, y_i) - \varphi_i(x_i, y_i) = \tan^{-1} \left[ \frac{\tilde{z}(x_i, y_i) - z(x_i, y_i)}{1 + \tilde{z}(x_i, y_i)z(x_i, y_i)} \right]. \quad (3.35)$$

Therefore, the phase increment that we sought is given by

$$\Delta\varphi_o^{(e)}(x_o, y_o) \simeq \Delta\varphi_i(-x_i, -y_i), \quad (3.36)$$

where the superscript e stands for extracted, and the values of  $\Delta\varphi_i(-x_i, -y_i)$  can be found from Eq. (3.35).

An alternative method of phase extraction, the so called method of correlation fringes, consists in subtracting a reference interference pattern obtained prior to the object deformation, say  $I^{(1)}(x_i, y_i)$ , from an interference pattern obtained after the object deformation,  $\tilde{I}^{(n)}(x_i, y_i)$ . In such case, from Eq. (3.23) and the equivalent equation for  $\tilde{I}^{(n)}(x_i, y_i)$ , it can be obtained

$$\begin{aligned} I^{(n)}(x_i, y_i) &= \left[ \tilde{I}^{(n)}(x_i, y_i) - I^{(1)}(x_i, y_i) \right]^2 \quad (3.37) \\ &= b^2(x_i, y_i) \left\{ \cos \left[ \tilde{\varphi}_i(x_i, y_i) + (n-1)\frac{\pi}{2} \right] - \cos[\varphi_i(x_i, y_i)] \right\}^2 \\ &= 2b^2(x_i, y_i) \sin^2 \left[ \varphi_i(x_i, y_i) + \frac{\Delta\varphi_i(x_i, y_i)}{2} + (n-1)\frac{\pi}{4} \right] \\ &\quad \times \left\{ 1 - \cos \left[ \Delta\varphi_i(x_i, y_i) + (n-1)\frac{\pi}{2} \right] \right\}. \end{aligned}$$

Eq. (3.37) allows the extraction of  $\Delta\varphi_i(x_i, y_i)$  from the usual four steps method, after filtering out the  $\sin^2(\dots)$ , high frequency, factor from the previous expression. After this,  $\Delta\varphi_o^{(e)}(x_o, y_o)$  can again be readily approximated with Eq. (3.36).

Similar equations for phase extraction can be found in the case of continuous phase vortices, and also of phase vortices with topological charges different from 1 - with phase spans larger than  $2\pi$ . At any rate, with the method that we propose here, the phase steps that are required for phase extraction can be accurately controlled by the vortex orientation, without the need of an elaborate calibration procedure to avoid detuning errors - like in the case of PZTs. The maximum speed for the rotation of the vortex depends on the

device that we use to produce it. New, non-LC, SLMs have been recently introduced to increase the video rate speeds of current LC devices, with an almost instantaneous response [128].

### 3.2.3 Numerical simulation

To verify the phase extraction equations, Eqs. (3.35) and (3.37), we devised a numerical simulation of an out-of-plane ESPI system working with VF-SPs. Preliminary values for the amplitude  $A_o(x_o, y_o)$  and phase  $\varphi_o(x_o, y_o)$  of the object field were obtained with a random number generator. These values were subsequently filtered with a low-pass filter, so that the speckle size of the field  $U_o(x_o, y_o)$  was adjusted through the cut-off spatial frequency of the filter. The field  $U_i(x_i, y_i)$  at the image plane of the  $4f$  correlator (Fig. 3.11) was obtained after two numerical Fourier transformations, indicated in Eqs. (3.13) and (3.15). After computing this field, the intensity resulting from the superposition of  $U_i^{(n)}(x_i, y_i)$  and a plane wave of constant amplitude  $r$  and zero phase is found. As a result of this numerical simulation, the intensity distributions  $I^{(n)}(x_i, y_i)$  and  $\tilde{I}^{(n)}(x_i, y_i)$  were obtained, in the second case after adding a Gaussian phase increment  $\Delta\varphi_o(x_o, y_o) = 2\pi\frac{h}{\lambda} \exp\left(-\frac{x_o^2+y_o^2}{w^2}\right)$  to the object phase  $\varphi_o(x_o, y_o)$ , with  $w = 5$  mm, and  $h = 4\lambda$ . The object area was  $10 \times 10$  mm<sup>2</sup>.

Fig. 3.13 shows the phase map that was extracted with an algorithm based on Eq. (3.35), for the Gaussian phase increment mentioned above. The map shown has been smoothed with a  $3 \times 3$  median filter. We can notice that the resemblance in shape, height ( $h/\lambda = 4$ ) and width ( $w = 5$ ) with the original phase increment map is quite close.

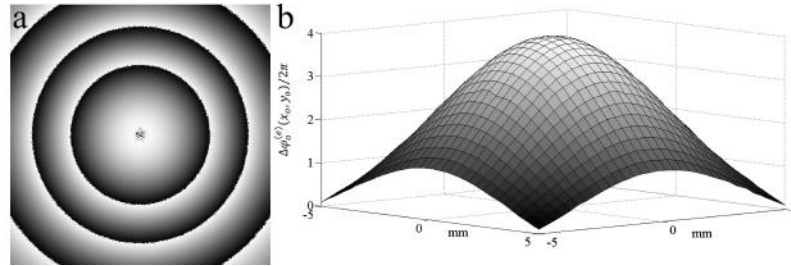


Figure 3.13. Phase map extracted with an algorithm based on Eq. (3.35).

The drawback of an algorithm based on Eq. (3.35) is that we need to record

eight intensity patterns, four before the displacement of the object, and four after. This number can be reduced to five if the phase increment is extracted from correlation fringe patterns, that is, with an algorithm based on Eq. (3.37). Fig. 3.14 shows a set of these patterns. After smoothing them with a low pass filter, we obtained the phase map shown in Fig. 3.15. It is similar to the map of Fig. 3.15, except that it still keeps some speckle noise. To remove it, a broad range of filters have been proposed: from simple filtering, such as neighborhood average, up to scale-space and regularization filters [129, 130].

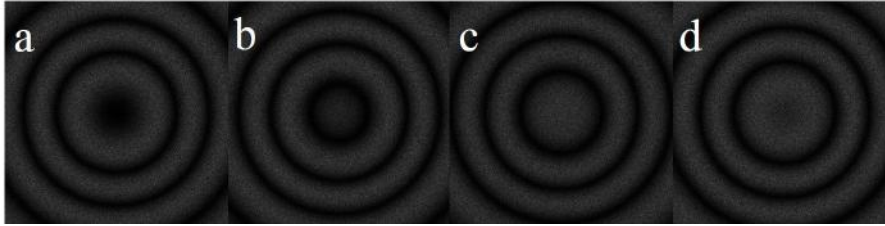


Figure 3.14. Correlation fringe patterns obtained with the numerical simulation: (a)  $I^{(1)}(x_i, y_i)$ ; (b)  $I^{(2)}(x_i, y_i)$ ; (c)  $I^{(3)}(x_i, y_i)$ ; (d)  $I^{(4)}(x_i, y_i)$ .

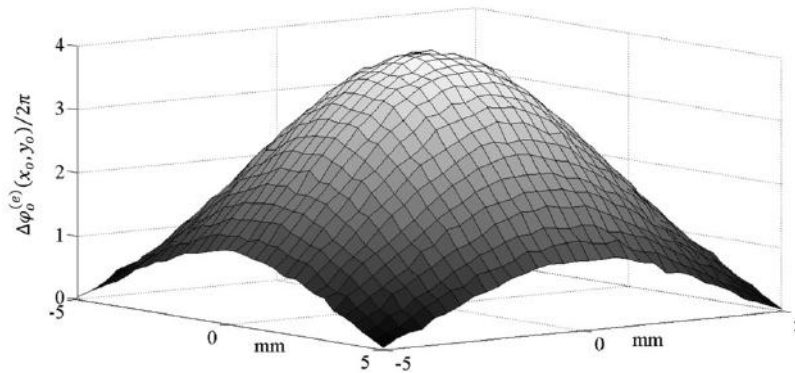


Figure 3.15. Extracted phase obtained from the correlation fringe patterns of Fig. 3.14 and an algorithm based on Eq. (3.37).

### 3.2.3.1 Effect of the aberrations of the phase filter

The phase vortices that we used were generated by a reflective spatial light modulator of the liquid crystal on silicon type (LCoS). Now, it is well known

that an active LCoS introduces an spurious phase throughout its surface, which corresponds to a wavefront aberration of several wavelengths [131]. This aberration is difficult to compensate with the LCoS itself, because the LCoS phase modulation depth is at the most  $3\pi$ , that is, the equivalent of an optical path difference (OPD) of only 1.5 wavelengths.

The effect of aberrations of phase vortices in spatial filtering has been studied in detail by Sharma and Senthil Kumaran [132]. We shall simulate here their effect in the case of speckle interferometry with VF-SPs, to see the extent to which the aberrations affect the phase which is extracted from the correlation fringes. For this end, a phase term needs to be added to the phase  $\psi^{(n)}(u, v)$  of the vortex, to take into account the wavefront aberration  $W(x_f, y_f)$  introduced by the LCoS. As a result of this addition, the filter transfer function becomes

$$H^{(n)}(u, v) = \exp \left\{ i \left[ \psi^{(n)}(u, v) + \frac{2\pi}{\lambda} W(\lambda f u, \lambda f v) \right] \right\}. \quad (3.38)$$

For moderate aberrations,  $W(x_f, y_f)$  can be adequately represented by a low order polynomial:

$$W(x_f, y_f)/\lambda = A \left( \frac{x_f}{l_{x_f}} \right)^2 + B \frac{x_f}{l_{x_f}} \frac{y_f}{l_{y_f}} + C \left( \frac{y_f}{l_{y_f}} \right)^2 + D \frac{x_f}{l_{x_f}} + E \frac{y_f}{l_{y_f}} + F, \quad (3.39)$$

where  $2l_{x_f}$  and  $2l_{y_f}$  are, respectively, the width and the height of the LCoS. Notice that the coefficients  $A, B, C, D, E$  and  $F$  in Eq. (3.38) are adimensional.

Table 3.1. Coefficients of the low order polynomial that we used to represent the wavefront aberration function of our LCoS.

Coefficient	Value
A	1.85
B	-0.59
C	2.85
D	0.04
E	0.05
F	-1.23

Fig. 3.16a shows an interferogram obtained with our LCoS in a Wyko interferometer. From the raw data of the interferometer (the OPDs given

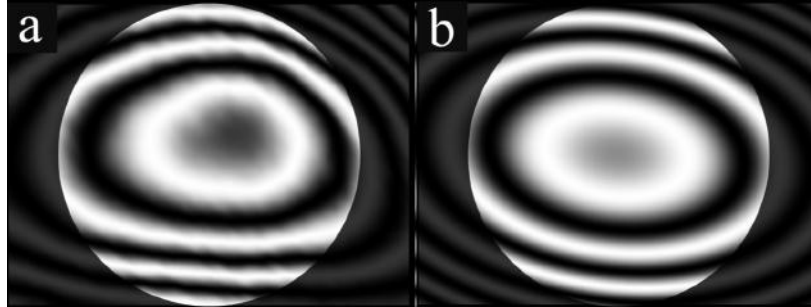


Figure 3.16. Interferograms of the LCoS obtained with a Fizeau interferometer (a), and generated after a least squares fit of a low order polynomial to the OPD values provided by the interferometer (b). The bright areas show the actual size that was given to the phase vortex filter with a diaphragm.

in micrometers for each pixel of the interferogram), we adjusted the low-order polynomial to the wavefront aberration measured in wavelengths ( $\lambda = 0.6328 \mu\text{m}$ ). Normalized pixel numbers were used to assign normalized coordinates  $x_f/l_f$  and  $y_f/l_f$  to the values of  $W(x_f, y_f)/\lambda$ . Table 3.1 shows the coefficients that we obtained. Fig. 3.16b shows the interferogram generated with the coefficients in this table.

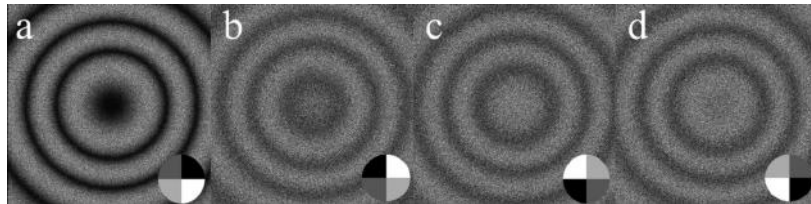


Figure 3.17. Progressive degradation of correlation fringes due to phase vortex aberrations. The circles on the lower right corner of each pattern show the filter orientation that was used to generate the pattern.

With Eq. (3.38) and the values of the coefficients in Table 3.1 we computed the correlation fringe patterns shown in Fig. 3.17, which clearly show a reduced contrast after the filter rotation. Nonetheless, with the values of  $I^{(n)}(x_i, y_i)$  that we used to find these patterns and Eq. (3.37) we could find the phase map in Fig. 3.18, that is close enough to the map that we obtained with the phase vortex that was free from aberrations (Fig. 3.15).

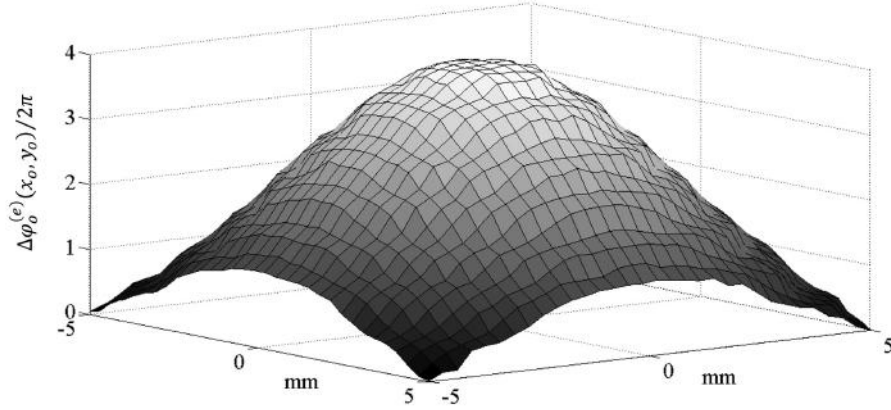


Figure 3.18. Extracted phase in the case of a moderately aberrated phase vortex filter. It was obtained from the correlation fringe patterns of Fig. 3.17 and an algorithm based on Eq. (3.37).

### 3.2.4 Experimental results

Fig. 3.19 shows the experimental setup for the out-of-plane deformation measurements. The light from a Nd-Yag laser  $L$  ( $\lambda = 532$ )nm is divided by a beam splitter  $BS_1$  into an object beam, shown with a solid line, and a reference beam, shown with a dashed line. The object beam is expanded with a microscope objective  $MO_1$  to illuminate an aluminum disk  $AD$ . The light scattered by the disk surface passes through a polarizer  $P_1$  and a half-wave plate  $HWP$ , which allows the adjustment of the plane of polarization of the object beam, before this incides on the LCoS (Liquid Crystal on Silicon) SLM (spatial light modulator). The aluminum disk is placed at the back focal plane of a lens  $L_1$ , with 400 mm focal length and 35 mm diameter. The LCoS, model LC-R 2500 by HoloeyeTM, and a 19 mm diameter diaphragm  $D$  are placed at the back focal plane of  $L_1$ , which also is the front focal plane of the lens  $L_2$ , a lens with the same focal length and diameter than  $L_1$ . The light reflected from the LCoS is brought to  $L_2$  by means of a non-polarizing beam splitter  $BS_2$ . The reference beam generated by the beam splitter  $BS_1$ , on the other hand, is directed by the mirrors  $M_1$ ,  $M_2$  and  $M_3$  to the microscope objective  $MO_2$ , also at the back focal plane of  $L_2$ . This lens collimates the beam, which incides normally at the  $CCD$ . For this work, the field of view of the spatial filtering system was restricted to that

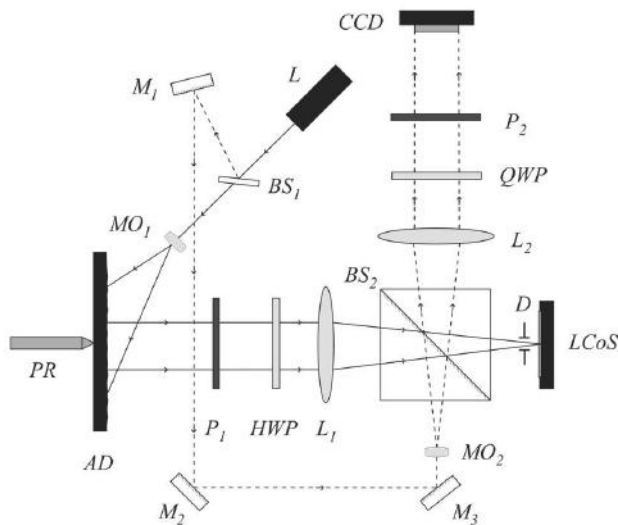


Figure 3.19. Experimental setup for out-of-plane displacement measurement using vortex filtering.

of a unit magnification, 4f system, so that the inspection area was approximately the size of the *CCD*. However, this limitation can be overcome, as shown, for instance, in [133, 134] for the case of shearography.

After  $L_2$ , the object beam and the reference beams present different states of polarization, reducing thus the contrast of the correlation fringes. To improve this contrast, a quarter wave plate *QWP* and a polarizer  $P_2$  were included before the *CCD* camera. Through rotations of *QWP* and  $P_2$  we could optimize the contrast of the correlation fringe pattern.

The aluminum disk *AD* was firmly clamped at its rim, and deformed with a pointed rod *PR*. The rod was fixed to a translation stage equipped with a micrometer head, where we could accurately read the displacement of the rod. Fig. 3.20 shows consecutive correlation fringe patterns obtained after the plate had been deformed, one pattern for each of the four vortex orientations displayed at the LCoS (Fig. 2.10). A slight decorrelation is observed on the fringe patterns that can be attributed to the phase vortex aberrations (Sec. 3.2.3.1) and to the flicker of the LCoS, which induces phase fluctuations within a band that can be as large as  $0.47\pi$ . This band, however, could be substantially reduced by cooling down the LCoS, as shown in [88]. Fig. 3.21 shows in gray levels the actual displacement map that we

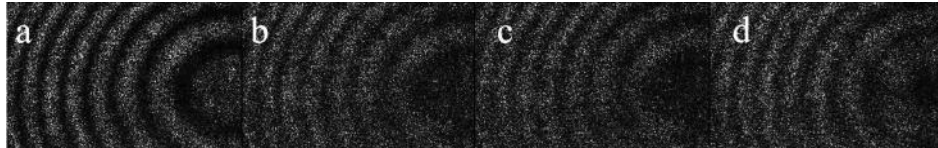


Figure 3.20. Experimental correlation pattern.

obtained from the correlation fringes of Fig. 3.20. We can notice that the maximum displacement was approximately  $2.4 \mu\text{m}$ , which agrees well with the number of correlation fringes in Fig. 3.20, and the displacement that we gave to the pointed rod.

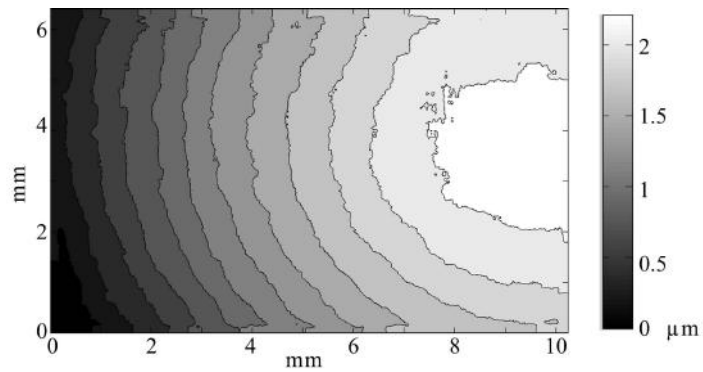


Figure 3.21. Displacement measurement.



### 3.3 Conclusions

In this chapter an alternative method of phase extraction from fringe correlation patterns obtained with vortex-filtered speckle patterns (VF-SP). We showed that these patterns can be generated by accurate phase stepping, which is achieved by three consecutive  $90^\circ$  turns of a 4-step spiral phase vortex.

The main advantage of this method of phase extraction is that an accurate phase stepping can be achieved easily, as the accuracy of the phase steps depends only on the precise rotation of the vortex filter, and this can be attained with ease using a spatial light modulator. Our technique is, therefore, virtually immune to detuning problems, unlike the case of PZTs, where hysteresis and wobbling must be taken into account. Even though the proposed setup has more components than the traditional out-of-plane interferometer arrangement, once the interferometer is built, the frequent phase re-calibration work of traditional ESPI is not required. In addition, the incorporation of very fast spatial light modulators into the electro-optics market in the near future will allow our method good control of phase stepping at very high speeds.

Also a theoretical justification of this method is deduced, and of a method based on the recording of eight VF-SP, one for each of the four vortex filter orientations, before and after the object is deformed. The equations derived from this analysis were experimentally tested, and also verified by numerical simulation.

Although aberrations in the phase vortex spatial filter affect the visibility of the correlation fringes, from the degraded fringe patterns we can still extract faithful phase information, since the phase stepping accuracy is not impaired by the presence of moderate aberrations.



## CHAPTER 4

# STRUCTURED ILLUMINATION MICROSCOPY

### Contents

---

<b>4.1</b>	<b>Introduction</b>	<b>100</b>
<b>4.2</b>	<b>Image formation</b>	<b>102</b>
<b>4.3</b>	<b>Reconstruction algorithm</b>	<b>107</b>
4.3.1	Isolation of high frequency information	109
4.3.2	Carrier removal	112
4.3.3	Optical transfer function compensation	116
4.3.4	Algorithm summary	118
<b>4.4</b>	<b>Experimental setup</b>	<b>120</b>
4.4.1	Performance of the microscope	122
<b>4.5</b>	<b>Application</b>	<b>126</b>
4.5.1	Inspection of nanostructures generated by ultrafast laser pulses	127
4.5.2	Real time inspection of nanostructures generated by ultrafast laser pulses	130
<b>4.6</b>	<b>Conclusions</b>	<b>138</b>

---

The structured illumination microscopy (SIM) is a super resolution wide field microscopy technique, which is based on fluorescence and a structured light pattern projected over the sample [40]. The structured illumination generates an extension in the image resolution, because the structures or deformations of high resolution can be seen as a low frequency Moiré fringes. The object can be reconstructed using the information of the Moiré fringes from several images. In this chapter SIM is explained, with the computational algorithm that is necessary for the reconstruction of the super-resolved image. Moreover application of this technique in the examination of nanostructures generated by ultrafast laser pulses is presented.

## 4.1 Introduction

SIM is based on the projection of a sinusoidal pattern over the sample which has to be inspected; using this structured illumination a series of images are taken and then processed using a reconstruction algorithm. However, the idea of structured illumination was used first for optical sectioning in 1997 by M. A. A. Neil and T. Wilson [135]. They projected also a sinusoidal pattern over the sample and recorded a set of three images to block background light and to enhance the contrast of the image by performing sectioning on the  $z$  axis but these images were not over the diffraction limit. It was until Gustaffson in 2005 [40] who took advantage of the Moiré effect produced by the sample and the structured illumination pattern to achieve super resolution images, usually the technique requires at least of nine images to achieve super resolution.

SIM has been used typically to achieve super resolution images (images with subfraction resolution) in amplitude objects that produces fluorescence. Nevertheless, modifications to the original setup allows the use of this technique for other purposes such as measurement of phase objects such as cells [136]; or in combination with no linear effects such as coherent anti-Stokes Raman scattering (CARS)[137].

SIM microscopy uses the effect of Moiré in order to get extra information of the sample that is lost due the diffraction limit associated with the microscope optical response. Moiré effect consists on the visualization of a low frequency fringe pattern. Consequence of the super impose fringe pattern of two high frequency gratings or periodic structures that varies in small angle between them [103], Moiré effect is presented in Fig 4.1. It is observed, From Fig. 4.1a that, if the sample has high frequency information and a structured light pattern (Fig. 4.1b) is projected over the sample, Moiré fringes are presented as low frequency information (Fig. 4.1c) which can be measured computationally.

In order to have a better understanding of this method, the analysis is done in the frequency domain, using the Fourier transform [138]. Traditional microscopy is restricted by diffraction limit, by the optical transfer function (OTF) of the system. The OTF of the microscope can be expressed as

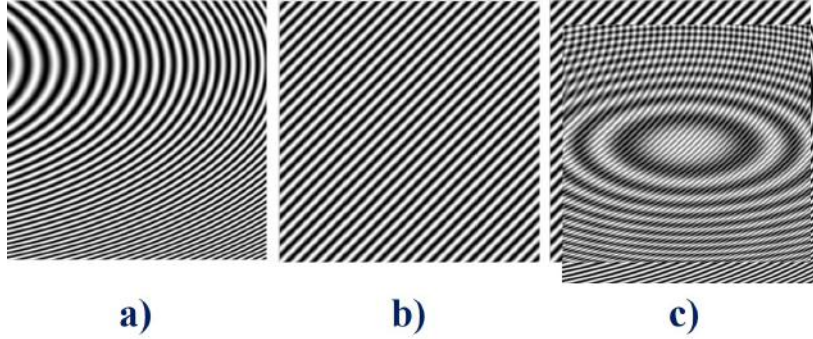


Figure 4.1. Moiré Fringes. a) High frequency information with carrier, b) high frequency structured illumination pattern, c) low frequency Moiré fringes.

$$\begin{aligned}
 H_m(u, v) &= P(x_o, y_o) \otimes P^*(x_o, y_o) \\
 &= \frac{1}{A} \int \int_{\text{Area}} P(x_o - u, y_o - v) P^*(x_o, y_o) dA,
 \end{aligned} \tag{4.1}$$

where  $P(x_o, y_o)$  is the generalized pupil function of the microscope, and the integral has to be done over the pupil area  $A$ .

This transfer function is represented as a blue circle in Fig. 4.2a. High frequency information of the object is neglected by the OTF which acts like a low pass filter with a cut off frequency equal to  $k_o$ . If a sinusoidal pattern is projected to the system, the harmonics of the object in the frequency domain  $\pm 1$  and the background signal are generated, as shown in Fig. 4.2a. In the spatial domain when the object is illuminated with the sinusoidal pattern, it is multiplied by this structured illumination; this can be translated as a convolution operation in the frequency domain as sketched in Fig. 4.2b. If the structured light illumination is projected in different angles, the Fourier spectrum also changes in different angles. This can be seen as an extended OTF with a double resolution as traditional microscopy as seen in Fig. 4.2c. Thus, the reconstruction of the object is done by adding all frequencies from the different directions.

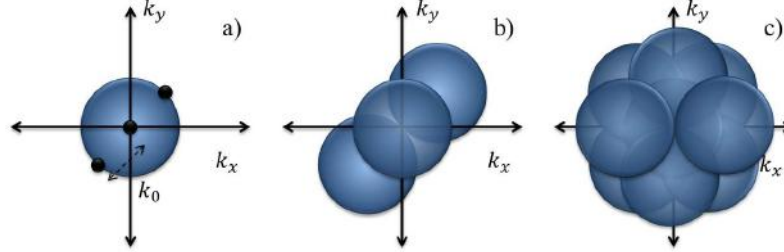


Figure 4.2. SIM analysis in the frequency domain.

## 4.2 Image formation

It is important to analyze the effect of the sinusoidal pattern projected over the sample. The analyzed object  $U_o(x_o, y_o)$  can be represented as shown in Eq. (4.2)

$$U_o(x_o, y_o) = a_o(x_o, y_o) \exp[i\varphi_o(x_o, y_o)], \quad (4.2)$$

where the amplitude  $a_o(x_o, y_o)$  and the phase  $\varphi_o(x_o, y_o)$  varies depending on the object analyzed. Where  $(x_o, y_o)$  corresponds to cartesian coordinates at the object plane. This technique is based on the projection of structured illumination over the sample. The illumination is described by a cosine function as follows

$$S(x_o, y_o) = 1 + \cos(\omega_k \cos \theta_d x_o + \omega_k \sin \theta_d y_o + \phi_0). \quad (4.3)$$

Where  $\omega_k$  is the spatial frequency of the fringes of the illumination and  $\theta_d$  corresponds to the angle of the fringes, the subindex  $d$  is for the multiples directions that the fringes can be positioned; and  $\phi_0$  is the initial phase of the fringes. It is chosen the cosine function for simplicity but a sine function can be used as well. This structured illumination pattern is shown in Fig 4.3, it can be seen it is just a fringe pattern but with a previously known period and controlled angle.

Structured illumination has to be projected over the sample as seen on Fig. 4.4. This can be modeled as a simple multiplication of the fields.

$$S(x_o, y_o)U_o(x_o, y_o), \quad (4.4)$$

in this stage of the process is where the Moiré effects takes place, the high frequency of the sample and the high frequency of the illumination pattern

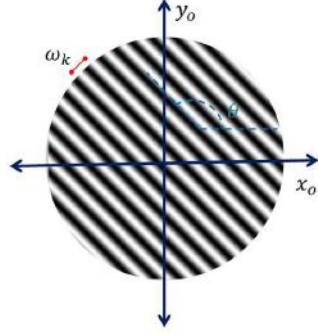


Figure 4.3. Structured illumination.

reveals in a pattern in low frequency which corresponds to information that was not available before.

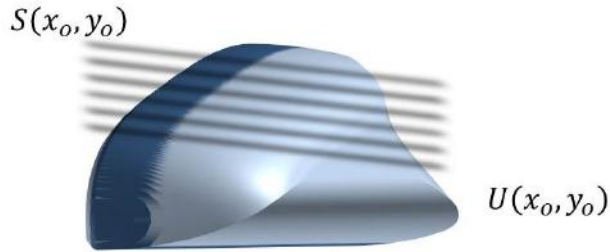


Figure 4.4. Structured illumination projected over a 3D object.

The image through the microscope objective can be modeled as an incoherent two stage imaging system [18]. In this system the image field  $U_i(x_i, y_i)$  is formed as the convolution of the object with the structured light and the point spread function (PSF) of the microscope as seen in Eq. (4.5)

$$U_i(x_i, y_i) = S(x_o, y_o)U_o(x_o, y_o) \otimes h_m(x_o, y_o), \quad (4.5)$$

where  $x_i, y_i$  corresponds to the image plane as seen in Fig. 4.5 and  $h_m(x_o, y_o)$  is the point spread function in the focal plane.

For simplicity the analysis of the image formation is done with the angle of the fringes equal to the  $x_o$  axis so, it is assumed that  $\theta_1 = 0$ . Hence the structured illumination expression becomes only a cosine function of

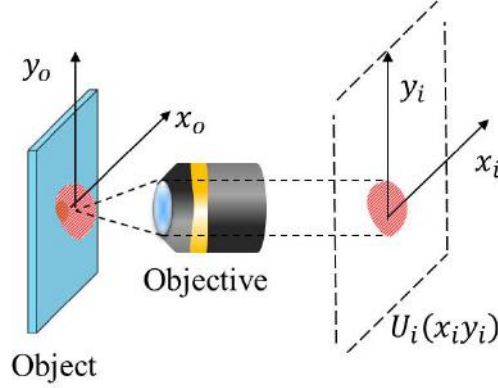


Figure 4.5. Structured illumination projected over the object through the microscope objective.

frequency  $k_o$ . Using those angle parameters and implementing the Euler identity, Eq. (4.5) can be rewritten as follows

$$\begin{aligned}
 U_i(x_i, y_i) &= \frac{1}{2} \{ \exp(i\phi_0 + ix_o\omega_k) U_o(x_o, y_o) \} \otimes h_m(x_o, y_o) \quad (4.6) \\
 &+ \frac{1}{2} \{ \exp(-i\phi_0 - ix_o\omega_k) U_o(x_o, y_o) \} \otimes h_m(x_o, y_o) \\
 &+ U_o(x_o, y_o) \otimes h_m(x_o, y_o).
 \end{aligned}$$

It can be observed that the microscope acts as a low pass filter because of the restrictions impressed by the OTF of the microscope and its resolution limit. In order to analyse the effect of the reconstruction algorithm the intensity distribution should be analyzed on the frequency domain, hence the Fourier transform should be applied to Eq. (4.6).

Thus, applying the Fourier transform to Eq. (4.6) and using shift frequency theorem it is obtained that

$$\begin{aligned}
 U_i(u, v) &= \frac{1}{2} \{ \exp(i\phi_0) U_o(u - \omega_k, v) \} H_m(u, v) \quad (4.7) \\
 &+ \frac{1}{2} \{ \exp(-i\phi_0) U_o(u + \omega_k, v) \} H_m(u, v) \\
 &+ U_o(u, v) H_m(u, v),
 \end{aligned}$$

where  $H_m(u, v)$  is the optical transfer function of the microscope as expressed in the spatial frequency coordinates  $(u, v)$ .



There are three different terms on Eq. (4.7) which are three replicas of the main information. The shifted replicas contained high frequency information, that for traditional microscopy would lie outside the band of the optical transfer function of the microscope. The graphical representation of this equation can be seen in Fig. 4.6, however this figure corresponds to a 3D object where several layers are analyzed in the same time so un focused information also appears.

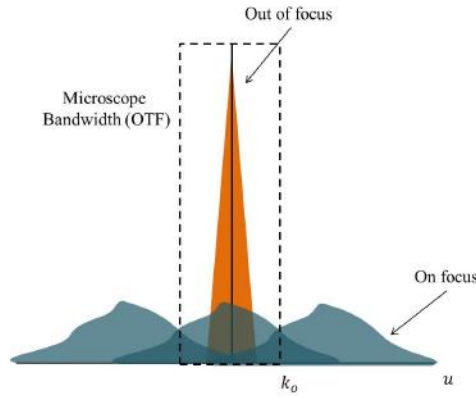


Figure 4.6. Frequency spectrum of a 3D object illuminated with structured light.

From Eq. (4.7) and from the graphical representation in Fig. 4.6. it can be noticed that the bandwidth of the microscope will be the same regardless of the structured illumination. Nonetheless, the spatial frequency of the structured illumination should be almost the same as the cut off frequency of the microscope bandwidth, so it will not be blocked by the bandwidth and the high frequency information can pass through the microscope OTF. So the next condition has to be presented in the structured spatial frequency

$$\omega_k \approx k_0. \quad (4.8)$$

Normally the structured sinusoidal pattern is generated with a physical grid whose parameter is the period of the grid  $T_s$  not the spatial frequency  $\omega_k$ . The period  $T_s$  could be related also with the resolution limit of the microscope, so for the selection criteria of the period of the structured illumination light that will be projected depends on

$$T_s \approx 0.61 \frac{\lambda}{NA}. \quad (4.9)$$

The intensity distribution  $I_n^{(d)}((x_i, y_i)) = |U_{i_n}(x_i, y_i)|^2$  on the CCD, corresponds to the intensity of the field  $U_i(x_i, y_i)$ ,

$$\begin{aligned}
 I_n^{(d)}(x_i, y_i) &= \left| \frac{1}{2} \exp(i\phi_n + \omega_k(\cos\theta_d x_o + \sin\theta_d y_o)) U_o(x_o, y_o) \right. & (4.10) \\
 &\otimes h_m(x_o, y_o) \frac{1}{2} + \exp(-i\phi_n - \omega_k(\cos\theta_d x_o + \sin\theta_d y_o)) U_o(x_o, y_o) \\
 &+ \left. U_o(x_o, y_o) \otimes h_m(x_o, y_o) \right|^2.
 \end{aligned}$$

The subindex  $n$  is introduced to indicate that the phase  $\phi_n$  of the illumination pattern can get  $n$ - values different from  $\phi_0$ , meanwhile the super index ( $d$ ) corresponds to the different angles that the illumination can be positioned.

### 4.3 Reconstruction algorithm

SIM technique is based on the recovery of the high frequency information of the shifted replicas that passes through the OTF of the microscope. In order to do this, the information has to be filtered out by computational methods and then the fourier spectrum of the object has to be reconstructed. The reconstruction algorithm has the following steps to reconstruct a super resolution image of the object.

1. Isolation of high frequency information
2. Carrier remove
3. Compensation of the OTF

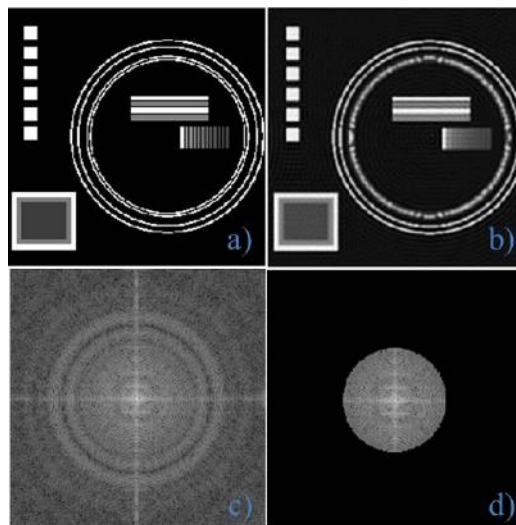


Figure 4.7. Object propagation through the microscope. a)Original object, b)object seen with the microscope, c) frequency spectrum of the original object, d)frequency spectrum of the object seen through the microscope.

To illustrate in a better way the algorithm and the steps numerical simulation was done. Fig. 4.7a illustrate an arbitrary object  $U_o(x_o, y_o)$ , which is propagated through the microscope. The result is seen on Fig. 4.7b. Where the optical signal that passes through the microscope losses information, a blurriness in the image is perceived. As stated on 4.5 the microscope acts like a low pass filter causing this losses of information. The effect is more

obvious when the frequency spectrum of the objects are compared. It can be observed that the original object spectrum shown in Fig. 4.7c has all the high frequency information compared to the one which passed through the microscope Fig. 4.7d.

Structured illumination is projected to the object and propagated through the microscope, as stated by Eq. (4.5). Simulated intensity pattern  $I_1(x_i, y_i)$  is seen in Fig 4.8a. The projected light stands only on vertical axis so  $\theta = 90^\circ$ , it is observed that the Moiré effect takes only place in one part of the object this is because only a direction of the high frequency information passes through the OTF of the microscope as seen in the frequency spectrum in Fig. 4.8b.

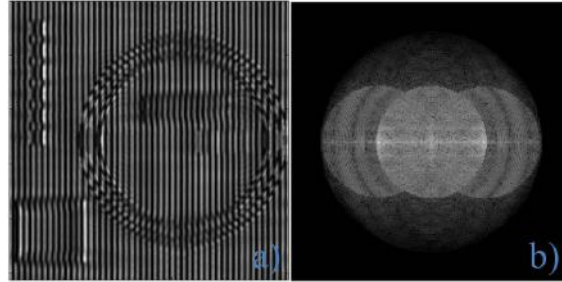


Figure 4.8. Structured illumination projected over an object and propagated through the microscope. a) Intensity distribution  $I_1(x_i, y_i)$ , b) frequency spectrum of the intensity distribution  $I_n(x_i, y_i)$ .

Comparison between the Figs 4.6 and 4.8b can be done; here it is observed that the two information replicas are also in the simulation. These information replicas are called harmonics and they contain high frequency information that is the one translated in the Moiré effect in the spatial domain. As the harmonics are just in one direction the Moiré effect is also just in one direction meaning that super resolution will be obtained just in this direction, which is the reason why the angle theta should vary depending on the increments. In theory only three different increments of  $\theta$  will be enough to reconstruct the object. However the more angles the illumination is projected, the more accurate the retrieved information is.

### 4.3.1 Isolation of high frequency information

The first step of the algorithm is to isolate the high frequency information contained in the harmonics. It is seen from Fig. 4.8b that the background signal or zero order overlaps with the harmonics so an ordinary Fourier filter as proposed by Takeda in 1993 [139] is not useful because the carrier frequency is not enough to separate the information lobes.

Gustafsson approach is to solve a linear set of equation which has the form

$$\begin{pmatrix} \mathcal{I}_0(x, y) \\ \mathcal{I}_+(x, y) \\ \mathcal{I}_-(x, y) \end{pmatrix} = \frac{1}{3} \begin{pmatrix} 1 & 1 & 1 \\ e^{i\phi_1} & e^{i\phi_2} & e^{i\phi_3} \\ e^{-i\phi_1} & e^{-i\phi_2} & e^{-i\phi_3} \end{pmatrix} \begin{pmatrix} I_1(x, y) \\ I_2(x, y) \\ I_3(x, y) \end{pmatrix} \quad (4.11)$$

There are three different terms that can be found using this equation, the first one  $\mathcal{I}_0(x, y)$ , belongs to the background signal of the microscope, it can be seen that is just the average of the input images. The second and third results of solving this linear equation  $\mathcal{I}_+(x, y)$  and  $\mathcal{I}_-(x, y)$  are the high frequency information required for super resolution, which corresponded to the  $\pm$  first harmonic of the signal. It can be seen from Eq. (4.11) that for isolating the high frequency information it is required at least three images with different illumination patterns  $I_1(x, y)$ ,  $I_2(x, y)$ , and  $I_3(x, y)$ . The illumination pattern projected over the sample must have the following phase values  $\phi_1 = 0$ ,  $\phi_2 = \frac{2\pi}{3}$  and  $\phi_3 = \frac{4\pi}{3}$  so the information can be filtered out correctly.

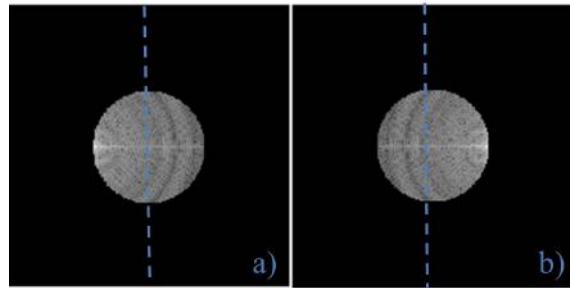


Figure 4.9. Spectrum of the isolated high frequency information a) Right information lobe  $|\mathcal{F}\{\mathcal{I}_+(x, y)\}|$ , b) left information lobe  $|\mathcal{F}\{\mathcal{I}_-(x, y)\}|$ .

If Eq.(4.11) is applied to the simulated object with the respective phase shifts  $\phi_1, \phi_2, \phi_3$ , the high frequency terms of the spectrum can be isolated as

it can be seen in Fig.4.9. It is observed from this figure, that the maximum of the power spectrum is not in the center, this is because there is still the spatial carrier on the image. The operation described in Eq. (4.11) acts like a band pass filter.

In order to understand how this filter works, just one high frequency term from Eq. (4.11) will be analyzed.

$$\mathcal{I}_+(x, y) = I_1(x, y) \exp(-i\phi_1) + I_2(x, y) \exp(-i\phi_2) + I_3(x, y) \exp(-i\phi_3). \quad (4.12)$$

It is observed that this high frequency image information corresponds to an analytical function, meaning that it has a complex part. This analytical function can be obtained by the convolution of an impulse response  $g(x, y)$  and a signal  $I(x, y)$ , evaluated for a time  $t = 2$

$$\begin{aligned} \mathcal{I}_+(x, y) &= I(x, y) \otimes g(x, y)|_{(t=2)} \\ &= [I_1(x, y)\delta(t-2) + I_2(x, y)\delta(t-1) + I_3(x, y)\delta(t)] \\ &\quad \otimes [\delta(t) \exp(-i\phi_1) + \delta(t-1) \exp(-i\phi_2) + \delta(t-2) \exp(-i\phi_3)]_{t=2}, \end{aligned} \quad (4.13)$$

so the impulse response  $g(x, y)$  of the filter is

$$g(x, y) = \delta(t) \exp(-i\phi_1) + \delta(t-1) \exp(-i\phi_2) + \delta(t-2) \exp(-i\phi_3). \quad (4.14)$$

By transforming into the frequency domain respect  $t$  Eq. (4.14), transfer function  $G^3(\omega)$  can be calculated, the super index 3 it is used to emphasis that three images are used in order to filter the information. The value of  $\phi_1 = 0$ , so the transfer function is

$$G^3(\omega) = 1 + \exp(-i[\omega - \phi_2]) + \exp(-i[2\omega - \phi_2]). \quad (4.15)$$

The graph of the magnitude of the filter is sketch on Figure 4.10. So the operation described in Eq. (4.12) is band pass filter which rejects the background signal and the other high frequency order.

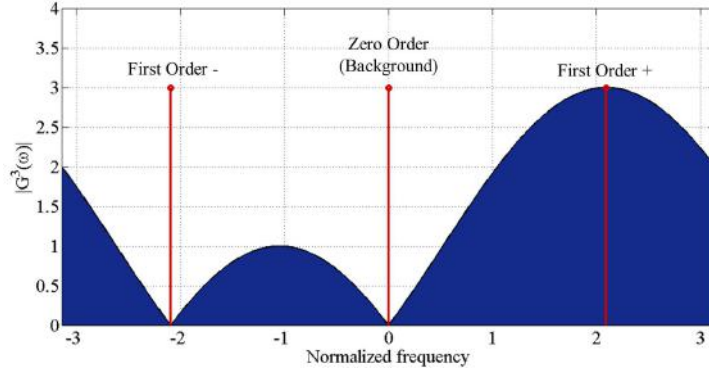


Figure 4.10. Frequency response of  $|G^3(\omega)|^2$ , orders 0,+1 and -1 are sketched in red.

If the filter operation is analyzed in the frequency domain, by performing the Fourier transform to  $\mathcal{I}_+(x, y)$  it can be observed in Eq. (4.16) that the information recovered corresponded to a shifted version of the object multiplied by the optical transfer function of the microscope  $H_m(u, v)$ .

$$\begin{aligned} \mathcal{F}\{\mathcal{I}_+(x, y)\} &= \mathcal{F}\{I(x, y)\}\mathcal{F}\{g(x, y)\} \\ &= U_o(u + \omega_k, v)H_m(u, v). \end{aligned} \quad (4.16)$$

In theory, only three images are needed to perform this operation but in practice there are several factors that affects the accuracy of the filter operation; so more images are needed. This can be easily done by adding more steps to  $\phi_n$ . For instance, a more suitable algorithm for filter the high frequency information is the four step algorithm described by

$$\begin{aligned} \mathcal{I}_+(x, y) &= I_1(x, y) \exp(-i\phi_1) + I_2(x, y) \exp(-i\phi_2) \\ &+ I_3(x, y) \exp(-i\phi_3) + I_4(x, y) \exp(-i\phi_4). \end{aligned} \quad (4.17)$$

It can be seen from Eq. (4.17) that for isolating the high frequency information it is required four images instead of three. The illumination pattern projected over the sample must have the following phase values  $\phi_1 = 0$ ,  $\phi_2 = \frac{\pi}{2}$ ,  $\phi_3 = \pi$  and  $\phi_4 = \frac{3\pi}{2}$ .

More illuminations pattern can be added in order to have a better band pass filter. General algorithm for using  $N$ - illumination patterns is described by

$$\begin{aligned}\mathcal{I}_+(x, y) &= \sum_{n=1}^N I_n(x, y) \exp[i\phi_n] \\ \mathcal{I}_-(x, y) &= \sum_{n=1}^N I_n(x, y) \exp[-i\phi_n],\end{aligned}\quad (4.18)$$

where

$$\phi_n = \frac{2\pi(n-1)}{N}.\quad (4.19)$$

One of the advantages of incrementing the number images used for filtering the high frequency information is the signal noise ratio. Which can be defined as

$$(S/N)|_{\text{out}} = \frac{|G^N(\omega_o)|^2}{1/2\pi \int_{-\pi}^{\pi} |G^N(\omega)|^2},\quad (4.20)$$

Where  $\omega_o = \frac{2\pi}{N}$  corresponds to the normalized cut-off frequency of the filter. From this equation it can be observed that the signal noise ratio  $(S/N)|_{\text{out}}$  increments as the number of images  $N$  also increments, so for noisy images it is better to use more images for performing the filter operation. Also, incrementing the number of illumination patterns allows some other problems such as detuning. [140].

However using more than four images can be counterproductive. A robust algorithm with more illumination patterns required more physical images so more acquisition time and more processing time being translated into a slow algorithm where no further benefits can be obtained, because the highest the degree of the filter is, it rejects more harmonics of the signal, nevertheless as this technique demands working on the resolution limit, no further harmonics of the signal can be obtained.

### 4.3.2 Carrier removal

It can be seen from Fig. 4.9 and Eq. (4.16) that the high frequency information is displaced by the factor  $\omega_k$ . In order to have a super resolution image this displacement caused by inducing a sinusoidal carrier to the object has



to be removed. A sketch of performing this translation can be seen in Fig. 4.11

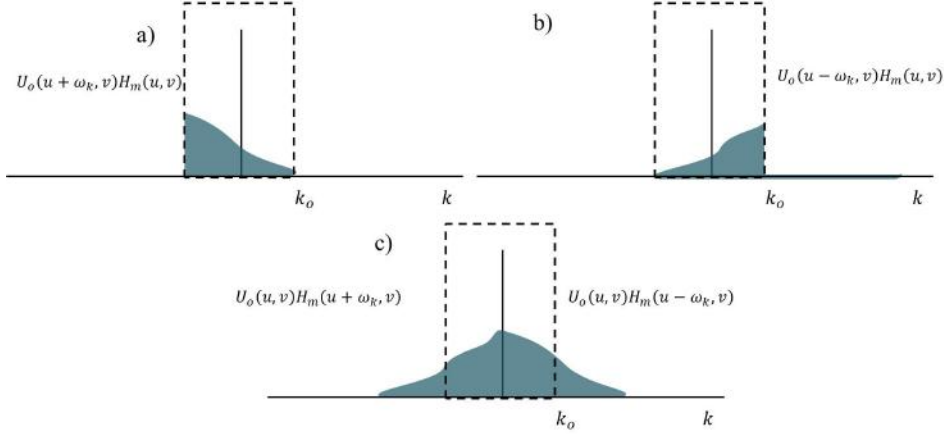


Figure 4.11. Sketch of the spectrum of the isolated high frequency information without carrier. a) Right information lobe  $|\mathcal{F}\{\mathcal{I}_+(x, y)\}|$ , b) left information lobe  $|\mathcal{F}\{\mathcal{I}_-(x, y)\}|$ , c) translation of the high frequency information.

The idea of this step is to remove the carrier from one of the lobes  $\mathcal{I}_+(x, y)$ . This can be done simply by multiplying the high frequency information by an exponential factor and using the translation theorem in the frequency domain. Defining  $\tilde{\mathcal{I}}_+(x, y)$  as the translated version of the high frequency information it can be simply obtained by

$$\begin{aligned}\tilde{\mathcal{I}}_+(x, y) &= \exp[-i\omega_k]\mathcal{I}_+(x, y) \\ \tilde{\mathcal{I}}_-(x, y) &= \exp[i\omega_k]\mathcal{I}_-(x, y),\end{aligned}\tag{4.21}$$

this operation has to be analyzed in the frequency domain by performing the Fourier transform as seen in Eq. (4.22). Here it will be referred to as  $\tilde{\mathcal{I}}_+(u, v) = \mathcal{F}\{\mathcal{I}_+(x, y)\}$  and  $\tilde{\mathcal{I}}_-(u, v) = \mathcal{F}\{\tilde{\mathcal{I}}_-(x, y)\}$  and the same for the left information lobe.

$$\begin{aligned}
\tilde{\mathcal{J}}_+(u, v) &= \mathcal{F}\{\tilde{\mathcal{I}}_+(x, y)\} \\
&= \mathcal{J}_+(u - \omega_k, v) \\
&= U_o(u, v)H_m(u - \omega_k, v).
\end{aligned} \tag{4.22}$$

A shifted version of the OTF of the microscope appears due the remove of the carrier, this can be seen in Eq. (4.22), if both shifted high frequency information are added an extended version of the OTF of the microscope  $H_e(u, v)$  is obtained,

$$\begin{aligned}
\tilde{\mathcal{J}}_+(u, v) + \tilde{\mathcal{J}}_-(u, v) &= U_o(u, v)H_m(u - \omega_k, v) \\
&+ U_o(u, v)H_m(u + \omega_k, v) \\
&= U_o(u, v) [H_m(u - \omega_k, v) + H_m(u + \omega_k, v)] \\
&= U_o(u, v)H_e(u, v),
\end{aligned} \tag{4.23}$$

where the extended OTF  $H_e(u, v)$  has a cut off frequency that depends on  $\omega_k$ , as seen in Eq. (4.8), this cut off frequency is related with the diffraction limit so if the condition established on Eq. (4.8) is respected the system will have an OTF cut off frequency the double as before, leading to super resolution images.

#### 4.3.2.1 Computing algorithm

If the operation of multiplying the filtered image by the exponential solves the problem of shifting the information to the right position, in practice it is not as easy as the illumination pattern changes. The misplaced of the information lobe leads to image distortion and affects the resolution of the image. In order to avoid that problem, an alternative method can be explored.

The algorithm is based on finding the position of the principal peak in  $|\mathcal{J}_+(u, v)|$  and then translating this peak to a defined position (the center of the image). That way all the high frequency information is placed on the same position avoiding mismatching errors.

The method described by Huntley in 1986 [141] provides good stability for experimental and noisy images as it was designed for speckled interferograms. The algorithm is used for computing the principal peak position of

an image whose Fourier transform has the same form as  $\mathfrak{J}_+(u, v)$ . The idea is just to use the Newton-Raphson method in order to find the coordinates  $(u_1, v_1)$  such that

$$\begin{aligned} \frac{\partial}{\partial u} |\mathfrak{J}_+(u, v)|^2 \Big|_{u=u_1} &= 0 \\ \frac{\partial}{\partial v} |\mathfrak{J}_+(u, v)|^2 \Big|_{v=v_1} &= 0. \end{aligned} \quad (4.24)$$

Once the coordinates of the main lobe are founded the translation can be done. It is important to notice that this method works regardless the position of the peak, so it is useful once the rotation of the grid is done. The generalized equation that describes this displacement is

$$\begin{aligned} \tilde{\mathfrak{J}}_+(u, v) &= \mathcal{F}\{\tilde{\mathcal{L}}_+(x, y)\} \\ &= \mathfrak{J}_+(u - \omega_{k_x}, v - \omega_{k_y}) \\ &= U_o(u, v)H_m(u - \omega_{k_x}, v - \omega_{k_y}), \end{aligned} \quad (4.25)$$

where  $\omega_{k_x} = u_1$  and  $\omega_{k_y} = v_1$ . The same proceeding can be done on the left information lobe. If this algorithm is applied to the simulation images, the result can be appreciated on Fig. 4.12

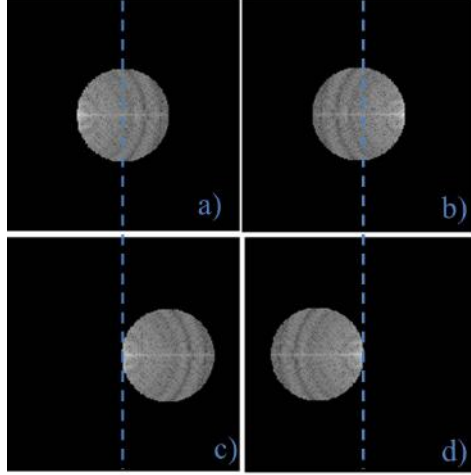


Figure 4.12. Simulation of the spectrum of the isolated high frequency information without carrier. a) Right information lobe  $|\mathfrak{J}_+(u, v)|$ , b) left information lobe  $|\mathfrak{J}_-(u, v)|$ , c) translation of the high frequency information  $|\tilde{\mathfrak{J}}_+(u, v)|$ , d) translation of the high frequency information  $|\tilde{\mathfrak{J}}_-(u, v)|$ .

### 4.3.3 Optical transfer function compensation

Subsequently the high information is recovered and placed on the center of the image, this information has super resolution information. However, the spectrum  $\mathfrak{J}_+(u, v)$  is still filtered by the OTF of the microscope. So a deconvolution operation has to be done. This can be appreciated in Eq. (4.25), where the OTF  $H_m(u - \omega_{k_x}, v - \omega_{k_y})$  is part of the information. This OTF can be removed by a modified Wiener filter [142]. The filter can be performed by

$$D_+(u, v) = \frac{\tilde{\mathfrak{J}}_+(u, v) H_m^*(u - \omega_{k_x}, v - \omega_{k_y})}{w^2 + |H_m(u - \omega_{k_x}, v - \omega_{k_y})|^2}, \quad (4.26)$$

where  $H_m^*(u - \omega_{k_x}, v - \omega_{k_y})$  is the complex conjugate of the microscope OTF and  $w$  is a weight constant of the filter to avoid division by zero, usually is one but it can be determinate by practical inference [143].

Finally the super resolution image in one direction ( $d$ ) can be found by adding the filtered data and performing a inverse Fourier transform.

$$I s_d(x, y) = \mathcal{F}^{-1} \{D_+(u, v) + D_-(u, v)\}. \quad (4.27)$$

Eq. (4.27) gives super resolution image just in one direction. Thus the angle of the illumination has to be modified in order to scan all the frequencies. So, the angle  $\theta$  on Eq. (4.3) has to be changed, usually it is only needed three rotation of the angle ( $\theta_1 = 0, \theta_2 = 60^\circ, \theta_3 = 120^\circ$ ) However in practice the more angles the illumination is projected, the reconstruction of the super resolution image is more precise and artifacts are avoided, this in practice five orientations are recommended.

The final super resolution image can be found by

$$I s(x, y) = \sum_{d=1}^{\mathcal{D}} I s_d(x, y). \quad (4.28)$$

The index  $d$  is for the different angles that the grid is projected. The angles should have the condition

$$\sum_{d=1}^{\mathcal{D}} \theta_d = 180^\circ. \quad (4.29)$$

The index  $\mathcal{D}$  correspond to the maximum number of rotation that are performed during the experiment. For instance if the grid is rotated five times then  $\mathcal{D} = 5$ . If Eq. (4.28) is applied to the simulation example the result can be seen in Fig 4.13. It can be observed that the high frequency information that was recovered is translated in the details of the image that were lost due the microscope diffraction limit.

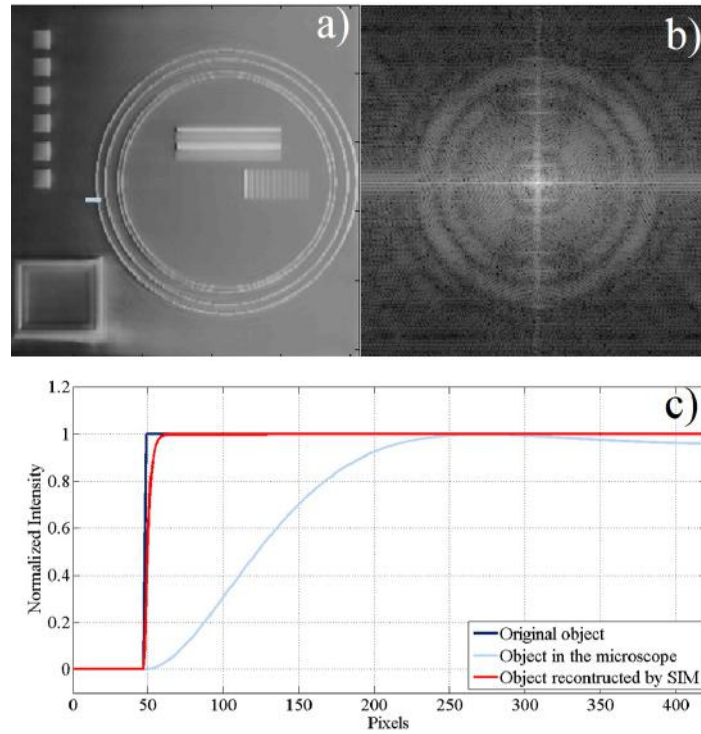


Figure 4.13. Simulated super resolution image. a) Super resolution image  $I_s(x, y)$ , b) reconstructed frequency spectrum, c) transversal cut section comparison between original object, object under the microscope and SIM reconstruction.

#### 4.3.4 Algorithm summary

Towards the right understanding on SIM technique, a brief summary of the algorithm for obtaining super resolution images is presented. The general algorithm can be divided in two parts:

1. Capture Algorithm Fig. 4.14a
2. Reconstruction Algorithm Fig. 4.14b

It can be seen from the capture algorithm (Fig. 4.14a) that are necessary  $N \times \mathcal{D}$  images so the reconstruction can be done. The minimum images that are required are nine, using three translations and three rotations. However in practice it is helpful to use at least 20 images, meaning four translations

and five rotations. These numbers can be adjusted depending on the noise generated by the image and the precision the rotation and translation are done.

The reconstruction algorithm presented on Fig. 4.14b is described in detail by the previous sections, but it is necessary to understand that previous treatment should be done before the super resolution reconstruction algorithm is done. As in all the experimental images, the noise has to be removed by a low pass filter; but this filter should not affect the fringes of the taken patterns, regularization filters can be implemented [130]. Also borders of the images should be removed and the histograms of the images should be equalized for an optimal performance as in interference pattern analysis [144].

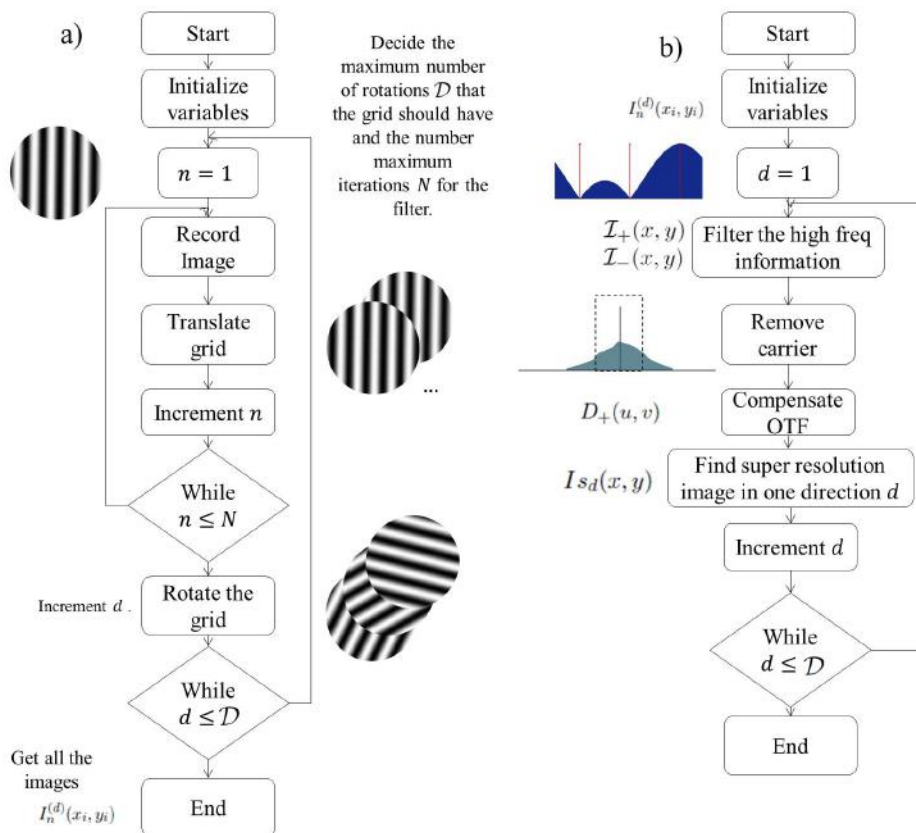


Figure 4.14. Diagram block of the algorithm for SIM. a) Capture algorithm, b) reconstruction algorithm.

## 4.4 Experimental setup

The experimental setup is shown in Fig. 4.15. An ultraviolet LED source  $S$  was used for the setup with a central wavelength of 405 nm and a bandwidth of 13 nm, the light was filtered by a diffuser and collimated by  $L_0$  and  $L_1$ , in order to achieve an uniform incoherent illumination based on the epi-illumination system. In the illumination path, an amplitude grid  $G$  was placed. The analyzed samples are specular samples, so the structured illumination light projection has to be done with an amplitude grid otherwise, as there are no fluorophores, there would be no structured illumination projected over the sample. The grid corresponds to a Ronchi grid with a period of 120 lines per millimeter. The grid is mounted over a rotation and a translation stage, this way its position and rotation of the grid can be changed for the spectral domain recovery stage. The grid has to be placed just in the focal plane of lens  $L_2$ , so it can be projected just in the back focal plane of the microscope objective  $MO$  using a beam splitter. The amplification of the grid is related between the focal distance of the microscope objective and lens  $L_2$ .

For this setup the microscope objective that was used was a corrected infinity 100x plano-achromatic Olympus objective with a  $NA = 0.9$ . The back focal plane of the objective is 1.8 mm. Using these parameters the resolution limit for this configuration is 275.5 nm.

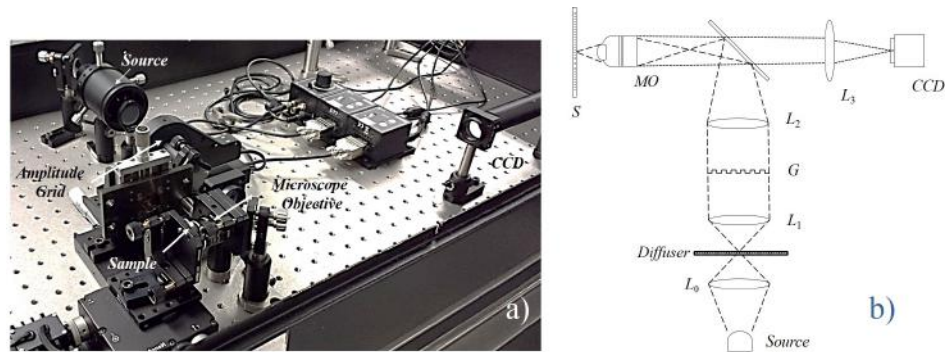


Figure 4.15. Experimental setup for SIM microscopy.

The amplification for the grid over the sample should be of  $1/30$ , this amplification is the ratio between the resolution limit and the period of the grid. The amplification can be controlled by the focal distance of lens  $L_2$ . The focal distance of the microscope objective is 1.8 mm, so the focal distance



of the lens  $L_2$  should be 54 mm. Nevertheless, for simplicity a 50 mm lens was used; the magnification of the grid over the sample is 0.036. With these parameters the fringes will be projected with a separation of 300 nm. Meaning that, the minimum theoretical resolution that can be achieved using this configuration will be of 150 nm.

Finally, the infinity corrected microscope objective needs a lens ( $L_3$ ) so the image over the CCD can be formed, the focal lens of  $L_3$  was chosen in order to have a total magnification of 100. To do this, the optical tube lens was calculated using a 200 mm focal lens for projection.

Once the optical setup was constructed some parameters had to be defined in order to make the super resolution algorithm previously described in section 4.3.2.1 worked out along with the optical setup previous described. The maximum number of rotations  $\mathcal{D}$  were five, so for this setup  $\mathcal{D} = 5$ . The angles used experimentally were  $\theta_1 = 90^\circ$ ,  $\theta_2 = 54^\circ$ ,  $\theta_3 = 18^\circ$ ,  $\theta_4 = 342^\circ$ , and  $\theta_5 = 306^\circ$ . The step between the angles is  $36^\circ$  and the initial angle  $\theta_1 = 90^\circ$  was vertical so it was easier the measurement and calibration of the other projected illumination patterns.

This illumination patterns with different angles can be seen in Fig. 4.16. Where Moiré effect is presented just in some directions; the analyzed sample is a stainless steel plate. For each rotation four displacements were done, so the maximum number of translations  $N$  for this setup corresponded to  $N = 4$ . Each translation corresponded to a phase displacement of  $\phi_n = \frac{2\pi(n-1)}{4}$  and a physical translation of  $25 \mu\text{m}$ . For recovering one super resolution image 20 images were needed. The synchronization between the rotation and the translation of the Thorlabs stages and the camera was done using LabView software.

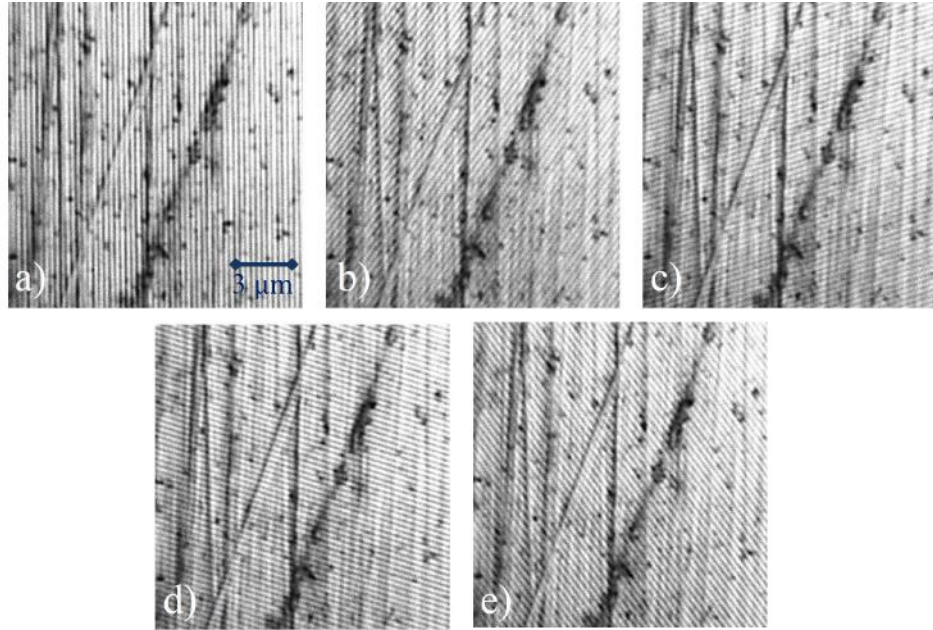


Figure 4.16. Experimental illumination patterns projected over a stainless steel sample. a)  $\theta_1 = 90^\circ$ , b)  $\theta_2 = 54^\circ$ , c)  $\theta_3 = 18^\circ$ , d)  $\theta_4 = 342^\circ$ , and e)  $\theta_5 = 306^\circ$ .

#### 4.4.1 Performance of the microscope

The performance of the microscope has to be analyzed, meaning that it has to be proved that super resolution is achieved through the algorithm and the experimental setup. First of all, the constructed microscope has an amplification of 100 X; it was measured using the pixel size of the camera ( $4.65\mu\text{m} \times 4.65\mu\text{m}$ ) and a Thorlabs air test grid. Thus the field of view of the microscope is  $45.6 \mu\text{m} \times 34.23 \mu\text{m}$ .

The point spread function of the microscope provides a good idea concerning the performance of the whole system in terms of resolution. The evaluation of the PSF has to be done by using a Dirac delta as the analyzed object and observe the formed image in the CCD. Usually fluorescent microspheres are placed as objects with in the resolution limit [19]. For the measurement of the PSF a flat silicon wafer was used as seen in Fig 4.17a. As the constructed microscope is designed for specular images with no fluorescence the analyzed object corresponded to an ablation spot generated with the femto second

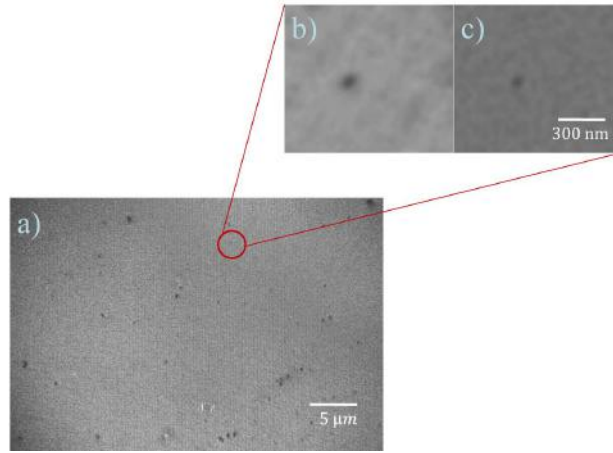


Figure 4.17. Evaluation of the point spread function of the microscope. a) Image of a flat surface for the PSF analysis, b) zoom of the image seen by the normal microscope, c) zoom of the image seen by the super resolution microscope.

laser, this spot can be seen in the red circle on Fig 4.17a.

The comparison of the analyzed spot can be seen in Fig 4.17 b) and c). Image presented on Fig 4.17b corresponds to the image without the super resolution algorithm and removing the grid of the setup. Meanwhile Fig. 4.17c is the super resolution image of the analyzed spot. A better idea of the point spread function can be seen if a transversal cut is done to the previous images. The graph presented in Fig 4.18 presents the profiles of the PSFs.

By comparing the point spread function it can be seen clearly a reduction of the main lobe, so the cut off frequency of the microscope is higher for super resolution technique. The full width at half maximum (FWHM) of the PSFs can be compared to make an objective comparison and analyze the minimum object that can be analyzed with this constructed microscope. So it can be obtained from the graph in Fig. 4.18.

$$\text{FWHM}_n = 0.315 \mu\text{m}$$

$$\text{FWHM}_s = 0.170 \mu\text{m}$$

Where  $\text{FWHM}_n$  stands for the full width at half maximum of the normal

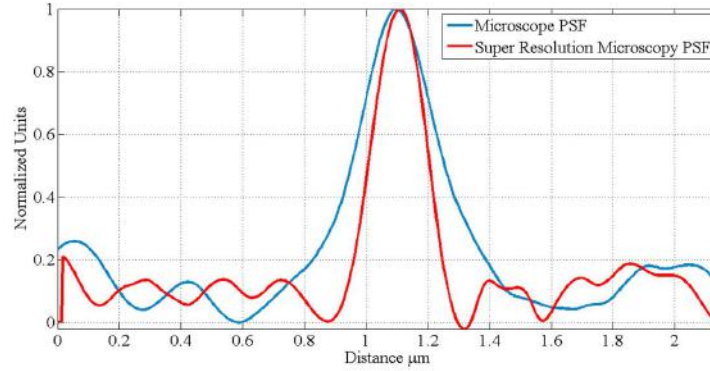


Figure 4.18. Experimental measurement of the point spread function of the microscope.

microscope without modifications and  $\text{FWHM}_s$  corresponds to the FWHM of the microscope with SIM. The ratio between this data gives the reduction of the PSF and numerical comparison of the methods can be evaluated .

$$\frac{\text{FWHM}_s}{\text{FWHM}_n} = 54\%$$

The reduction of the point spread functions is 54% in theory the super resolution achieved should be 50%, in this case is desired that the percentage is lower in order to get a better resolution in the image. Meaning that in optimal circumstances the microscope should achieve double of resolution as a typical microscope. Nevertheless in practice it is obtained a 4% error; this error is due to the amplification of the projection lens, which focus length was rounded for convenience. However using this experimental data, the microscope resolution is 155 nm. instead of the 150 nm expected by theory.

For analyzing the performance on specular surface and have a better idea of the limits of the technique, it was used an air grid test from Thorlabs to inspect the resolution of the microscope. The air grid was a metallic thin film deposited over glass, where the edge of the film was analyzed on the microscope. Fig. 4.19 shows the comparison of the obtained images. Fig. 4.19a corresponds to the analyzed object without modifications to a normal microscope; meanwhile Fig. 4.19b corresponds to the super resolution setup. A vertical cut of the edge can be appreciated on Fig. 4.19c, where the edge is clearer in the super resolution image, the sharpest the edge of the thin film is measured the best is the resolution of the microscope.

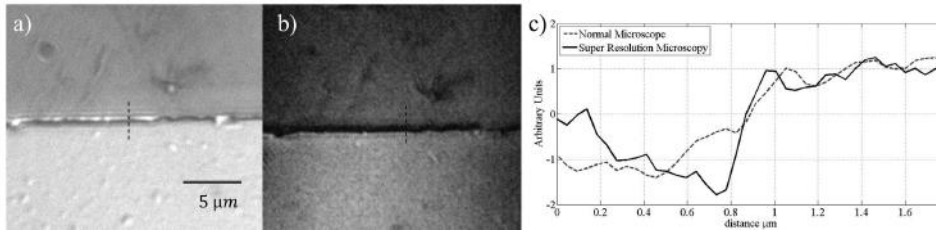


Figure 4.19. Analysis of a test grid. a) Normal microscope, b) super resolution microscope, c) comparison of the profile of the images a) and b).

Analyzing the resolution limit of the microscope and proving that the technique is suitable for analysis on specular objects which are beyond traditional resolution limit, there are different applications for this super resolution microscope technique.

## 4.5 Application

Ultrafast laser manufacturing has been taking importance over the years because of their different applications. For instance, the processing enables the generation of specific nano scales periodic organizations in the material. This nano structures are typically spaced by

$$d_r = \frac{\lambda}{2n}, \quad (4.30)$$

where it can be observed that the space  $d_r$  between the nano structures are subwavelength structures which depend on the material refraction index  $n$  [145].

The characteristics of the nanostructures depend on the different parameters of the laser pulse used to create the nano structures. For instance, the laser polarization can change the direction of the structures [146], meanwhile the periodicity of the nano structures and arrangement depends on the pulse form of the laser [147]. Nanostructures formed by ultrafast laser can be used to modify the optical functionality of the material, giving properties such as polarization guiding or phase retardation [148, 149] to the material that were not presented before.

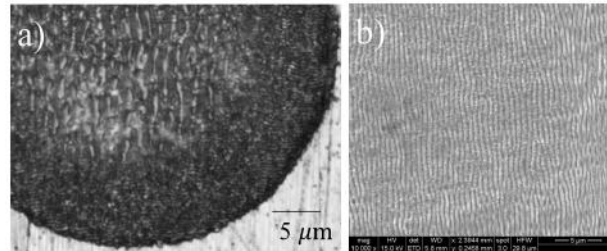


Figure 4.20. Inspected nanostructures generated by the ultrafast pulse laser. a) Impact analyzed using an optical microscope, b) nanostructures analyzed using an SEM.

These nanostructures can not be easily inspected using traditional microscopy because they are beyond the diffraction limit as it can be seen in Fig. 4.20. If Scanning Electron Microscopy (SEM) or Atomic Force Microscopy (AFM) enable fine topological measurements of these structures on surfaces, these techniques can't be applied in real time nor for bulk modification. Thus, there is a need for an optical detection set up with a resolution below the

diffraction limit, so SIM technique provides the elements in order to analyze this nanostructures.

#### 4.5.1 Inspection of nanostructures generated by ultrafast laser pulses

Nanostructures generated by ultrashort pulses have several characteristics that have to be analyzed such as the orientation, the size, the period and secondary structures formed. These parameters allow that the structures formed could be used in different applications depending on the functionalization that is applied.

Fig. 4.21 shows the nanostructures generated by ultrashort infrared (800 nm) light pulses from a regenerative amplified Ti: sapphire ultrafast laser system delivering 50 mW of usable power at a repetition rate of 100 kHz and nominal output pulse duration of 130 fs. The sample used in Fig. 4.21 was a stainless steel plate, ablated by 15 pulses.

It can be observed in Fig. 4.21a the image obtained by a classical optical microscope, some structures can be observed due the diffraction limit of the setup. However using the super resolution SIM constructed setup a super resolution image of the nanostructures is computed as it can be seen in Fig. 4.21b.

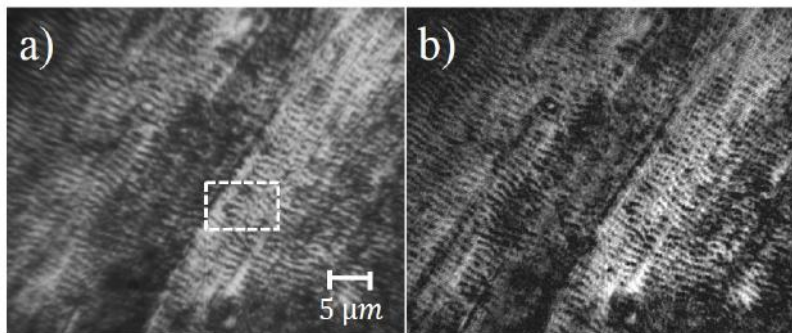


Figure 4.21. Inspected nanostructures generated by the ultrafast pulse laser over stainless steel. a) Impact analyzed using an optical microscope, b) nanostructures analyzed using SIM.

The comparison between the two images is more evident if a section on Fig. 4.21 is compared as seen in Fig. 4.22. Where it is clear in the image com-

puted with SIM, Fig. 4.22b, that some structure properties that were not able to distinguish in traditional microscopy can be analyzed and inspected giving more information of the nanostructures that were not evident before. It can be seen that smaller secondary structures perpendicular to the bigger structures appears. This nanostructures couldn't be appreciated in traditional microscopy.

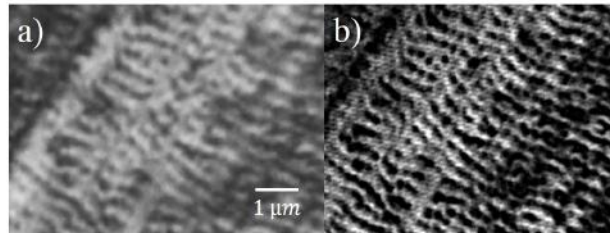


Figure 4.22. Zoom over the selected area in Figure 4.22. a) Impact analyzed using an optical microscope, b) nanostructures analyzed using SIM.

SIM technique uses structured illumination, so besides super resolution images also optical sectioning could be achieved [135]. Hence, this technique is not suitable when an object that requires focal depth analysis. For instance, sometimes ripples or nanostructures are formed using a big amount of energy as, (over 50 mW per pulse) it can be seen in Fig. 4.23. Here an impact over stainless steel is seen, the impact was done using the same laser characteristics than before but using 50 mW and 20 pulses. The depth of the ablation spot is around 3  $\mu\text{m}$ , so some areas of the image are out of focus as it can be observed in Fig. 4.23. Where the microscope is on focus the ripples can be well analyzed however in the area that was out of focus due the depth of the sample the technique doesn't provides reliable information.

However when the nanostructures are created just in the surface of the impact the technique provides an improvement for the quantification of certain parameters. For instance in Fig. 4.24 the nanostructures are also created over a stainless steel surface caused by the femto second laser with the same characteristics of wavelength and pulse duration as the others. It can be seen that the computed image in Fig. 4.24b which corresponds to the SIM technique, gives more reliable information for getting the period and position of the ripples.

As the resolution is almost as twice as the traditional microscopy the edges of the ripples are improve as well as little details that were not available before. A transversal cross section of the image is plotted in Fig. 4.25, it



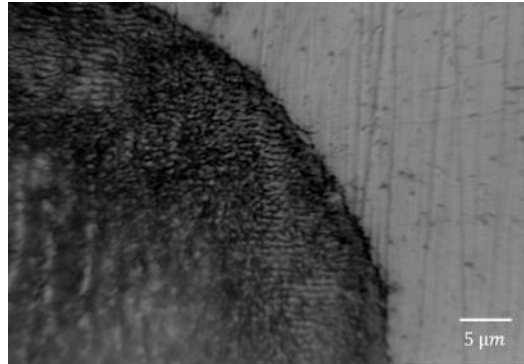


Figure 4.23. Analyzed impact of a femtosecond laser using SIM.

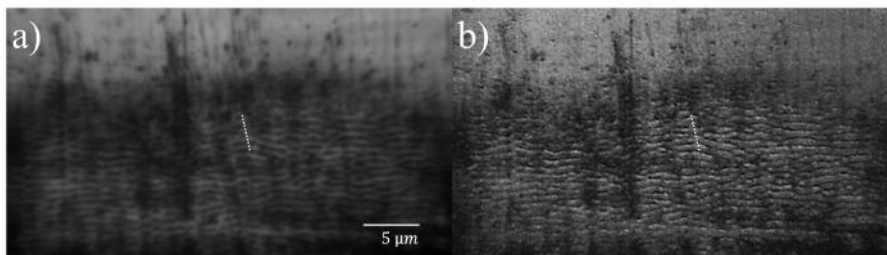


Figure 4.24. Inspected nanostructures generated by the ultrafast pulse laser over stainless steel before ablation. a) Impact analyzed using an optical microscope, b) nanostructures analyzed using an SIM.

can be seen that the period of the structure is  $0.5 \mu\text{m}$  and some details appear that were cut off by the OTF of the traditional microscope.

Also in order to decrease the speckle caused by the coherence of the UV lamp of the microscope white light can be used in the setup, results are similar as using the UV lamp however more image treatment has to be done as histogram equalizing and noise reduction because the contrast of the fringes is lower, so the reconstruction technique has to be optimized. Results using this technique over a silica sample can be seen in Fig. 4.26. It can be seen that also super resolution is achieved but with a smaller cut off frequency so the optimal illumination corresponds to the UV illumination.

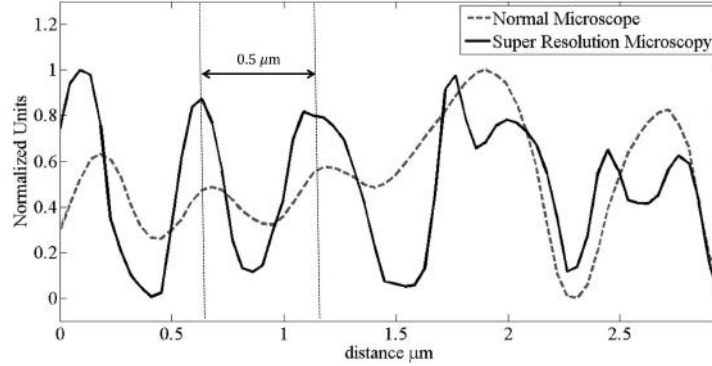


Figure 4.25. Comparison of the microscopy techniques by a transversal cut of the sample images shown in Fig. 4.24.

#### 4.5.2 Real time inspection of nanostructures generated by ultrafast laser pulses

It has been shown that SIM technique can be applied in the analysis of nanostructures generated by femto-second lasers. Using this technique some details can be observed that with a traditional optical microscope are not easily visible; this makes possible the characterization of the nanostructures more accurate. The main advantage of SIM microscopy is that the optical setup can be applied to analyze the formation of the nanostructures in real time by modifying the optical setup. Even though that AFM or SEM provides better results are not suitable to get results in real time.

The optical setup can be seen in Fig. 4.27. It can be observed that the optical setup from the microscope stays as in the previous section, so the microscope was not modified. However, here the femto second laser ( $\lambda = 800$  nm) which comes from a regenerative amplified Ti: sapphire with a repetition rate of 1 kHz and nominal output pulse duration of 50 fs is focused over the sample using a positive lens  $L_4$ , with a focal distance of 10 cm. The beam is focused on the sample using some thin film mirrors  $M_1$ .

From the schematic presented in Fig. 4.28 it can be observed that the femto second laser beam arrives with an incident angle  $\alpha$  different from the perpendicular axis of the microscope. So the Gaussian beam is a projection of the perpendicular beam which depends on the angle  $\alpha$ . The angle of incidence of the beam is  $78^\circ$  as it can be seen in Fig. 4.28b.

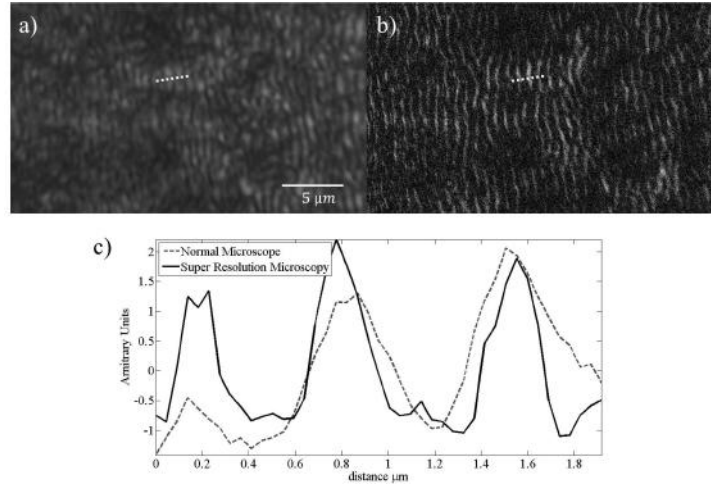


Figure 4.26. Inspection of nanostructures using white light. a) Impact analyzed using an optical microscope, b) nanostructures analyzed using an SIM, c) comparison of the microscopy techniques by a transversal cut of the sample.

For this configuration the minimum spot focus on the sample has a waist  $\omega_{oy} = 10\mu\text{m}$  in the  $y$  direction and  $\omega_{ox} = 50\mu\text{m}$  in the  $x$  direction as it can be appreciated on Fig. 4.28a. This was calculated using the 10 cm lens. So the fluence of the laser will be dissipated over an elliptical region, so two maximum fluence will be calculated, one in the  $x$  direction and one for the  $y$  direction,  $F_x$  and  $F_y$ , respectively.

To see the evolution of the ripples in real time, different materials were evaluated as well as different power for the laser intensity. Table 4.1 explains the materials and the different powers that were used in the experiments. The power from the laser irradiated over the different materials for each test, were based on a test matrix where the power and number of pulses were incremented until the nanostructures were created in the material. So the number of pulses varies depending on the material even though the same power was irradiated over the material.

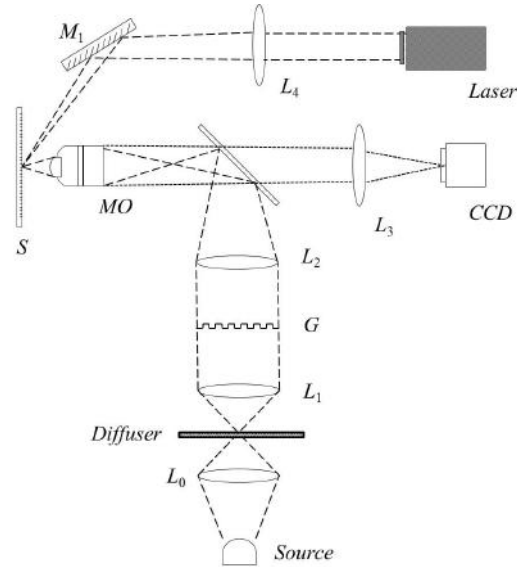


Figure 4.27. Experimental Setup for inspection of nanostructures in real time.

Table 4.1. Samples analyzed.

<b>Material</b>	$P_1$	$P_2$	$P_3$
Stainless Steel	3 mW	8 mW	10 mW
Silica type n	5 mW	10 mW	-
Metallic Glass	10 mW	15 mW	-

On the next section the discussion over the stainless steel sample is presented but only for laser powers of 3 mW and 8 mW average. Here are presented two regimes, one with low fluence over the sample (with a maximum power from the laser of 3 mW), and the other with high fluence over the sample.

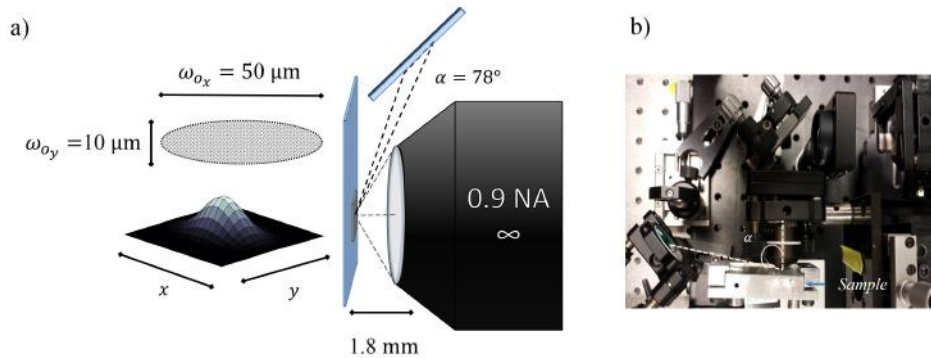


Figure 4.28. Schematic of the ultrafast laser beam focused on the sample for real time inspection of the nanostructures. a) Size of the minimum spot focus on the sample, b) experimental setup.

#### 4.5.2.1 Stainless steel

In order to see the evolution of laser-induced periodic surface structures (LIPSS) in-situ over stainless steel, experimental setup shown in Fig. 4.28a was used. At first, the sample was irradiated with 3 mW average power from the ultrashort laser. As the laser arrives with an angle  $\alpha$  as stated before, there are two different fluence, one in the  $x$  direction and one in the  $y$  direction, the maximum fluence is on  $x$  direction, being the average fluence on this direction  $F_x = 0.18 \text{ J/cm}^2$ .

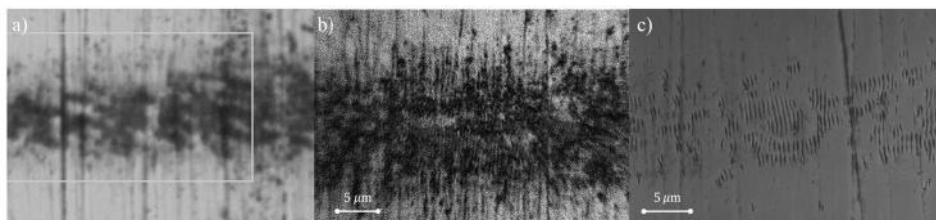


Figure 4.29. LIPSS over stainless steel sample after 72 pulses. a) Sample seen through a traditional microscope, b) sample seen through SIM, c) sample seen through a SEM.

It can be seen on Fig. 4.29 the importance of using a super resolution technique to see the development of LIPSS. Fig. 4.29a shows the stainless steel sample treated after 72 pulses on a regular Zeiss microscope; where no

nanostructures can be observed due the resolution limit of the microscope. However using SIM technique with no fluorophores LIPSS can be seen as shown on Fig. 4.29b. The same area is observed over an SEM, even though the resolution is better as seen on Fig. 4.29c, the evolution in time of the structures can not be determined.

Optical setup on Fig. 4.27a allows the inspection of the surface after shooting one single pulse and see how the material responds to the interaction of the laser. On the stainless steel sample 50 pulses were shot over the sample so LIPSS were induced over the surface. After doing this, one single pulse was shot over the sample and then a super resolution image was computed, completing a total of 72 pulses over the stainless steel sample. The result can be analyzed on Fig. 4.30. Where it can be seen that the sample suffers from an erosion effect while the pulses interacts with the surface, having a deterioration of the material. This deterioration makes the ripples more defined over the surface, causing an enlargement which is dependent of the number of pulses.

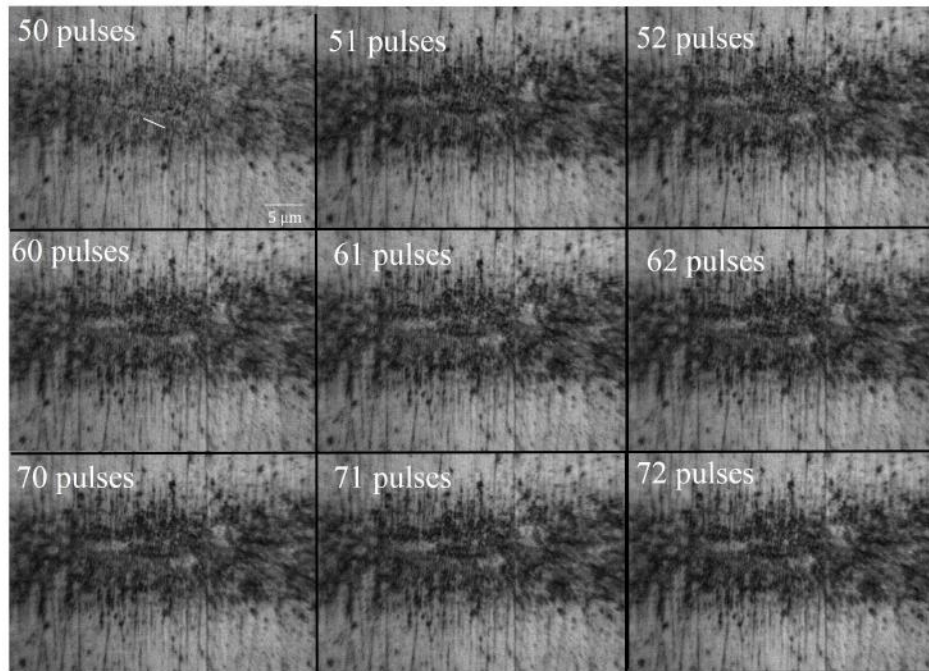


Figure 4.30. Evolution in time of LIPSS on a stainless steel sample with low fluence.

The effect of sharpness evolution over the LIPSS can be seen with more detail if a transversal cut is done over the images. This can be observed on Fig. 4.31 where it can be noticed that the central peak of each nanostructure is preserved, meaning that there is no phase change on the structure just a degradation effect is presented under a low fluence regime.

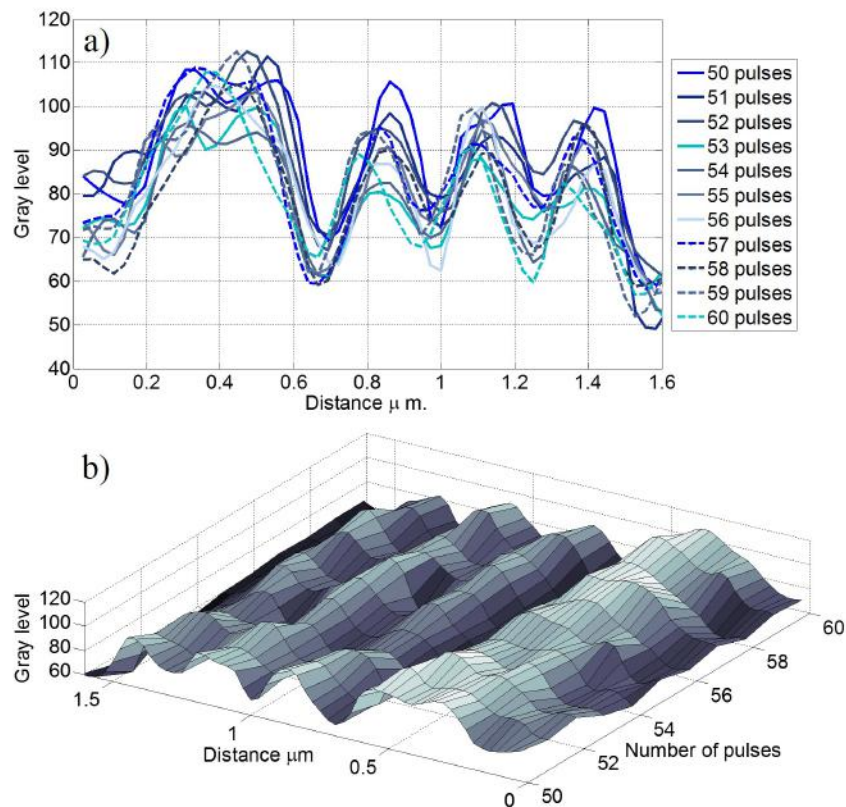


Figure 4.31. Transversal cut for analyze the time evolution of LIPSS on a stainless steel sample with low fluence. a) Comparison graph of the 21 profile of LIPSS over stainless steel low fluence regime, b) time evolution of the structures on stainless steel at low fluence.

The periodic structures remain almost the same as it can be seen on Fig. 4.31b where the nanostructures get more defined as the number of pulses increment over the sample. This is shown as the contrast between the structures and the maximum increases over the pulses, moreover a steady state on the structures is well defined.

After the low fluence regime was analyzed the average laser power was increased to 8 mW, so an average of  $F_x = 0.24 \text{ J/cm}^2$  irradiated the sample.

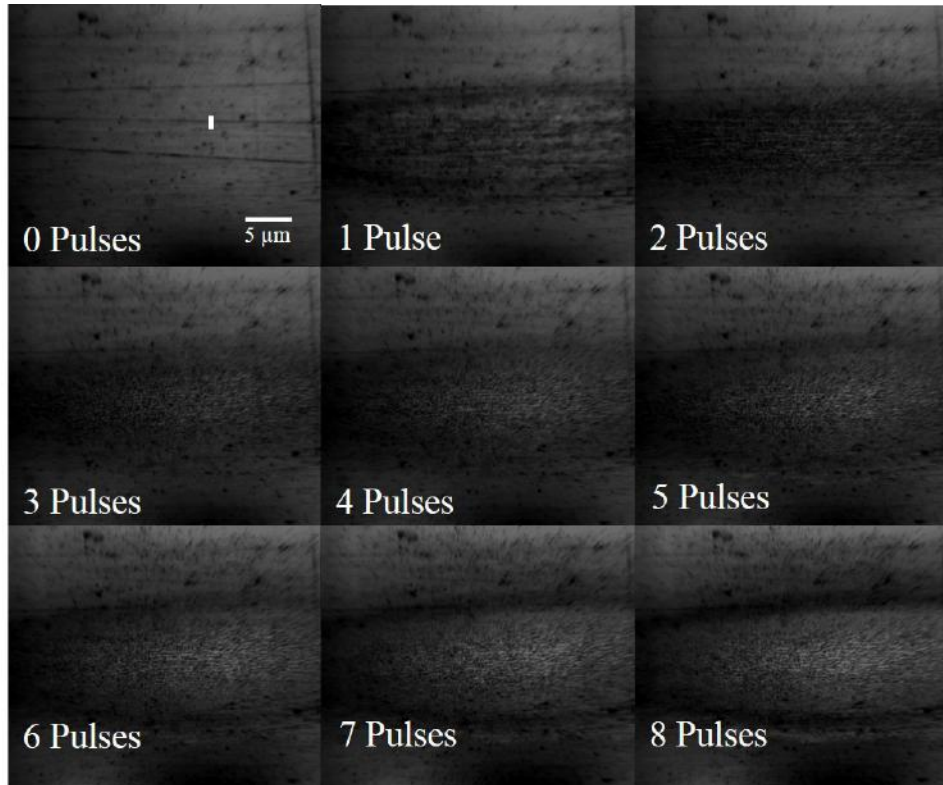


Figure 4.32. Evolution in time of LIPSS on a stainless steel sample with high fluence, white mark on the first image to indicate a segment for analysis, presented on Fig. 4.33.

Evolution of LIPSS under this fluence can be seen in Fig. 4.32, where it can be seen that the ripples bigger than in the regime with low fluence and also the orientation of the nanostructures changes from vertical to horizontal. In order to appreciate in more detail the evolution of the ripples, a transversal cut was done and analyzed over time, the results are shown in Fig. 4.33.

In contrast with the steady state achieved on the low fluence regime, there is a phase change on the structures as seen on Fig. 4.33. The transversal cut plotted on Fig. 4.33a shows that there are pulses whose ripples are out of phase by  $180^\circ$  between the last impulsión of the laser. This can be seen with more detail on Figs. 4.33b and 4.33c, where an alternating phase of



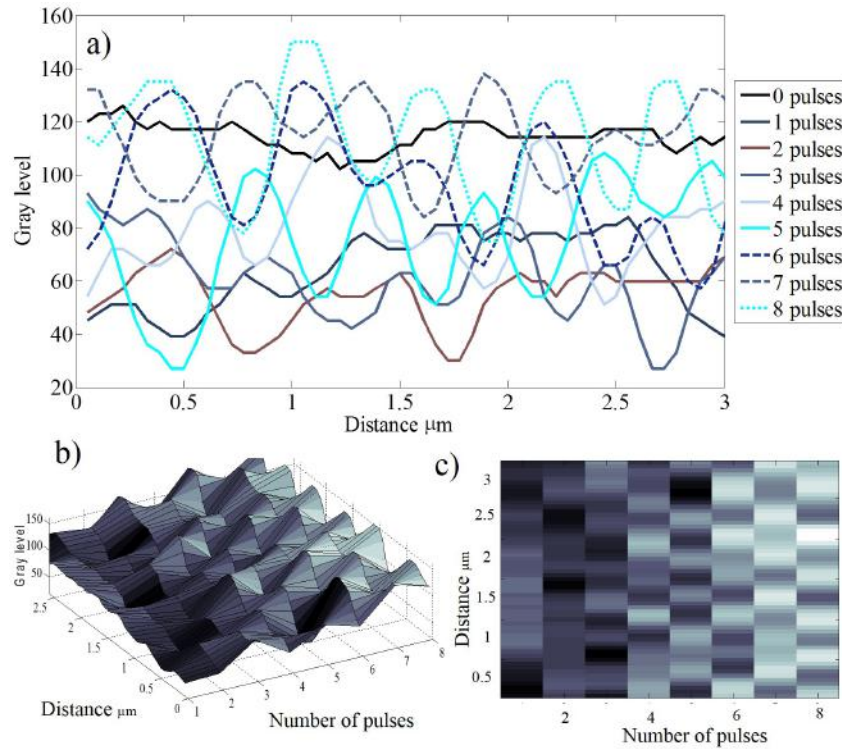


Figure 4.33. Transversal cut for analyze the time evolution of LIPSS on a stainless steel sample with high fluence. a) Comparison graph of the 8 profile of LIPSS over stainless steel low fluence regime, b) time evolution of the structures on stainless steel at high fluence, c) time evolution of the structures on stainless steel at high fluence on a color scale.

$180^\circ$  is clearly visible.

This effects gives information that has to be analyzed so the formation of nanostructures over metallic surface can be understand with more detail.

## 4.6 Conclusions

In this chapter it has been shown how the expansion of the microscope pupil by projecting structured illumination in different directions over the sample can modify the resolution of the microscope. Structured illumination microscopy (SIM) allows the computing of high frequency information of the object that has been restricted by the optical transfer function of the microscope. Traditional SIM has been used only on samples that have been previously treated with fluorophores, so it has been used specially for biological samples. However it has been shown that by changing the illumination, this technique can be adapted for specular samples also. Illumination of SIM usually is done by projecting a phase grid over the fluorophores, which produces a structured illumination pattern over the sample. Though, by changing the phase grid for an amplitude grating and projected it over the sample, fringe projection techniques usually used in optical metrology can be adapted and used over SIM. Using this little modification super resolution over specular samples can be achieved. This alteration of classical SIM lets the examination of small objects that are beyond diffraction limit of optical microscopy by a factor of two.

Usually the examination of nanostructures beyond diffraction limit on specular surface has been done only by non-optical methods such as the atomic force microscope or by scanning electron microscope. It has been shown that using amplitude SIM the observation of structures beyond this limit is accomplished; letting some advantages over AFM or SEM. For instance, SIM technique can be used for the examination of the sample evolution through time as there is no special treatment of the sample or physical contact with it. But one disadvantage of the developed technique is that it requires at least nine images in order to obtain one single super resolution image. This technique was developed especially for the analysis of nanostructures generated over metallic samples by ultrashort laser pulses. With SIM, the period of the nanostructures could be analyzed better than on classical optical microscopy, because this nanostructures or ripples are beyond diffraction limit of an optical microscope. It has been shown how this ripples were formed over the time with some samples, including stainless steel, a metallic glass sample and silica n-type. Depending on the material, the laser power and the number of pulses several effects were observed using SIM that otherwise couldn't be observed.

## CHAPTER 5

# DISCUSSIONS AND CONCLUSIONS

### Contents

---

<b>5.1</b>	<b>Concluding remarks . . . . .</b>	<b>139</b>
<b>5.2</b>	<b>Further work . . . . .</b>	<b>141</b>

---

## 5.1 Concluding remarks

This work has shown a study of the effects introduced by a vortex phase filter in the microscope pupil. The main finding was that the filter can be used to obtain the same results than the phase contrast techniques. By quantifying this phase vortex into a multi-step phase vortex, the phase of the analyzed object can be quantified by rotating the filter into different angles. It has been shown that depending on the object, an edge enhancement of the object border or a spiral carrier on the interferograms are obtained. However the phase extraction can be done using the same algorithm. Using multi-step vortex provides some advantages over classical phase extraction techniques, such as the implementation of the vortex on low range spatial light modulators, and that the rotation of the filter can be done with high accuracy avoiding problems such as detuning.

The multi-step vortex can be adapted into a combined filter which adds the amplitude of a Smartt type filter, and the phase vortex. Using this combined filter a new point diffraction interferometer with spiral carrier was proposed. This interferometer can also be used for phase measurement by the rotation of the vortex, being more simple the rotation of a mask than using liquid crystals over just the center of the filter. Also as a multi-step vortex phase filter is used, the implementation is simpler as it requires only constant phase areas over the filter, which is easier to incorporate in the manufacturing of this complex filter.

It has been also shown this phase-only multi-step vortex can be applied on speckle interferometry for out-plane displacement measurement. Filtering with a multi-step vortex filter creates a different speckle which can be used for computing correlation fringe patterns which can be used in combination with the filter rotation to measure the displacement of rough samples. With all the advantages of the multi-step vortex filter that have been previously reported.

Finally it has been demonstrated that the expansion of the microscope pupil by projecting structured illumination in different directions over the sample allows an increment of the conventional resolution of the microscope. The illumination that is frequently used by the SIM technique using a phase grid, and applied to samples containing fluorophores has been adapted to inspect nanostructures in metallic samples. The main adaptation, was to replace the phase grid by an amplitude grating to deal with specular samples. This alteration of classical SIM lets the examination of specular objects of nanometric dimensions, allowing a resolution improvement by a factor of two. This technique was especially developed for the analysis of nanostructures generated over metallic samples by ultrashort laser pulses.

## 5.2 Further work

The work presented on this thesis can have improvements which can be foreseen, for the quantitative phase contrast microscopy, and for the super resolution microscopy. The implementation of the multi-step vortex on an optical setup can be with optical systems that deliver magnifications of the object, with the possibility of incorporation into a commercial microscope. This could be achieved by using a vortex phase plate instead of a spatial light modulator such as the LCoS. The vortex phase plate, as it is built with multi-steps is easily constructed by using thin films deposition over a substrate. Moreover, an extra amplitude film can be deposited over the filter creating the combined amplitude-phase filter, which be used for the point diffraction interferometer; being adapted into a one path quantitative phase contrast microscope with commercial applications.

The main disadvantage of the super resolution optical microscope structured light is that a high number of frames are needed in order to obtain just one image with extended resolution. This restriction does not allows the analysis of super resolving images in short times, limiting the in-situ analysis of fast evolving images from a microscope. Techniques that use spatial multiplexing can be studied with more detail so to speed up the super-resolving acquisition, allowing the analysis of fast super-resolved phenomena.



# BIBLIOGRAPHY

- [1] D. Malacara. *Óptica Básica*. Fondo de Cultura Economica, México, D.F, 1 edition, 1989.
- [2] E. Hetch. *Optics*. Pearson Education, San Francisco, 4 edition, 2002.
- [3] D. B. Murphy. *Fundamentals of light microscopy and electronic imaging*. John Wiley & Sons, 2002.
- [4] B. Herman. *Fluorescence microscopy*. BIOS Scientific Publishers, 1998.
- [5] S. Bradbury. *The evolution of the microscope*. Elsevier, 2014.
- [6] G. Shtengel, J.A Galbraith, C.G. Galbraith, J. Lippincott-Schwartz, J.M Gillette, S. Manley, R. Sougrat, C.M Waterman, P. Kanchana-wong, M.W. Davidson, et al. Interferometric fluorescent super-resolution microscopy resolves 3d cellular ultrastructure. *Proceedings of the National Academy of Sciences*, **106**(9):3125–3130, 2009.
- [7] E.J.K.T.D.J.S.R.L. Betzig, J.K. Trautman, T.D. Harris, J.S. Weiner, and R.L. Kostelak. Breaking the diffraction barrier: optical microscopy on a nanometric scale. *Science*, **251**(5000):1468–1470, 1991.
- [8] B. Huang, M. Bates, and X. Zhuang. Super resolution fluorescence microscopy. *Annual Review of Biochemistry*, **78**:993, 2009.
- [9] C. Mann, L. Yu, C.M Lo, and M. Kim. High-resolution quantitative phase-contrast microscopy by digital holography. *Optics Express*, **13**(22):8693–8698, 2005.
- [10] R.G. Fassett, B. Horgan, and T.H. Mathew. Detection of glomerular bleeding by phase-contrast microscopy. *The Lancet*, **319**(8287):1432–1434, 1982.
- [11] C.M Waterman-Storer, A. Desai, J.C. Bulinski, and E.D. Salmon. Fluorescent speckle microscopy, a method to visualize the dynamics of protein assemblies in living cells. *Current Biology*, **8**(22):1227–S1, 1998.

- [12] G. Seward. Optical design of microscopes. SPIE, 2010.
- [13] Michael W. Davidson Kenneth R. Spring, H. Ernst Keller. Olympus microscopy resource center. <http://www.olympusmicro.com/primer/anatomy/objectives.html/>, 2012.
- [14] Zeiss Corporation. Zeiss. <http://zeiss-campus.magnet.fsu.edu/articles/basics/index.html>, 2014.
- [15] Tomasz S. T. *Field Guide to Microscopy*. SPIE Press, Washington, 1 edition, 2010.
- [16] A. Köhler. Ein neues beleuchtungsverfahren für mikrographische zwecke. *Zeitschrift für wissenschaftliche Mikroskopie und für Mikroskopische Technik*, **10**(4):433–440, 1893.
- [17] Nikon Corporation. Nikon. <http://www.microscopyu.com/>, 2014.
- [18] J.W Goodman. *Introduction to Fourier Optics*. McGraw-Hill, New York, 2 edition, 1996.
- [19] J. B. Pawley. *Handbook of Biological Confocal Microscopy*. Springer, Wisconsin, 3 edition, 2006.
- [20] D.B Murphy and M.W Davidson. Differential interference contrast microscopy and modulation contrast microscopy. *Fundamentals of Light Microscopy and Electronic Imaging, Second Edition*, pages 173–197, 2001.
- [21] M. Born and E. Wolf. *Principles of optics: electromagnetic theory of propagation, interference and diffraction of light*. Cambridge university press, 1999.
- [22] H.U. Dodt and W. Ziegglängsberger. Visualizing unstained neurons in living brain slices by infrared dic-videomicroscopy. *Brain research*, **537**(1):333–336, 1990.
- [23] S. Bernet, A. Jesacher, S. Fürhapter, C. Maurer, and M. Ritsch-Marte. Quantitative imaging of complex samples by spiral phase contrast microscopy. *Optics Express*, **14**(9):3792–3805, 2006.
- [24] C. Maurer, A. Jesacher, S. Bernet, and M. Ritsch-Marte. What spatial light modulators can do for optical microscopy. *Laser & Photonic Reviews*, **5**(1):81–101, 2011.



- 
- [25] C. Maurer, S. Bernet, and M. Ritsch-Marte. Refining common path interferometry with a spiral phase fourier filter. *J. Opt. A*, **11**(9):1–7, 2009.
- [26] M. Minsky. Memoir on inventing the confocal scanning microscope. *Scanning*, **10**(4):128–138, 1988.
- [27] D. Semwogerere and E.R Weeks. Confocal microscopy. *Encyclopedia of Biomaterials and Biomedical Engineering*, **426**:1–10, 2005.
- [28] L. Moreaux, O. Sandre, and J. Mertz. Membrane imaging by second-harmonic generation microscopy. *J. Opt. Soc. Am. B*, **17**(10):1685–1694, 2000.
- [29] W.R Zipfel, R.M Williams, R. Christie, A.Y Nikitin, B.T. Hyman, and W.W. Webb. Live tissue intrinsic emission microscopy using multiphoton-excited native fluorescence and second harmonic generation. *Proceedings of the National Academy of Sciences*, **100**(12):7075–7080, 2003.
- [30] F. Helmchen and W. Denk. Deep tissue two-photon microscopy. *Nature Methods*, **2**(12):932–940, 2005.
- [31] YR Shen. Surface properties probed by second-harmonic and sum-frequency generation. *Nature*, **337**:519–525, 1989.
- [32] P.J Campagnola, Mei-de Wei, A. Lewis, and L.M Loew. High-resolution nonlinear optical imaging of live cells by second harmonic generation. *Biophysical Journal*, **77**(6):3341–3349, 1999.
- [33] Z. Zalevsky and D. Mendlovic. *Optical Superresolution*. Physics and Astronomy Online Library. Springer, 2004.
- [34] G.T Di Francia. Super-gain antennas and optical resolving power. *Il Nuovo Cimento (1943-1954)*, **9**:426–438, 1952.
- [35] T. RM Sales and G. M. Morris. Diffractive superresolution elements. *J. Opt. Soc. Am. A*, **14**(7):1637–1646, 1997.
- [36] M.P Cagigal, J.E Oti, V.F Canales, and P.J Valle. Analytical design of superresolving phase filters. *Optics Communications*, **241**(4):249–253, 2004.
- [37] Hongxin Luo and Changhe Zhou. Comparison of superresolution effects with annular phase and amplitude filters. *Applied Optics*, **43**(34):6242–6247, 2004.

- [38] J. Reymann, D. Baddeley, M. Gunkel, P. Lemmer, W. Stadter, Thibaud J., K. R., C. Cremer, and Udo Birk. High-precision structural analysis of subnuclear complexes in fixed and live cells via spatially modulated illumination (smi) microscopy. *Chromosome Research*, **16**(3):367–382, 2008.
- [39] R.C Dunn. Near-field scanning optical microscopy. *Chemical Reviews*, **99**(10):2891–2928, 1999.
- [40] M.G.L Gustafsson. Nonlinear structured-illumination microscopy: Wide-field fluorescence imaging with theoretically unlimited resolution. *Proceedings of the National Academy of Sciences*, **102**(37):13081–13086, 2005.
- [41] S.W Hell, K.I Willig, M. Dyba, S. Jakobs, L. Kastrup, and V. Westphal. Nanoscale resolution with focused light: Sted and other resoltf microscopy concepts. *Handbook of biological confocal microscopy*, pages 571–579, 2006.
- [42] S.W Hell and J. Wichmann. Breaking the diffraction resolution limit by stimulated emission: stimulated-emission-depletion fluorescence microscopy. *Optics Letters*, **19**(11):780–782, 1994.
- [43] S.W Hell. Far-field optical nanoscopy. *Science*, **316**(5828):1153–1158, 2007.
- [44] T. A Klar and S. W Hell. Subdiffraction resolution in far-field fluorescence microscopy. *Optics Letters*, **24**(14):954–956, 1999.
- [45] G. Patterson, M. Davidson, S. Manley, and J. Lippincott-Schwartz. Superresolution imaging using single-molecule localization. *Annual Review of Physical Chemistry*, **61**:345, 2010.
- [46] R. Heintzmann, H. Münch, and C. Cremer. High-precision distance measurements in epifluorescent microscopy-simulation and experiment. *Cell Vision*, **4**:252–253, 1997.
- [47] C. Cremer, R. Kaufmann, M. Gunkel, Sebastian Pres, Y. Weiland, P. Müller, T. Ruckelshausen, P. Lemmer, F. Geiger, S. Degenhard, et al. Superresolution imaging of biological nanostructures by spectral precision distance microscopy. *Biotechnology Journal*, **6**(9):1037–1051, 2011.
- [48] C. Cremer, R. Kaufmann, M. Gunkel, F. Polanski, P. Müller, R. Dierkes, S. Degenhard, C. Wege, M. Hausmann, and U. Birk. Ap-

- plication perspectives of localization microscopy in virology. *Histochemistry and Cell Biology*, **142**(1):43–59, 2014.
- [49] M.J Rust, M. Bates, and X. Zhuang. Sub-diffraction-limit imaging by stochastic optical reconstruction microscopy (storm). *Nature Methods*, **3**(10):793–796, 2006.
- [50] E. Betzig, G.H. Patterson, R. Sougrat, O.W. Lindwasser, S. Olenych, J.S Bonifacino, M.W. Davidson, J. Lippincott-Schwartz, and H.F. Hess. Imaging intracellular fluorescent proteins at nanometer resolution. *Science*, **313**(5793):1642–1645, 2006.
- [51] S.T Hess, T.P.K. Girirajan, and M.D. Mason. Ultra-high resolution imaging by fluorescence photoactivation localization microscopy. *Biophysical Journal*, **91**(11):4258–4272, 2006.
- [52] Y. Chen, A.D. Aguirre, P.L. Hsiung, S. Desai, P.R. Herz, M. Pedrosa, Q. Huang, M. Figueiredo, S.W. Huang, A. Koski, et al. Ultrahigh resolution optical coherence tomography of barrett’s esophagus: preliminary descriptive clinical study correlating images with histology. *Endoscopy*, **39**(7):599–605, 2007.
- [53] A. Dubois, L. Vabre, A.C. Boccara, and E. Beaufepaire. High-resolution full-field optical coherence tomography with a linnik microscope. *Applied Optics*, **41**(4):805–812, 2002.
- [54] D. Huang, E.A. Swanson, C.P. Lin, J.S Schuman, W.G Stinson, W. Chang, M.R. Hee, T. Flotte, K. Gregory, C.A. Puliafito, et al. Optical coherence tomography. *Science*, **254**(5035):1178–1181, 1991.
- [55] J.G Fujimoto, M.E Brezinski, G.J. Tearney, S.A. Boppart, B. Bouma, M.R. Hee, J.F. Southern, and E.A. Swanson. Optical biopsy and imaging using optical coherence tomography. *Nature Medicine*, **1**(9):970–972, 1995.
- [56] G.J Tearney, M.E Brezinski, B.E Bouma, S.A Boppart, C. Pitris, J.F. Southern, and J.G. Fujimoto. In vivo endoscopic optical biopsy with optical coherence tomography. *Science*, **276**(5321):2037–2039, 1997.
- [57] M.R Hee, J.A Izatt, E.A Swanson, D. Huang, J.S Schuman, C.P. Lin, C.A. Puliafito, and J.G. Fujimoto. Optical coherence tomography of the human retina. *Archives of Ophthalmology*, **113**(3):325–332, 1995.

- [58] S.N Khonina, V.V Kotlyar, M.V Shinkaryev, V.A Soifer, and G.V Uspleniev. The phase rotor filter. *Journal of Modern Optics*, **39**(5):1147–1154, 1992.
- [59] K.T Gahagan and G. A. Swartzlander Jr. Optical vortex trapping of particles. *Optics Letters*, **21**(11):827–829, 1996.
- [60] J.E. Curtis and D.G. Grier. Modulated optical vortices. *Optics Letters*, **21**(11):872–874, 2003.
- [61] J.E Curtis, B.A Koss, and D.G Grier. Dynamic holographic optical tweezers. *Optics Communications*, **207**(1):169–175, 2002.
- [62] J.A. Davis, D.E. McNamara, D.M. Cottrell, and J. Campos. Image processing with the radial hilbert transform: theory and experiments. *Optics Letters*, **25**(2):99–101, 2000.
- [63] K.G Larkin, D.J. Bone, and M.A. Oldfield. Natural demodulation of two-dimensional fringe patterns. i. general background of the spiral phase quadrature transform. *J. Opt. Soc. Am. A*, **18**(8):1862–1870, 2001.
- [64] A.H. Nuitall. On the quadrature approximation to the hilbert transform of modulated signals. In *IEEE proceedings*, pages 1458–1459, october 1966.
- [65] J.E. Curtis and D.G. Grier. Structure of optical vortices. *Phys. Rev. Lett.*, **90**(13):133901–133904, Apr 2003.
- [66] A.M Yao and M.J Padgett. Orbital angular momentum: origins, behavior and applications. *Advances in Optics and Photonics*, **3**(2):161–204, 2011.
- [67] A.W. Lohmann, D. Mendlovic, and Z. Zalevsky. Fractional hilbert transform. *Optics Letters*, **21**(4):281–285, 1996.
- [68] V. Lerner, D. Shaw, Y. Drori, and N. Katz. Shaping laguerre-gaussian laser modes with binary gratings using a digital micromirror device. *Optics Letters*, **37**(23):4286–4288, 2012.
- [69] D.P. Ghai, P. Senthilkumaran, and R.S. Sirohi. Adaptive helical mirror for generation of optical phase singularity. *Applied Optics*, **47**(10):1378–1383, 2008.
- [70] A. Aguilar, A. Dávila, and J. García-Márquez. Multi-step vortex filtering for phase extraction. *Optics Express*, **22**(7):8503–8514, 2014.

- 
- [71] Cheng-Shan Guo, Dong-Mei Xue, Yu-Jing Han, and Jianping Ding. Optimal phase steps of multi-level spiral phase plates. *Optics Communications*, **268**(2):235–269, 2006.
- [72] A. Jesacher, S. Fürhapter, S. Bernet, and M. Ritsch-Marte. Shadow effects in spiral phase contrast microscopy. *Physical Review Letters*, **94**(23):223902–1–223902–4, 2005.
- [73] S. Fürhapter, A. Jesacher, S. Bernet, and M. Ritsch-Marte. Spiral interferometry. *Optics Letters*, **30**(15):1953–1955, 2005.
- [74] A. Jesacher, S. Fürhapter, S. Bernet, and M. Ritsch-Marte. Spiral interferogram analysis. *J. Opt. Soc. Am. A*, **23**(6):1400–1409, 2006.
- [75] Ronald Bracewell. *The Fourier Transform and Its Applications*. McGraw-Hill Science/Engineering/Math, New York, 3 edition, 1999.
- [76] J.A. Quiroga, M. Servin, and F. Cuevas. Modulo  $2\pi$  fringe orientation angle estimation by phase unwrapping with a regularized phase tracking algorithm. *J. Opt. Soc. Am. A*, **19**(8):1524–1531, 2002.
- [77] J.A. Quiroga, J.A. Gómez-Pedrero, and A. García-Botella. Algorithm for fringe pattern normalization. *Optics Communications*, **197**(1):43–51, 2001.
- [78] J.A. Quiroga, M. Servin, J.L. Marroquin, and D. Crespo. Estimation of the orientation term of the general quadrature transform from a single  $n$ -dimensional fringe pattern. *J. Opt. Soc. Am. A*, **22**(3):439–444, 2005.
- [79] Ismael Villa, J.R. and G. Miramontes. Phase recovery from a single fringe pattern using an orientational vector-field-regularized estimator. *J. Opt. Soc. Am. A*, **22**(12):2766–2773, 2004.
- [80] K. Larkin. Natural demodulation of two-dimensional fringe patterns. ii. general background of the spiral phase quadrature transform. *J. Opt. Soc. Am. A*, **18**(8):1871–1881, 2001.
- [81] D. Kerr, G.H. Kaufmann, and G. E. Galizzi. Unwrapping of interferometric phase-fringe maps by the discrete cosine transform. *Applied Optics*, **35**(5):810–816, 1996.
- [82] D.J. Bone. Fourier fringe analysis: the two-dimensional phase unwrapping problem. *Applied Optics*, **30**(25):3627–3632, 1991.

- [83] R. Cusack, J.M. Huntley, and H.T. Goldrein. Improved noise-immune phase-unwrapping algorithm. *Applied Optics*, **34**(5):781–789, 1995.
- [84] M. Servin and J.C. Estrada. Analysis and synthesis of phase shifting algorithms based on linear systems theory. *Optics and Lasers in Engineering*, **50**(8):1009–1014, 2012.
- [85] Z. Wang and A.C Bovik. A universal image quality index. *Signal Processing Letters, IEEE*, **9**(3):81–84, 2002.
- [86] D. Kerr, G.H. Kaufmann, and G.E. Galizzi. Unwrapping of interferometric phase-fringe maps by the discrete cosine transform. *Applied Optics*, **35**(5):810–816, 1996.
- [87] Y. Calderón-Hermosillo, J. García-Márquez, R. Espinosa-Luna, N.A. Ochoa, V. López, A. Aguilar, E. Noé-Arias, and Y. Alayli. Flicker in a twisted nematic spatial light modulator. *Optics and Lasers in Engineering*, **51**(6):741–748, 2013.
- [88] J. García-Márquez, E. López-Padilla, A. Gónzales-Vega, and E. Noé-Arias. Flicker minimization in an lcos spatial light modulator. *Optics Express*, **20**.
- [89] R.N. Smartt. Special applications of the point-diffraction interferometer. In *23rd Annual Technical Symposium*, pages 35–40. International Society for Optics and Photonics, 1979.
- [90] E. Acosta, S. Chamadoira, and R. Blendowske. Modified point diffraction interferometer for inspection and evaluation of ophthalmic components. *J. Opt. Soc. Am. A*, **23**(3):632–637, 2006.
- [91] P. Gao, I. Harder, V. Nercissian, K. Mantel, and B. Yao. Phase-shifting point-diffraction interferometry with common-path and in-line configuration for microscopy. *Optics Letters*, **35**(5):712–714, 2010.
- [92] C. Koliopoulos, C.R. Hayslett, O. Kwon, R. Shagam, and J.C. Wyant. Infrared point-diffraction interferometer. *Optics Letters*, **3**(3):118–120, 1978.
- [93] K. Otaki, K. Ota, I. Nishiyama, T. Yamamoto, Y. Fukuda, and S. Okazaki. Development of the point diffraction interferometer for extreme ultraviolet lithography: Design, fabrication, and evaluation. *Journal of Vacuum Science & Technology B*, **20**(6):2449–2458, 2002.

- 
- [94] H. Visser. Point-diffraction interferometer, August 21 2002. US Patent App. 10/224,401.
- [95] C.R Mercer and K. Creath. Liquid-crystal point-diffraction interferometer. *Optics Letters*, **19**(12):916–918, 1994.
- [96] H. Medeck. Phase-shifting point diffraction interferometer, November 10 1998. US Patent 5,835,217.
- [97] K.G. Larkin, M.A. Oldfield, and Donald J. Bone. Demodulation and phase estimation of two-dimensional patterns, October 28 2008. US Patent 7,444,032.
- [98] J.C Dainty. Laser speckle and related phenomena. In *Berlin and New York, Springer-Verlag (Topics in Applied Physics. Volume 9), 1975. 298 p*, volume 9, 1975.
- [99] R. Erf. *Speckle metrology*. Elsevier, 2012.
- [100] J.W Goodman. Statistical properties of laser speckle patterns. In *Laser speckle and related phenomena*, pages 9–75. Springer, 1975.
- [101] J.W Goodman. *Speckle phenomena in optics: theory and applications*. Roberts and Company Publishers, 2007.
- [102] L. Leushacke and M. Kirchner. Three-dimensional correlation coefficient of speckle intensity for rectangular and circular apertures. *J. Opt. Soc. Am. A*, **7**(5):827–832, 1990.
- [103] K.J. Gåsvik. *Optical metrology*. John Wiley & Sons, 2003.
- [104] M. Lehmann. Measurement optimization in speckle interferometry: the influence of the imaging lens aperture. *Optical Engineering*, **36**(4):1162–1168, 1997.
- [105] J.M. Huntley. Random phase measurement errors in digital speckle pattern interferometry. *Optics and lasers in engineering*, **26**(2):131–150, 1997.
- [106] M. Lehmann. Decorrelation-induced phase errors in phase-shifting speckle interferometry. *Applied Optics*, **36**(16):3657–3667, 1997.
- [107] A. Martínez, R. Rodríguez-Vera, J.A. Rayas, and H.J. Puga. Fracture detection by grating moiré and in-plane espi techniques. *Optics and Lasers in Engineering*, **39**(5):525–536, 2003.

- [108] F. Gascón et al. Measurement of the longitudinal and transverse vibration frequencies of a rod by speckle interferometry. *Ultrasonics, Ferroelectrics, and Frequency Control, IEEE Transactions on*, **40**(3):265–269, 1993.
- [109] T.P Newson, J.L Santos, and D.A Jackson. Electronic speckle-pattern interferometry compensated for environmentally induced phase noise. In *The Hague'90, 12-16 April*, pages 173–179. International Society for Optics and Photonics, 1990.
- [110] Y. Song, W. Zhang, Y. Wu, and X. Yao. Digital speckle technique applied to flow visualization. *Tsinghua Science and Technology*, **5**(1):89–95, 2000.
- [111] A.J. Moore and J.R. Tyrer. An electronic speckle pattern interferometer for complete in-plane displacement measurement. *Measurement science and technology*, **1**(10):1024, 1990.
- [112] H.J. Tiziani. Application of speckling for in-plane vibration analysis. *Journal of Modern Optics*, **18**(12):891–902, 1971.
- [113] A. Dávila, S. Márquez, E. Landgrave, Z. Vázquez, K. Vera, and C. Caudillo. Axial loading verification method for small bones using carrier fringes in speckle pattern interferometry. *Journal of Modern Optics*, **62**(11):1–6, 2015.
- [114] J.A. Leendertz and J.N. Butters. An image-shearing speckle-pattern interferometer for measuring bending moments. *Journal of Physics E: Scientific Instruments*, **6**(11):1107, 1973.
- [115] H.A Aebischer and S. Waldner. Strain distributions made visible with image-shearing speckle pattern interferometry. *Optics and Lasers in Engineering*, **26**(4):407–420, 1997.
- [116] S.Y. Wu and Y.W. Qin. Determination of residual stresses using large shearing speckle interferometry and the hole drilling method. *Optics and Lasers in Engineering*, **23**(4):233–244, 1995.
- [117] J.D.R Valera, J.D.C Jones, D.P Towers, and C.H. Buckberry. Strain and vibration analysis by fibre based speckle shearing interferometry. *Optics and Lasers in Engineering*, **26**(4):361–376, 1997.
- [118] Y.Y Hung. A speckle-shearing interferometer: a tool for measuring derivatives of surface displacements. *Optics Communications*, **11**(2):132–135, 1974.



- 
- [119] A. Dávila, M. Servin, and M. Facchini. Fast phase-map recovery from large shears in an electronic speckle-shearing pattern interferometer using a fourier least-squares estimation. *Optical Engineering*, **39**:2487–2494, 2000.
- [120] X. Chen, Z. Li, H. Li, M. Zhang, and C. Cheng. Experimental study on the existence and properties of speckle phase vortices in the diffraction region near random surfaces. *Optics Express*, **20**(16):17833–17842, 2012.
- [121] W. Wang, T. Yokozeki, R. Ishijima, A. Wada, Y. Miyamoo, M. Takeda, and S.G. Hanson. Optical vortex metrology for nanometric speckle displacement measurement. *Optics Express*, **14**(1):120–127, 2006.
- [122] W. Wang, Y. Qiao, R. Ishijima, T. Yokozeki, D. Honda, A. Matsuda, S.G. Hanson, and M. Takeda. Constellation of phase singularities in a speckle-like pattern for optical vortex metrology applied to biological kinematic analysis. *Optics Express*, **16**(18):13908–13917, 2008.
- [123] A. Dávila, J.E.A. Landgrave, and G. Garnica. In situ calibration of a michelson type, speckle-shearing interferometer: Wobbling mirror effect. *Optics and Lasers in Engineering*, **45**(1):70–76, 2007.
- [124] A. Dávila, J.M. Huntley, G.H. Kaufmann, and D. Kerr. High-speed dynamic speckle interferometry: phase errors due to intensity, velocity, and speckle decorrelation. *Applied Optics*, **44**(19):3954–3962, 2005.
- [125] D. Pal Ghai, P. Senthilkumaran, and R.S. Sirohi. Adaptive helical mirror for generation of optical phase singularity. *Applied Optics*, **47**(10):1378–1383, 2008.
- [126] V. Lerner, D. Shwa, Y. Drori, and N. Katz. Shaping laguerre–gaussian laser modes with binary gratings using a digital micromirror device. *Optics Letters*, **37**(23):4826–4828, 2012.
- [127] I. Moreno, C. Iemmi, J. Campos, M.J. Yzuel, and A. Vargas. Polarization vortices generation by diffraction from a four quadrant polarization mask. *Optics Communications*, **276**(2):222–230, 2007.
- [128] R.S. Cudney, H.M. Escamilla, and L.A. Ríos. Electro-optic vortex-producing lenses using spiral-shaped ferroelectric domains. *Optics Express*, **17**(2):997–1002, 2009.

- 
- [129] A. Dávikla, G.H. Kaufmann, D. Kerr, et al. Scale-space filter for smoothing electronic speckle pattern interferometry fringes. *Optical Engineering*, **35**(12):3549–3554, 1996.
- [130] J. L Marroquin, M. Rivera, S. Botello, R. Rodriguez-Vera, and M. Servin. Regularization methods for processing fringe-pattern images. *Applied Optics*, **38**(5):788–794, 1999.
- [131] J. Garcia-Marquez, J.E.A. Landgrave, N. Alcala-Ochoa, and C. Perez-Santos. Recursive wavefront aberration correction method for lcos spatial light modulators. *Optics and Lasers in Engineering*, **49**(6):743–748, 2011.
- [132] M. K. Sharma, J. Joseph, and P. Senthilkumaran. Effect of aberrations in vortex spatial filtering. *Optics and Lasers in Engineering*, **50**(11):1501–1507, 2012.
- [133] S. Wu, X. He, and L Yang. Enlarging the angle of view in michelson interferometer-based shearography by embedding a  $4f$  system. *Applied Optics*, **50**(21):3789–3794, 2011.
- [134] Cai. C. and L. He. Improved mach-zehnder interferometer-based shearography. *Optics and Laser in Engeniering*, **50**(12):1699–1708, 2012.
- [135] M.A.A Neil, R. Juskaitis, and T. Wilson. Method of obtaining optical sectioning by using structured light in a conventional microscope. *Optics Letters*, **22**(24):1905–1907, 1997.
- [136] S. Chowdhury and J. Izatt. Structured illumination diffraction phase microscopy for broadband, subdiffraction resolution, quantitative phase imaging. *Optics Letters*, **39**(4):1015–1018, 2014.
- [137] J.H. Park, S.W. Lee, E.S Lee, and J.Y Lee. A method for super-resolved cars microscopy with structured illumination in two dimensions. *Optics Express*, **22**(8):9854–9870, 2014.
- [138] Sebastian H. *OMX – A Novel High Speed and High Resolution Microscope and its Application to Nuclear and Chromosomal Structure Analysis*. PhD thesis, Berlin University, 2007.
- [139] M. Takeda, H. Ina, and S. Kobayashi. Fourier-transform method of fringe-pattern analysis for computer-based topography and interferometry. *J. Opt. Soc. Am. A*, **72**(1):156–160, 1982.

- 
- [140] M. Servin and J.C. Estrada. Analysis and synthesis of phase shifting algorithms based on linear systems theory. *Optics and Lasers in Engineering*, **50**(8):1009–1014, 2012.
- [141] J.M. Huntley. An image processing system for the analysis of speckle photographs. *Journal of Physics E: Scientific Instruments*, **19**(1):43, 1986.
- [142] B. Thomas, M. Momany, and P. Kner. Optical sectioning structured illumination microscopy with enhanced sensitivity. *Journal of Optics*, **15**(9):094004, 2013.
- [143] M. Gustafsson. Extended-resolution reconstruction of structured illumination microscopy data. In *Computational Optical Sensing and Imaging*, page JMA2. Optical Society of America, 2005.
- [144] Malacara D., M. Servin, and Malacara Z. *Interferogram analysis for optical testing*, volume 84. CRC press, 2005.
- [145] P.G. Kazansky and Y. Shimotsuma. Self-assembled sub-wavelength structures and form birefringence created by femtosecond laser writing in glass: properties and applications. *Journal of the Ceramic Society of Japan*, **116**(1358):1052–1062, 2008.
- [146] G. Cheng, K. Mishchik, C. Mauclair, E. Audouard, and R. Stoian. Ultrafast laser photoinscription of polarization sensitive devices in bulk silica glass. *Optics Express*, **17**(12):9515–9525, 2009.
- [147] C. Mauclair, M. Zamfirescu, J.P. Colombier, G. Cheng, K. Mishchik, and R. Audouard, E.and Stoian. Control of ultrafast laser-induced bulk nanogratings in fused silica via pulse time envelopes. *Optics Express*, **20**(12):12997–13005, 2012.
- [148] Y. Shimotsuma, M. Sakakura, P.G Kazansky, M. Beresna, J. Qiu, K. Miura, and K. Hirao. Ultrafast manipulation of self-assembled form birefringence in glass. *Advanced Materials*, **22**(36):4039–4043, 2010.
- [149] R. Taylor, C. Hnatovsky, and E. Simova. Applications of femtosecond laser induced self-organized planar nanocracks inside fused silica glass. *Laser & Photonics Reviews*, **2**(1-2):26–46, 2008.

